Aix*Marseille université
Socialement engagée

NNT/NL : 2022AIXM0345/037ED352

THÈSE DE DOCTORAT

Soutenue à Aix-Marseille Université
le 28 Octobre 2022 par

Valeria Ostuni

Impact de la composition du plasma et du rapport d'aspect sur les performances globales du tokamak

Discipline
Physique et Sciences de la Matière

spécialité
Énergie, Rayonnement et Plasma

École doctorale
ED PHYSIQUE ET SCIENCES DE LA MATIÈRE

Laboratoire/Partenaires de recherche
CEA de Cadarache

Composition du jury

Jonathan Citrin Chef du groupe DIFFER, CCER	Rapporteur
Federico Felici Coordinateur scientifique, EPFL	Rapporteur
Yanick Sarazin Directeur de Recherche en Physique, CEA	Examinateur
Pascale Hennequin Directrice de recherche, CNRS	Présidente du jury
Clarisse Bourdelle Directrice de recherche, CEA	Directrice de thèse
Jorge Morales Ingénieur chercheur, CEA	Superviseur CEA

cea

Affidavit

Je soussigné, Valeria Ostuni, déclare par la présente que le travail présenté dans ce manuscrit est mon propre travail, réalisé sous la direction scientifique de [Clarisse Bourdelle], dans le respect des principes d'honnêteté, d'intégrité et de responsabilité inhérents à la mission de recherche. Les travaux de recherche et la rédaction de ce manuscrit ont été réalisés dans le respect à la fois de la charte nationale de déontologie des métiers de la recherche et de la charte d'Aix-Marseille Université relative à la lutte contre le plagiat.

Ce travail n'a pas été précédemment soumis en France ou à l'étranger dans une version identique ou similaire à un organisme examinateur.

Fait à Cadarache le 26/8/2022

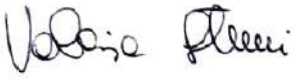

List of publications and conference participation

List of publications produced in the framework of the thesis project :

1. V. Ostuni et al. "Core radiative collapse characterisation and integrated modelling in WEST plasmas", *Nucl. Fusion*, https://iopscience.iop.org/article/10.1088/1741-4326/ac8cd6 (2022)
2. G. Urbanczyk, , L. Colas, J. Hillairet, E. Lerche, N. Fedorczak, J. Morales , J. Gunn, V. Ostuni et al. "RF wave coupling, plasma heating and characterization of induced plasma-material interactions in WEST L-mode discharges", *Nucl. Fusion*, **61** (2021) 086027 (19pp)
3. M. Goniche, V. Ostuni et al. "Developing high performance RF heating scenarios on the WEST tokamak", *Nucl. Fusion*, **text** (2022)

Participation in conferences and summer schools during the thesis period :

1. WPSA meeting - Budapest (online), 02/04/2020;
2. ITPA T&C meeting - Garching (online), 30/06/2020;
3. QuaLiKiz and QLKNN mini-workshop (online), 18/03/2021;
4. Culham Plsma Physics Summer School - Oxford, 05/09/2021-18/09/2021;
5. Poster contribution to EU-US joint TTF meeting (online), 06/09/2021;
6. Invited talk to 5th Asia-Pacific Conference on Plasma Physics (online), 26/09/2021;
7. Plenary talk to US-EU joint TTF meeting - Santa Rosa, 07/04/2022;
8. Contributed Oral to 48th EPS Conference on Plasma Physics (online), 30/06/2022;
9. Contributed Oral to 6th Asia-Pacific Conference on Plasma Physics (online), 26/09/2022.

Résumé

WEST est le tokamak métallique en fonctionnement depuis décembre 2016. Ses caractéristiques sont une valeur rapport d'aspect de 5-6 et la paroi interne recouverte en tungstène. Ses plasmas sont chauffés par chauffage électronique et sans couple de rotation. Dans ce travail, nous analysons en profondeur la base de données du plasma de WEST pour caractériser le domaine opérationnel. Ensuite, nous appliquons un modèle de transport turbulent et explorons sa validité sur le domaine opérationnel de WEST.

La dépendance paramétrique du temps de confinement par rapport au rapport d'aspect (A) est obtenue en ajoutant les données WEST à la base de données ITER existante. La base de données WEST contient plus de 1000 entrées en mode L, deutérium uniquement, chauffées par ondes à la fréquence hybride basse et par résonance cyclotronique ionique. Les études réalisées prennent en compte les statistiques calculées sur les plateaux de puissance totale croisant les plateaux de courant plasma (états quasi stables). En injectant 1000 plateaux WEST aux 1312 entrées existantes, le coefficient de régression calculé associé au rapport d'aspect est proche de zéro, comme précédemment trouvé pour L96 malgré la nouvelle gamme de rapport d'aspect couverte par WEST.

Dans la base de données WEST, on a observé que deux états de confinement différents coexistent, les branches froide et chaude, pour un $P_{tot}/n_{e,vol}$ donné. Dans la première, $T_e(0)$ est supérieur à 2keV. Alors que dans la "branche froide", $T_e(0)$ reste inférieur à 2 keV. De plus, les 25% des plateaux détectés sont dus à un collapse rapide de la température centrale des électrons de la branche chaude à la branche froide.

Expérimentalement, on observe une réduction initiale lente de la température central des électrons due à une augmentation de la densité, tandis que le profil central du tungstène est plat et constant dans le temps. Ensuite, un collapse radiatif se produit : le profil du tungstène central atteint rapidement un pic, en même temps, la mesure du canal central des rayons X durs diminue, indiquant un changement dans l'absorption du des ondes hybrides (LHCD) central. La modélisation intégrée à l'aide de plusieurs codes de calcul est utilisée pour explorer la chaîne de causalité (RAPTOR couplé au réseau neuronal 10D QuaLiKiz, LUKE pour calculer le profil de dépôt de puissance LHCD). Pour reproduire la vitesse du collapse, il faut un pic de tungstène et une réduction de l'absorption centrale du LHCD. Lorsque l'absorption de puissance LHCD centrale est réduite, les profils de température des électrons et des ions au centre s'aplatissent, ce qui réduit le transport thermique néoclassique du tungstène et conduit à l'accumulation de tungstène observée dans le centre. En prenant en compte l'augmentation de la densité de tungstène et la diminution de la puissance LH injectée dans le centre du plasma, le collapse de la température des électrons peut

être reproduit.

Mots clés : loi d'échelle, rapport d'aspect, tungstène, modélisation intégrée, collapse

Abstract

WEST is the metallic tokamak operating since December 2016. Its specificities are an aspect ratio value of 5-6 and a full tungsten coverage. Its plasmas are dominantly electron heated and torque free. In this work, we extensively analyze the database of WEST plasmas to characterize the operational domain. Then, we apply a turbulent transport model and explore its validity on WEST operational space.

The parametric dependence of the confinement time with respect to the aspect ratio (A) is obtained by adding WEST data to the existing ITER database. The WEST database contains more than 1000 entries in L mode, deuterium only pulses, heated by lower hybrid and ion cyclotron resonance heating. The performed studies take into account statistics calculated on plateaus of total power intersecting plasma current plateaus (quasi-steady states). When adding 1083 WEST plateaus to the existing 1312 entries, the computed regression coefficient associated to aspect ratio is close to zero, hence confirming the very weak aspect ratio dependence of ITER96-L scaling law in spite of the new aspect ratio range covered by WEST.

In the WEST database it has been observed that two different confinement states coexist, the cold and the hot branches at a given $P_{tot}/n_{e,vol}$. In the "hot branch", $T_e(0)$ is higher than 2keV and $T_e(0)$ increases with larger $P_{tot}/n_{e,vol}$. While in the "cold branch" $T_e(0)$ remains lower than 2 keV and does not respond to larger $P_{tot}/n_{e,vol}$. Moreover, the 25% of the detected plateaus are effected by a rapid collapse of the central electron temperature from the hot to the cold branch.

Experimentally, during a collapse from the hot to the cold branch, an initial slow reduction of central electron temperature due to a density increase is observed, while the central tungsten profile is flat and constant in time. Then, radiative collapse occurs: the core tungsten profile peaks rapidly, at the same time, the central hard X-ray channel measurement decreases indicating a change in core LHCD absorption. Integrated modelling is used to explore the causality chain (RAPTOR coupled with QuaLiKiz 10D neural network, LUKE to compute the LHCD power deposition profile). To capture the dynamics of the velocity collapse, both, enhanced tungsten core peaking and reduction of central LHCD absorption are required. When central LHCD power absorption is reduced, core electron and ion temperature profiles flatten which reduces the tungsten neoclassical thermal screening and leads to the observed core tungsten accumulation. Taking into account both the increase of the tungsten density and the decrease of the LH power absorbed in the plasma center, the collapse of the central electron temperature can be reproduced.

Keywords: scaling law, aspect ratio, tungsten, integrated modelling, radiative collapse

Résumé en français

L'étude des performances des machines de fusion magnétique est d'une importance fondamentale pour extrapoler vers des dispositifs plus grands et plus puissants tels qu'ITER et DEMO. Pour cette raison, les tokamaks actuellement disponibles, grâce à leurs expériences dédiées, constituent des étapes importantes sur la voie de la production d'énergie à partir de la fusion nucléaire.
De nombreux paramètres peuvent influencer les performances d'un tokamak, dont les plus importants, le courant plasma, la densité électronique, la puissance totale, le champ magnétique toroïdal, l'élongation, le rayon principal, le rapport d'aspect et la masse atomique, conduisent à la définition de la loi d'échelle capable de calculer, et donc de prédire, le temps de confinement magnétique de l'énergie. Cela permet de définir les fenêtres opérationnelles dans lesquelles la machine peut fonctionner en toute sécurité et atteindre les niveaux de performance souhaités.

Ce travail a deux objectifs principaux : le premier est de comprendre l'impact du tungstène, de son rayonnement et du rapport d'aspect sur les performances du tokamak. Le second est de comprendre et de reproduire le collapse radiatif observé pendant l'opération de WEST.

En ce qui concerne le premier objectif, le temps de confinement est analysé à différents niveaux.
Les deux lois d'échelle ITER89-P et ITER96-L sont bien reproduites tant en paramètres dimensionnels que non dimensionnels et leurs différences ont été comprises. En particulier, les différences proviennent d'un écart entre les valeurs de rapport d'aspect entre 4.4 et 5.5. Ceci est dû aux décharges dans la configuration avec un point X bas du tokamak JT-60. Pour ces décharges, le τ_{th} n'est pas disponible et, en plus, elles sont caractérisées par un petit volume de plasma qui conduit à une dégradation du temps de confinement de l'énergie.

La base de données WEST a été construite. Elle ne contient que des chocs en mode L, des décharges en deutérium, dans une configuration avec point X inférieur et avec une faible erreur par rapport aux mesures d'interférométrie.
La seule valeur disponible pour le temps de confinement de l'énergie est τ_{mhd}, donc un sous-ensemble de la base de données en mode L a été sélectionné. En particulier, seules sont sélectionnées les décharges pour lesquelles les valeurs τ_E, τ_{th} et τ_{mhd} sont disponibles et leur différence ne dépasse pas 30%.
Ces décharges sont utilisés pour déterminer la loi d'échelle τ_{mhd}. La grande dispersion des points avec le rapport d'aspect indique que cette quantité a un impact limité sur

le temps de confinement de l'énergie.
Les plateaux WEST sont ajoutés à cette base de données réduite et une loi d'échelle par rapport à τ_{mhd} est établie. WEST est bien aligné avec les autres tokamaks en mode L malgré le fait qu'il a un rapport d'aspect plus grand.

Puisque A, B, k, R et M_{eff} sont fixes dans le fonctionnement de WEST, une loi d'échelle est dérivée par rapport au courant du plasma, à la densité électronique moyenne et à la puissance totale seulement.
Par rapport à ITER96-L, on a constaté une corrélation plus élevée avec le courant du plasma. Cela est dû à la petite gamme opérationnelle de WEST (0,3MA à 0,7MA), la plupart des expériences (environ 800 plateaux) étant réalisées à 0,5MA. Ce paramètre peut être amélioré en augmentant les décharges à un courant plus faible, ou plus élevé, ou en augmentant la gamme opérationnelle. Le coefficient de régression pour la puissance totale est très proche de celui d'ITER96-L. En revanche, la densité présente une corrélation négative, ce qui pourrait être dû au chauffage dominant LHCD qui pourrait ajouter certaines spécificités telles que le chauffage central se déplaçant vers l'extérieur pour les plasmas plus denses. D'autres études ont été menées sur ce sujet et de plus amples informations peuvent être trouvées dans la réf. [M. Goniche, soumis à NF].

Lorsque les données WEST sont ajoutées à ITER96-L et que τ_{mhd} est proche de τ_{th} et que les lois d'échelle en dimensionnel et en sans dimension sont déterminées, le coefficient de régression pour le rapport d'aspect est toujours proche de zéro.
Pour analyser l'impact de la fraction de la puissance rayonnée, cette dernière est soustraite à la puissance totale et la régression est recalculé. Dans ce cas également, les coefficients sont très peu affectés.

L'impact du chauffage par radiofréquence a également été analysé en divisant la base de données WEST en décharges avec $P_{LH} > 1MW$ et décharges avec $P_{ICH} > 1MW$. Les deux lois d'échelle montrent une dépendance inverse par rapport à la densité, ce qui pourrait refléter le fait qu'un plasma plus dense entraîne une absorption LHCD déplacée vers l'extérieur. De plus, l'exposant de dégradation de la puissance est plus grand lorsque le rayonnement global est supprimé. Cela signifie que la dégradation du temps de confinement due au transport turbulent uniquement est plus importante qu'avec les pertes turbulentes et radiatives.

Les décharges ohmiques sont aussi analysées, par conséquent, la base de données est filtrée en tenant compte uniquement de la phase ohmique. En traçant le temps de confinement de l'énergie expérimentale en fonction de la densité électronique linéique moyenne, on a observé le changement du temps de confinement, du régime de confinement ohmique linéaire (LOC) au régime de confinement ohmique saturé (SOC). Une évolution initiale linéaire du temps de confinement est suivie d'une phase saturée.

Grâce à l'inversion de la bolométrie, il est possible d'estimer les profils de tungstène pour $T_e > 1keV$ ainsi que la fraction de puissance rayonnée dans le cœur.
On a vu que le chauffage RF n'a pas d'impact sur la puissance rayonnée dans le cœur puisque les décharges avec LHCD seulement et avec ICRH seulement sont superposées.

Le H_{WEST} a été calculé comme le rapport entre le temps réel de confinement de l'énergie et celui calculé à partir de la loi d'échelle de WEST.
Cette quantité a été utilisée pour quantifier la qualité du confinement et deux groupes de points ont été identifiés.
La branche chaude est caractérisée par une température centrale des électrons, une inductance interne et un flux neutronique élevés, tandis que la branche froide présente une température, une inductance interne et un flux neutronique faibles. Il a été remarqué que certaines décharges dans la branche chaude vont vers la branche froide. Ces chocs ont en commun un collapse rapide de la température électronique centrale.

Un modèle simple pour détecter ces collapses est développé. Nous avons trouvé que 25% des décharges dans la branche chaude collapsent. De plus, tous les plateaux instables sont situés dans la région entre 1,5 keV et 3keV. Ceci est en accord avec la région instable du facteur de refroidissement du tungstène, dans laquelle une diminution de la température électronique centrale augmente le rayonnement et conduit à une nouvelle diminution de la température.
En général, l'évolution temporelle du collapse est la suivante. Une première diminution lente de la température centrale est observée et, en même temps, la densité électronique augmente, puis un effondrement rapide se produit. Le signal du canal central HXR pour la bande d'énergie 60-80 keV diminue, ce signal est une signature de l'absorption de LHCD. En ce qui concerne la densité de tungstène, elle est constante avant l'effondrement et ensuite elle atteint un pic pendant le collapse rapide. Nous concluons que les causes potentielles de l'effondrement du $T_e(0)$ sont : la réduction de l'absorption LHCD centrale et l'augmentation de la radiation du cœur due à l'augmentation du taux de refroidissement et de la densité de tungstène.

Un modèle 0D du collapse a été développé dans lequel seule une concentration effective de tungstène est supposée. Les simulations montrent que le système passe d'un régime stable à une condition stable détériorée. Ce modèle permet de mieux comprendre la dynamique du collapse, mais d'autres phénomènes comme l'absorption de LHCD au cœur et l'accumulation de tungstène jouent aussi un rôle majeur dans l'évolution observée du collapse.

Certaines solutions au problème du collapse ont été testées. En particulier la boronisation et le système de chauffage ICRH.
Dans le premier cas, il a été démontré que l'effet bénéfique de la boronisation dure environ 50 décharges, puisque, après cela, la fraction de puissance rayonnée augmente et se stabilise autour de 50%.

Les acteurs clés à l'origine de la transition de la branche chaude à la branche froide sont identifiés à travers la modélisation intégrée de deux cas typiques, les décharges 55025 et 54802.
Le cadre de la modélisation est composé de simulations METIS interprétatives et de simulations RAPTOR prédictives utilisant le réseau de neurones QuaLiKiz pour le transport de la chaleur. Le code LUKE est utilisé séparément pour déterminer les profils d'absorption de puissance de LHCD. Dans LUKE l'absorption multi-passe est utilisée, l'absorption sur l'axe magnétique n'est pas définie, donc nous avons ajusté cette valeur afin de reproduire l'évolution du T_e central. La densité du tungstène et ses profils sont calculés par inversion de la bolométrie. La puissance rayonnée est calculée en utilisant le facteur de refroidissement du tungstène donné par ADAS 50.
Alors que les travaux antérieurs sur le JET et sur AUG, par exemple, utilisent un cadre plus complet en termes de couplage physique non linéaire avec prédiction de la chaleur, des particules, des radiations, etc. Au début de ce travail, seul RAPTOR était capable de traiter les données IMAS et donc d'être facilement appliqué à WEST. Aujourd'hui, nous pouvons utiliser la version connectée à IMAS du code JETTO (appelée High Fidelity Pulse Simulator) pour lire et modéliser WEST.

Pour les deux décharges étudiées, la première légère baisse de température est due à l'augmentation de la densité électronique. La seule augmentation de la concentration de tungstène dans le centre n'est pas suffisante pour reproduire l'effondrement. Lorsque la réduction de l'absorption de la puissance centrale de LHCD est considérée, l'effondrement est reproduit. Si l'on tient compte uniquement de la réduction de l'absorption centrale de LHCD et de l'augmentation du facteur de refroidissement, le collapse se produit mais la vitesse de l'effondrement est plus faible que celle observée expérimentalement.
Par conséquent, trois effets se produisant simultanément sont nécessaires pour capturer la vitesse de la chute de $T_e(0)$: augmentation du facteur de refroidissement, réduction de l'absorption centrale LHCD et accumulation de tungstène.

En ce qui concerne le premier ingrédient, comme le facteur de refroidissement est directement lié à la température des électrons, une réduction initiale de T_e fait augmenter le facteur de refroidissement en induisant une nouvelle diminution de T_e, dans un cercle vicieux. L'absorption de l'onde hybride au centre diminue comme prévu dans un plasma plus froid car le pic du dépôt se déplace plus loin de l'axe avec la diminution de T_e central. Cela conduit à un bilan de puissance négatif dans le cœur qui initie l'effondrement de la température. En même temps, l'aplatissement de ∇T_e induit un aplatissement de ∇T_i par équipartition, et, si le transport du tungstène est principalement néoclassique, un aplatissement initial de T_e est nécessaire pour déclencher l'accumulation de W. Par conséquent, le profil du tungstène atteint un pic. Ensuite, lorsque le cycle vicieux est initié, les deux phénomènes se produisent simultanément (diminution de T_e central et accumulation de W). A la fin du collapse, un élargissement du profil de courant se produit (chute de l'inductance interne du plasma) et l'activité MHD se déclenche.

Malgré le fait qu'un grand pas en avant ait été fait pendant cette thèse concernant notre compréhension de la dynamique de l'effondrement, de nombreuses améliorations significatives peuvent encore être faites dans le futur.
Tout d'abord, le High Fidelity Pulse Simulator peut être utilisé pour modéliser WEST afin de simuler directement l'évolution de la densité du tungstène dans le temps.
Deuxièmement, en termes d'amélioration des performances de WEST, un chauffage central des électrons est crucial pour se situer, autant que possible, au-dessus de la plage de température dans laquelle le facteur de refroidissement du tungstène augmente avec des T_e plus faibles ($> 3keV$) . Ceci permet d'être plus résilient à une légère augmentation de la densité ; pour compenser le rayonnement du tungstène dans le cœur et donc de supporter des niveaux plus élevés de tungstène.
Dans les prochaines campagnes WEST, en utilisant LHCD, la température électronique centrale sera contrôlée en augmentant le rapport de la puissance injectée sur la densité.
Le chauffage des électrons centraux sera maximisé, grâce à des expériences dédiées sur l'ICRH ajustant la fréquence et la concentration en H minoritaire. À partir de 2023, le chauffage des électrons centraux sera complété par 1, puis 3 gyrotrons fournissant 3MW d'ECRH.

Acknowledgements

Tout d'abord, je tiens à remercier mon tuteur Jorge qui m'a suivi de la meilleure des façons possible pendant ces trois courtes années. Pour sa patience, son temps et ses connaissances qu'il a partagées avec moi. Je n'aurais pas pu demander un meilleur tuteur.
Après cela, j'irai dans l'ordre chronologique. Je tiens à remercier Gerardo de m'avoir permis d'entrer dans le monde de la fusion nucléaire. Pour m'avoir accueillie comme sa propre fille et pour m'avoir toujours aidée, ne serait-ce qu'en échangeant quelques mots autour d'un café.
Je tiens à remercier Jean-François qui me connaît depuis le plus longtemps et qui m'a encadré pour la première fois. Je te remercie de m'avoir accueilli en tant que stagiaire et de m'avoir soutenu même sur mon chemin en tant que doctorant.
Ensuite, les autres membres du fantastique "dream team" qui ont joué un rôle tout aussi important dans ce voyage. Clarisse, une femme inspirante, merci pour tout ton temps, tes conseils et ton aide. Pierre, merci de répondre à toutes mes questions stupides à tout moment. C'est un plaisir de pouvoir partager avec vous tous mon doctorat qui a été un long voyage, parfois avec quelques obstacles, mais avec le soutien de la meilleure équipe qui soit.
Je tiens à remercier toutes les personnes qui, à leur manière, ont contribué à cette thèse, aux articles et à mon parcours éducatif. En particulier, merci à Rémi, Patrick, Yves, Marc, Yannick, Nicolas et toute l'équipe de WEST.
Je suis également reconnaissant au CEA de m'avoir accueilli pendant mon doctorat et de m'avoir permis de connaître ce beau pays qui m'a hébergé pendant près de quatre ans, dans l'espoir que je puisse continuer à y contribuer.
Enfin, merci au jury d'avoir pris le temps d'évaluer et de juger mon travail, clôturant ainsi ce voyage qui restera éternellement dans mon cœur.
Merci à toutes les personnes que j'ai eu le plaisir de rencontrer au cours de mon doctorat. En particulier, merci à mon co-bureau Tullio notamment mon copain de ski ; merci à Silvia pour tous les cafés "scroccati" ; merci à Manuel, Alberto, Stefano, Rebecca et Daniela, qui, en plus d'être des collègues, continuent d'être de grands amis.
Merci à tout le groupe du "repas italien" qui m'a accueilli dès le premier jour où j'ai mis les pieds dans cet endroit.
Et enfin, et surtout parce que c'est la plus importante, un merci infini à Virginia, un amour au premier regard, une copine de travail et heureusement de nombreuses aventures, le meilleur cadeau que le CEA pouvait me faire.
Je tiens à remercier tous les amis qui ont contribué à ma vie et à mon épanouissement personnel au cours de ces années. Un merci spécial à Valeria, 9 mois ont suffi à faire de nous des amis pour la vie. Merci au groupe de pingouins alcoolisés Sveva, Heddy et

Lorenzo ; et merci à tout le reste de la compagnie : Giorgio, Lorenzo, Barbara, Chiara, Quentin et Michela.
Un merci spécial à mon meilleur ami Henry pour m'avoir appris une nouvelle langue et pour m'avoir supporté pratiquement tous les jours. Et pour conclure la "période française", je voudrais remercier Romain pour m'avoir redonné une grande partie de la confiance en moi que j'avais perdue pendant mon parcours et pour continuer à faire de moi une meilleure version de moi-même.
Je voudrais remercier tous mes amis de l'université qui, bien qu'éloignés, m'ont toujours accueillie et hébergée à chaque moment de l'année, pour m'aider comme eux seuls savent le faire : merci à Serena, Francesca, Fabio, Riccardo, Daniele, Selenia et Beppe.
Et tous mes meilleures amies qui ont toujours et pour toujours été à mes côtés à chaque étape de ma vie : merci à Silvia, Giorgia, Roberta et Chiara.
Enfin, je voudrais remercier et dédier toute cette croissance professionnelle et personnelle, tous les sacrifices et tous les bons moments à ma folle famille. Sans leur soutien, de mes premiers pas à aujourd'hui, rien n'aurait pu se passer. À ma mère, mon père et mon frère, les personnes les plus importantes de ma vie. Merci de toujours croire en moi et d'être une source constante d'inspiration.

Ringraziamenti

Prima di tutti vorrei ringrziare il mio tutor Jorge che mi ha seguita nel migliore dei modi in questi brevi tre anni. Per la sua pazienza, il suo tempo e le sue conoscienze che ha condiviso con me. Non potevo chiedere tutor migliore.
Dopo di cio andro in ordine cronologico. Vorrei ringraziare Gerardo per avermi permesso di entrare nel mondo della fusione nucleare. Per avermi accolta come una figlia e per avermi sempra aiutata, anche solo scambiando due parole davanti ad un caffe.
Vorrei ringraziare Jean-François, colui che mi conosce da piu tempo e colui che mi ha seguita per la prima volta. Grazie per avermi presa come stagista e per essermi stato accanto anche nel mio percorso da dottoranda.
Vorrei, poi, ringraziare gli altri componenti del fantastico "dream team" che sono stati altrettanto fondamentali in questo percorso. Clarisse, una donna fonte di ispirazione, grazie per tutto il tempo dedicato, per tutti i consigli e per tutto l'aiuto. Pierre, grazie per aver risposto a tutte le mie domande stupide in qualsiasi momento. E stato un piacere poter condividere con tutti voi il mio dottorato, che è stato un persorso lungo, a volte con qualche ostacolo, ma con il supporto del miglior team di sempre.
Vorrei ringraziare tutte le persone che a modo loro hanno contribuito a questa tesi, agli articoli e al mio persorso formativo. In particolare, grazie a Remi, Patrick, Yves, Marc, Yannick, Nicolas e a tutto il WEST team.
Sono inoltre grata al CEA per avermi ospitato durante il dottorato e per avermi permesso di conoscere questo bellissimo paese che mi ha accolta per quasi quattro anni, con la speranza di poter continuare a dare la mia contribuzione.
Grazie infine alla commissione per aver trovato il tempo di valutare e giudicare il mio lavoro, chiudendo questo percorso che rimmarrà per sempre del mio cuore.

Grazie a tutte le persone che ho avuto il piacere di conoscere durante il mio dottorato. In particolare grazie al mio co-bureau Tullio nonché mio compagno di sci ; grazie a Silvia per tutti i caffé “scroccati” ; grazie a Manuel, Alberto, Stefano, Rebecca e Daniela che oltre che colleghe continuano ad essere delle grandi amiche.
Ringrazio tutto il gruppo del “pranzo italiano” che mi ha accolto del primo giorno in cui ho messo piede in questo posto.
E per ultimo, sopratutto perché è la piu importante, un grazie infinito a Virginia, un amore a prima vista, compagna di lavoro e fortunatamente di tante avventure, il miglior regalo che il CEA potesse farmi.
Vorrei ringraziare tutti gli amici che hanno contibuito alla mia vita e crescita personale durante questi anni. Un grazie speciale a Valeria, 9 mesi sono bastati per renderci amiche a vita. Grazie al gruppo dei pinguini alcolizzati Sveva, Heddy e Lorenzo ; e grazie a tutto il resto della compagnia : Giorgio, Lorenzo, Barbara, Chiara, Quentin e Michela.
Un grazie particolare al mio migliore amico Henry per avermi anche insegnato una nuova lingua altre che a sopportarmi praticamente ogni giorno.
E per concludere il “periodo francese” vorrei ringraziare Romain per avermi ridato grand parte della fiducia in me stessa che avevo perso durante il mio percorso e per continuare a rendermi una versione migliore di me stessa.
Vorrei ringraziare tutti i miei amici dell’università che nonostante lontani mi hanno sempre accolta e ospitata in ogni mometo dell’anno, per aiutarmi come solo loro sanno fare : grazie a Serena, Francesca, Fabio, Riccardo, Daniele, Selenia e Beppe.
E tutte le mie migliori amiche che da sempre e per sempre saranno al mio fianco in ogni tappa della mia vita : grazie a Silvia, Giorgia, Roberta e Chiara.
Infine, vorrei ringraizare e dedicare tutto questo persorso di crescita professionale e personale, tutti i sacrifici e tutti i momenti belli alla mia pazza famiglia. Senza il loro supporto dai miei primi passi ad oggi niente sarebbe potuto accadere. A mia madre, mio padre e mio fratello, le persone più importanti della mia vita. Grazie per credere sempre in me e per essere una fonte di ispirazione costante.

Contents

List of Figures

List of Tables

1 Global energy context

1.1 Introduction of the chapter

In the following chapter the actual global energy context is presented.
With more emphasis nuclear energy is explained as a viable solution to the problem of the uncontrollable increase in energy demand and the decrease in current energy resources.
In particular, the processes involved in nuclear fusion are explained.
In addition, the different fusion devices are listed. Finally, since tokamaks are the current favourite machines for generating electricity through nuclear fusion, a brief history of these is given.

1.2 Energy needs

A worldwide energy shortfall is predicted within the next few decades due to the combination of steadily increasing demand and decreasing available energy sources. Moreover, if current policy and technology trends continue, global energy consumption and energy-related carbon dioxide emissions will increase up to 2050 as a result of population and economic growth.
The solution to the energy problem can come from a portfolio of options that includes improvements in energy efficiency, renewable energy, nuclear energy and carbon capture techniques.

As reported in the International energy outlook 2021 and in figure 1.1, liquid fuels remain the largest energy source in the Reference case, but renewable energy use grows to a similar level. The rise of renewables results from falling technology costs and changing government policies, which in turn support the electric power sector using renewable energy sources to meet the growing electricity demand [1].

Up to now, sustainable energy sources represent only 14% of the total energy supply. The biggest contributor is the hydro-power which constitutes to 70% of the global renewable electricity production, while solar and wind contribute at a very small scale to the energetic mix despite their strong increase in the past decades. However, they are not able to produce the necessary energy production density. The main problem of the renewable energy is due to their intermittent availability and the difficulty to store electricity. In fact, electricity generation from wind and solar (PV) plants is

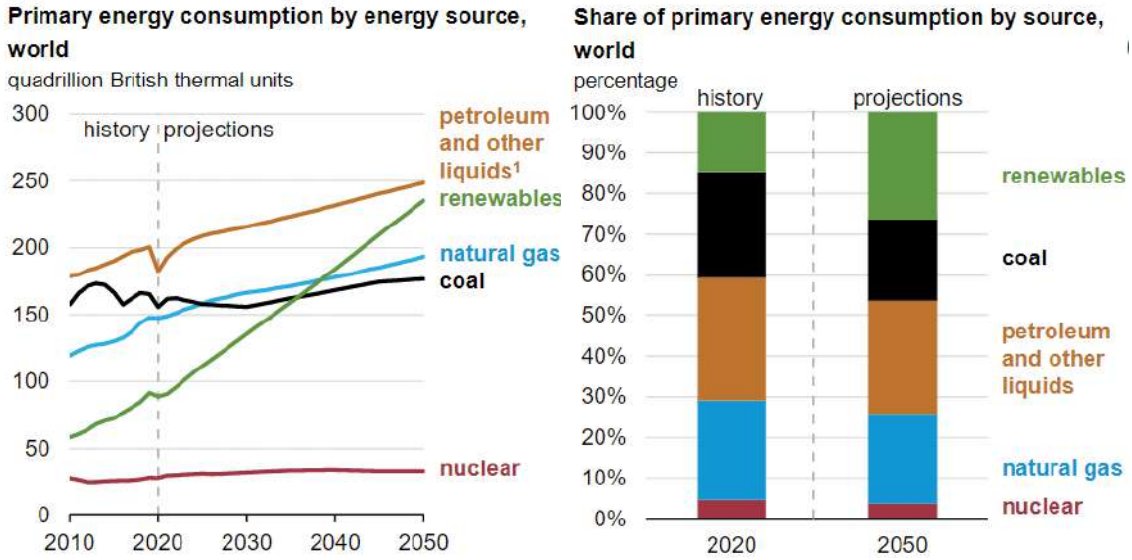

(a) Primary energy consumption by energy source, world, computed in 2020 and extrapolated up to 2050

(b) Share of primary energy consumption by source, world, computed in 2020 and extrapolated up to 2050

Figure 1.1 – U.S. Energy Information Administration, International Energy Outlook 2021 (IEO2021) Reference case

variable and depends on exogenous weather conditions, the time of day, season, and location. In addition, the potential temporal mismatch of supply and demand raises two fundamental questions: how to deal with variable renewable energy at times when there is too much supply, and how to serve demand at times when supply is scarce. [2]

Nuclear energy represents 5% of the energetic mix. France is the country with the biggest contribution of nuclear energy (~ 50% of our electricity comes from nuclear power plants) and produces 17% of the world nuclear energy.
Fission-based nuclear power has historically been one of the largest contributors of carbon-free electricity globally. Their potential to contribute to power sector decarbonisation is significant. In many jurisdictions nuclear power has trouble competing against other, more economic alternatives, such as natural gas or modern renewables [3]. Concerns over safety, waste storage and broader public acceptance also remain an obstacle to its development. However, to make a relevant contribution worldwide, fusion should aim to generate 1TW of electricity in the course of the 22nd century. It is not mentioned in the today worldwide energy mix since it is not yet a commercially available energy source, but a fusion-power nuclear reactor would offer significant advantages. In particular, fusion needs hydrogen isotopes to work. The abundance of deuterium leads to a negligible fuel supply problem. On the other hand, tritium supply still be a problem. Tritium, with a half-life of 12.3 years, exists naturally only in trace amounts in the upper atmosphere, the product of cosmic ray bombardment.

This problem can be shrug off if the future reactors breed the tritium they need. The neutrons released in fusion reactions can split lithium into helium and tritium if the reactor wall is lined with the metal [4]. Fusion would produce no air pollution or greenhouse gases during normal operation. The risk of accident for fusion reactor is much lower than for fission reactor (no chain reaction because the neutrons do not participate to the fusion reaction, therefore no risk of "divergence", hence of reaction-driven explosion) and in particular the risk to have external contamination is only related to the volatility of the tritium. This is mainly due to the negligible residual power during the shutdown of the reactor and low inventory of radioactive combustible. Hence, for these reasons, many techniques have been studied in various parts of the world to develop this kind of energy source and to make fusion a credible energy option. [5]

1.3 Nuclear fusion reaction

The nuclear fusion reaction consists in two light nuclei colliding to form an heavier nucleus and subatomic particles. Atomic nuclei are positively charged and so they repel each other. The only possibility to fuse is colliding so fast to overcome the electrostatic repulsion. This is the reason why the fusion fuel has to be heated to about 200 million of degrees. At this temperature, atoms are split into nuclei and electrons forming a gas of charged particles known as plasma.
The probability of overcoming the electrostatic repulsion is expressed in effective cross section. Figure 1.2 shows the effective cross sections for several fusion reactions depending on the interaction energy expressed in keV.

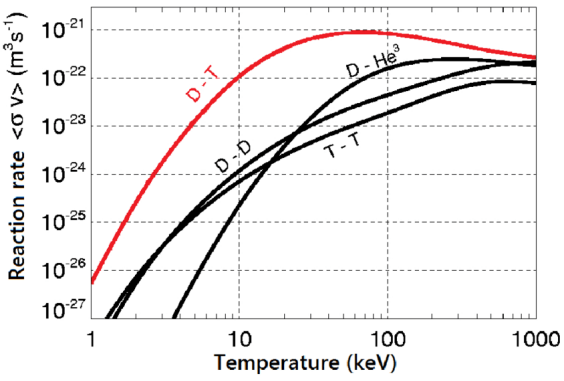

Figure 1.2 – Cross-sections of potential fusion reactions depending on interaction energy. [6]

Hydrogen isotopes are the perfect candidates for such reactions because Deuterium is abundant in oceans and their fusion cross sections are higher than the ones for other reactions at lower temperature making it able to be reached in terrestrial. The

combination Deuterium-Tritium (D-T), two hydrogen isotopes, offers by far the highest cross-section, with a maximum at ~ 66 keV. The D-T fusion reaction is written below:

$$ {}^{2}_{1}D + {}^{3}_{1}T \rightarrow {}^{4}_{2}He(3.5MeV) + {}^{1}_{0}n(14.1MeV) \tag{1.1} $$

Unlike Deuterium, Tritium is an unstable radioactive element with a half-life of 12.3 year, therefore it cannot be found in nature but it can be product in-situ thanks to a breading blanket.

In fusion reactors, we have to find ways to confine such plasmas to generate sufficiently energy to be profitable. There is also a permanent energy loss, compensated by external heating systems. The power loss is defined as $P_L = P_H + P_\alpha$, the sum of the external heating P_H and the thermonuclear power P_α, generated by the Helium particles. The goal is to reach ignition, when the plasma is self-heated thanks to the α-particles, such that external power heating is not required any more. This ignition point called the Lawson's criterion can be written as:

$$ n_i T_i \tau_e = 3 \times 10^{21} keV s m^{-3} \tag{1.2} $$

where n_i and T_i are respectively the ion density and temperature and τ_e is the energy confinement time. To reach this criterion, two main opposite ways have been explored: the inertial confinement consists in confining plasmas with high intensity lasers shooting uniformly on spherical fuel targets during a very short time ($10^{-11} s$) to reach densities of $10^{31} m^{-3}$ at temperature of 10keV. The second way is the magnetic confinement, involving lower densities ($10^{20} - 10^{21} m^{-3}$) at similar temperatures but for longer confinement time of the order of the second.
Nowadays, the last method is the most promising one to produce electricity and it has led to the tokamak machine concept.

1.4 Story of the tokamak

Tokamaks were initially conceptualized in the 1950s by Soviet physicists Igor Tamm and Andrei Sakharov. The first working tokamak was attributed to the work of Natan Yavlinsky on the T-1 in 1958 [7]. It demonstrated very high energy losses through radiation. This was traced to impurities in the plasma due to the outgassing from the copper container. In order to explore solutions to this problem, another small device was constructed, T-2 with an inner vacuum chamber (liner) made of corrugated metal that could be heated up to 550 Celsius degrees. [8]
The next major improvements were presented in 1968 thanks to two additional tokamak designs, TM-2 in 1965, and T-4 in 1968. [8]

By the late-1970s, tokamaks had reached all the conditions needed for a practical fusion reactor; in 1978 the Princeton Large Torus, PLT, had reached ignition compatible temperature but at low density. The next year the Soviet T-7 successfully used superconducting magnets for the first time.
During the 1970s, four major second-generation proposals were funded worldwide. The Soviets continued their development lineage with the T-15, while a pan-European effort was developing the Joint European Torus (JET) and Japan began the JT-60 effort (originally known as the "Breakeven Plasma Test Facility"). In the US, the Tokamak Fusion Test Reactor (TFTR) was built [9]. TFTR began operation in 1982, followed shortly by JET in 1983 and JT-60 in 1985. JET quickly took the lead in critical experiments, moving from test gases to deuterium and increasingly powerful "shots".
Some thought of an international reactor design had been ongoing since June 1973 under the name INTOR, for INternational TOkamak Reactor. [10]
The next year, an agreement was signed between the US, Soviet Union, European Union and Japan, creating the International Thermonuclear Experimental Reactor organization. Design work began in 1988, and since that time the ITER reactor has been the primary tokamak design effort worldwide. [11]
This led to the construction of more tokamaks around the world. In 1986 DIII-D in San Diego has been constructed, as well as the first superconducting tokamak in 1988, Tore Supra in France, FTU in 1990 in Italy and, one year later ASDEX in Germany. More recently EAST in China (2006) and JT-60SA in Japan (2015).

1.5 The way for fusion

The pragmatic approach on fusion energy is based on a realistic demonstration that fusion is able to produce electricity. In order to reach the goal three main elements are necessary:

— The ITER project as the essential step towards energy production;

— A single step between ITER and the commercial fusion power plant design, DEMO;

— The International Fusion Materials Irradiation Facility (IFMIF) for materials qualification under intense neutron irradiation.

Moreover, a numerous private companies working on controlled fusion with alternative projects.
Anyway, ITER is the key facility of the fusion energy. ITER will be the first magnetic confinement device to produce a net surplus of fusion energy. It is designed to generate 500 MW of fusion power. As the injected power will be 50MW, this corresponds to a fusion gain Q=10. ITER will also demonstrate the main technologies for a fusion

power plant. It is currently being built in Cadarache (France), in the framework of a collaboration between China, Europe, India, Japan, Korea, Russia and the USA. [12]
The milestones for ITER are explained into the European Research Roadmap to the Realization of Fusion Energy (Ref [5]) in which the next stellarator generation and the DEMO scenarios are also prepared. The ITER roadmap is based on eight missions and the Mission 1 and 2 are in particular connected to the tokamak program. Mission 1 is based on the tokamak configuration and has to provide the basis for plasma regimes operations. ITER has to achieve the headline missions of Q=10 (inductive regime) and Q=5 (steady-state regime). In order to mitigate the risk of ITER failure, accompanying scientific programmes on small and medium sized tokamaks are necessary. In addition, two very large tokamaks (still smaller than ITER) are or will be exploited on the framework of the EU fusion research: JET, the Joint European Torus located at Culham Center in Oxford, is used to validate the inductive regimes and operation with D-T in high performance and tungsten environment, while JT-60SA, located at Naka Fusion Institute in Japan, is mainly devoted to high performance steady-state regimes. The third in size is WEST operating in steady-state and tungsten environment, used also to investigate the problem of the heat exhaust.
Mission 2 consists of reducing the heat load on the divertor targets by radiating a sufficient amount of power from the plasma and by producing “detached” divertor conditions. A dedicated test on specifically upgraded existing facilities or on a dedicated Divertor Tokamak Test (DTT) facility will be necessary.

2 General introduction

2.1 Context of this PhD

In this chapter all the theory necessary to understand the context of this PhD is described.
The work accomplished during the PhD concerns WEST data analysis. The work had two different main purposes: first, a data analysis in the context of large aspect ratio and high tungsten radiation plasmas has been performed; second, a dynamical radiation collapse has been analysed and modelled.
For both of these purposes, a set of knowledge is necessary.

In particular, for the large aspect ratio and high tungsten radiation plasmas studies, the starting point is the reconstruction of the plasma equilibrium. This is a fundamental step to introduce the energy confinement time of a tokamak.
This latter quantity is used to extrapolate plasma performances. Therefore, the theory of the scaling law in a fusion device is explained, in both dimensional and dimensionless parameters. The scaling law includes both the aspect ratio and the total power, useful for analysing the impact of these two quantities on energy confinement time itself. Moreover, all the statistical techniques used in this work are summarized. All of these knowledges are useful as a theoretical basis for the first part of this thesis, which focuses on analysing the performance of WEST and its comparison with other L- mode tokamaks. The aim of the work is to check if WEST L-mode confinement is well aligned with the other tokamaks and to investigate the aspect ratio effect on L mode confinement. WEST is well suited for this analysis because it is characterized by an aspect ratio large compared to other tokamaks.
The entire analysis concerning this first objective can be found in Chapter 3.

Since, in WEST operation, a radiative collapse of the central electron temperature is observed during some pulses in which this collapse degrades the confinement and lead to MHD instability, the second objective is to reproduce thanks to integrated modelling this phenomena in order to avoid it.
For this purpose, the transport in a plasma is described, both neoclassical and turbulent transport, since the high Z particles such as tungsten are influenced by both. Then, a general overview on the importance of integrated modelling is given. At the end, a general description of WEST is given.
Details on the second objective of the work can be found in Chapters 4 and 5.

2.2 Reconstruction of plasma equilibrium

The reconstruction of the equilibrium of a plasma in a tokamak is a free boundary problem described by the Grad-Shafranov equation in axisymmetric configuration [13]. This equation is a two-dimensional, nonlinear, elliptic partial differential equation obtained from the reduction of the ideal Magneto Hydro Dynamics (MHD) equations [14] to two dimensions.
The plasma is confined by magnetic field that is not sufficient alone. In order to have an equilibrium in which th eplasma pressure is balanced by the magnetic forces it is necessary also to have a poloidal magnetic field that is produced mainly by current in the plasma itself.
Starting from the hypothesis that a thermonuclear plasma can be naturally considered as a mixture of at least two species (ions and electrons considered as a single fluid) the set of equations that describe MHD are a combination of the Navier–Stokes equations of fluid dynamics (continuity, momentum and energy balance equations) and Maxwell's equations of electromagnetism:

$$\frac{\partial \rho}{\partial t} + \nabla \cdot (\rho \boldsymbol{v}) = 0 \tag{2.1}$$

$$\rho(\frac{\partial}{\partial t} + \boldsymbol{v} \cdot \nabla)\boldsymbol{v} = \boldsymbol{J} \times \boldsymbol{B} - \nabla \boldsymbol{P} \tag{2.2}$$

$$\frac{d}{dt}(\frac{p}{\rho^{\gamma}}) = 0 \tag{2.3}$$

$$\boldsymbol{E} + \boldsymbol{v} \times \boldsymbol{B} = 0 \tag{2.4}$$

$$\frac{\partial \boldsymbol{B}}{\partial t} = -\nabla \times \boldsymbol{E} \tag{2.5}$$

$$\mu_0 \boldsymbol{J} = \nabla \times \boldsymbol{B} \tag{2.6}$$

$$\nabla \cdot \boldsymbol{B} = 0 \tag{2.7}$$

where bold indicates vectors, ρ is mass density, v is fluid velocity ($\boldsymbol{v} = \frac{1}{n}\int f(\boldsymbol{x}, \boldsymbol{v}', \boldsymbol{t})\boldsymbol{v}' d\boldsymbol{v}'$ where $f(\boldsymbol{x}, \boldsymbol{v}, \boldsymbol{t})$ is the distribution function depending on space, velocity and time and $\boldsymbol{v}'$ is the particle velocity), J is current density, B the magnetic fields, P is plasma pressure, E represents the electric magnetic field and μ_0 is vacuum permeability.
Going from the first to the last equation, we have the continuity , the momentum and the energy conservation equations and the Ohm's, the Faraday's and the Ampere's law and the magnetic divergence.
The plasma can be confined by a proper equilibrium of plasma pressure and magnetic field.
Thanks to the axisymmetry, there is no dependence with respect to the toroidal direction, therefore, the spatial derivatives of physical quantities with respect to ϕ are zero. [15]

Therefore, it is possible to define the poloidal flux function, that is the total flux

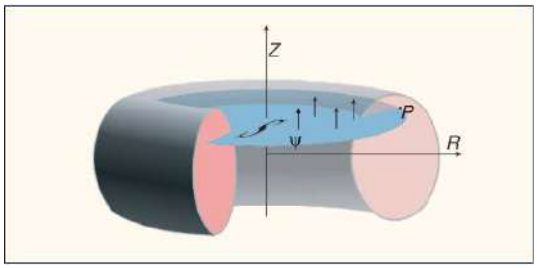

Figure 2.1 – Definition of poloidal flux function.

through the surface S(r,z) bounded by the toroidal ring passing through a point P 2.1, as:

$$\Psi(r,z) = r\,A_\phi(r,z) \tag{2.8}$$

Where $A = \frac{R_0}{\lambda}$ (the parameter λ is a scaling factor used to ensure that the given total current value Ip is satisfied and R_0 the major radius).
Assuming an azimuthal symmetry about the z-axis of a cylindrical coordinate system, it is possible to derive the Grad-Shafranov equation.

$$\nabla(\frac{1}{r^2}\nabla\Psi) + 4\pi^2\mu_0 P' + \frac{\mu_0^2}{r^2} I' I = 0 \tag{2.9}$$

where, P is the plasma pressure, $I = R \times B_\phi(\phi)$ and (r,ϕ,z) are respectively the radial, toroidal and vertical coordinate as shown in the figure 2.2.

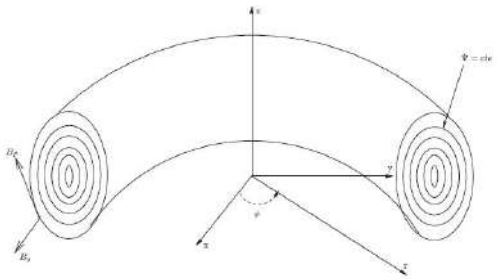

Figure 2.2 – Toroidal geometry of a plasma column.

The Grad-Shafranov equation is non-linear equation in Ψ because it involves three independent quantities Ψ, $P(\Psi)$ and $I(\Psi)$, therefore, it cannot be solved analytically in general cases without assumptions. There exist a limited number of analytic solutions, one of them is the Solov'ev solution. It assumes that the pressure is a linear function of Ψ ($P = P_0 + \lambda\Psi$) and the plasma current is constant inside the plasma ($I' = 0$).
Under these assumptions, Grad-Shafranov equation is reduced to:

$$r\frac{\partial}{\partial r}(\frac{1}{r}\frac{\partial \Psi}{\partial r}) + \frac{\partial^2 \Psi}{\partial^2 z} + 4\pi^2 r^2 \mu_0 \lambda = 0 \tag{2.10}$$

Which has the exact solution:

$$\Psi(r,z) = \Psi_0 \frac{r^2}{r_0^4}(2r_0^2 - r^2 - 4\alpha^2 z^2) \tag{2.11}$$

Where Ψ_0 , r_0 and α are constants. For the case of $\alpha = 1$, the contour plot of Ψ exhibits open curves going to $z = \pm\infty$ (for any negative value of Ψ), concentric closed curves (for any positive value of Ψ) and a single curve called the separatrix (if $r^2 + 4\alpha^2 z^2 = 2r_0^2$).
Substituting the poloidal flux function in the Grad-Shafranov equation leads to:

$$\lambda = \frac{2\Psi_0}{\pi^2 r_0^4 \mu_0}(1+\alpha^2) \tag{2.12}$$

Then, the pressure is:

$$P(\Psi) = P_0 + \frac{2\Psi_0}{\pi^2 r_0^4 \mu_0}(1+\alpha^2)\Psi \implies P(\Psi) = P_0 + \frac{2\Psi_0}{\pi^2 r_0^4 \mu_0}(1+\alpha^2)[\Psi - \Psi_{edge}] \tag{2.13}$$

The pressure is needed to compute the energy stored in the plasma.

2.3 Energy confinement time

The best way to quantify the tokamak performance is the estimation of the tokamak energy confinement time. The concept was first developed by John D. Lawson in 1955. As originally formulated, the Lawson criterion gives a minimum required value for the product of the plasma (electron) density n_e and the energy confinement time that leads to net energy output.
The energy confinement time is computed as the ratio between the plasma energy content and the total injected power in the machine. It is the time scale on which plasma energy would decay if heatings were switched off. The general expression of the confinement time for a time evolving plasma is [16]:

$$\tau_E = \frac{W}{P_{aux} + V_{loop} I_p - \dot{W} - X} \tag{2.14}$$

With

$$V_{loop} I_p = P_{ohm} \tag{2.15}$$

$$\dot{W} = \frac{dW}{dt} \tag{2.16}$$

$$X = \frac{1}{\mu_0} \int_U [B_p \dot{B}_p + B_\phi^{plasma} (\dot{B}_\phi^{vacuum} + \dot{B}_\phi^{plasma})] dv \tag{2.17}$$

Where P_{aux} is the external heating power, V_{loop} is the loop voltage, I_p is the plasma current, W is the plasma energy, P_{ohm} is the ohmic power, U is the surface occupied by the plasma and B_p and B_ϕ are the poloidal and toroidal components of the magnetic field. The dot indicates the derivative with respect to time. Therefore, X contains the rate of change of poloidal magnetic field energy inside the plasma, and a part of the toroidal field energy.
In steady-state equilibria $B_T B_P$ and I_p are constant and $X = 0$.
Confinements is limited by thermal conduction and convection process but radiation is also a source of energy loss.

The plasma energy content W is difficult to calculate and there exist different methods to compute it. One of them consists on solving the Grad-Shafranov equation (assuming that the pressure is a linear function of Ψ and the plasma current is constant inside the plasma), finding the total plasma pressure P and integrating over the plasma volume to compute W. In this case the plasma MHD energy content, W_{mhd}, is computed as:

$$W_{mhd} = \frac{3}{2} \int_V P dV \tag{2.18}$$

To compute the plasma energy content by the MHD equilibrium reconstruction, the reconstruction of the poloidal flux function, the plasma boundary and the two non-linear source term p' and II' in the Grad-Shafranov (formula 2.11) equation are needed. The magnetic probes and the flux loops which provide values of the poloidal magnetic field and the flux at several points surrounding the vacuum vessel and the plasma are used for the numerical equilibrium reconstruction [17]. The principle is to determine the flux linking the coil from the induced voltage V [18]:

$$\mathbf{\Phi} = -\int_{t_0}^{t} V(t') dt' \tag{2.19}$$

and to calculate the average value of the normal component of the magnetic field B from the flux using:

$$\boldsymbol{B} \cdot \boldsymbol{n} = \frac{\mathbf{\Phi}}{NA} \tag{2.20}$$

where N is the number of turns of the coil and A is the average area.
In order to be able to separate the contribution of p' and II' it is necessary to use the polarimetry. The latter consists in measurements of the change of state of polarization of an electromagnetic radiation propagating across the magnetized plasma along several lines of sight distributed on the poloidal section of the tokamak [17]. For propagation parallel to a magnetic field in a plasma, there is a difference in the refractive indices of right and left circularly polarized rotation, arising from the gyration of the plasmas electrons. The difference in the refractive indices gives rise to a rotation of the polarization vector known as Faraday effect. The angle of rotation is given by:

$$\Theta_F = \frac{\lambda^2 e^3}{8\pi^2 c^3 \epsilon_0 m_e^2} \int n_e B_{||} dl \tag{2.21}$$

where dl is an element of the length of the loop, λ is the wavelength, e is the electron electric charge, c is the velocity of light, m_e is the electron mass, n_e the electron density and $B_{||}$ the parallel magnetic field. The formula 2.21 can be used to measure the internal poloidal magnetic field [19].

Another method to compute the energy content consists in measuring T_e, n_e and T_i profiles. This one gives the plasma thermal energy content, W_{th} computed as:

$$W_{th} = \frac{2}{3}\int_V P_{th} dV = \frac{3}{2}\int_V n(T_i + T_e) dV \tag{2.22}$$

In this expression a single ion and quasi-neutrality are assumed ($n_e \approx n_i$).

It is possible to define different τ according to how the plasma energy content is computed. Therefore, three plasma energy contents are defined:

— W_{tot} = global energy content including fast particles energy;

— W_{th} = thermal energy content without fast particles energy;

— W_{mhd} = total energy content determined by an MHD equilibrium reconstruction.

Regarding the power, it can be defined in different ways depending on the definition of plasma energy content chosen. Therefore, it is defined as [20]:

— P_L = total heating power corrected for $\frac{dW_{tot}}{dt}$;

— P_{TH} = total heating power corrected for $\frac{dW_{th}}{dt}$ and for charge exchange;

— P_{MHD} = total heating power corrected for $\frac{dW_{mhd}}{dt}$;

They are used as denominator in the calculation of the energy confinement time. Therefore, the definition and the value of the energy confinement time depends on which energy content and power is chosen for the calculation. In particular, three τ are defined:

— $\tau_E = \frac{W_{tot}}{P_L}$;

— $\tau_{th} = \frac{W_{th}}{P_{TH}}$;

— $\tau_{mhd} = \frac{W_{MHD}}{P_{MHD}}$

2.4 Scaling law in fusion devices

The global energy confinement time scaling law is a key tool that allows extrapolating towards ITER and DEMO. To do that, a database with a large number of entries is necessary. Therefore, many different discharges from different size and shape tokamaks contribute to joined databases. Different databases exist for specific operating regimes such as L-mode and H-mode. When a magnetically confined plasma is heated above a threshold, it may spontaneously transition from a low confinement (L-mode) state to a high confinement (H-mode) state. In the H-mode, the energy confinement time is significantly enhanced (typically by a factor of 2)[21]. The change in confinement is first apparent at the age of the plasma where there is a rapid increase in the pressure gradient mainly due to an increase in edge density. The associated improvement in the edge confinement can be thought of as a transport barrier. When this barrier appears it produces an increase in density over the whole plasma on the timescale of the confinement time, with some further improvement of confinement in the bulk.
Once the database has been constructed the empirical scaling is applied. The common form of scaling law consists in a power law and it includes several engineering plasma parameters [20]:

$$\tau = C I_p^{\alpha_{Ip}} B^{\alpha_B} P_{tot}^{\alpha_{P_{tot}}} n_e^{\alpha_{n_e}} M^{\alpha_M} R^{\alpha_R} \epsilon^{\alpha_\epsilon} k^{\alpha_k} \tag{2.23}$$

Where I_p is the plasma current in MA, B is the toroidal magnetic field in T, P_{tot} is the total power in MW, n_e is the line average electron density in $10^{19} m^{-3}$, M is the average ion mass in atomic mass units, R is the major radius in m, $\epsilon = \frac{1}{A}$ is the inverse aspect ratio (where $A = \frac{R}{a}$ where a is the minor radius in m) and $k = \frac{b}{a}$ is the plasma elongation (see figure 2.3 for the derivation of all plasma geometrical parameters).

Dimensionless parameter scaling technique is a robust method for obtaining qualitative and quantitative information about complex physical system. This technique is useful when a mathematical model describing the quantity of interest does not

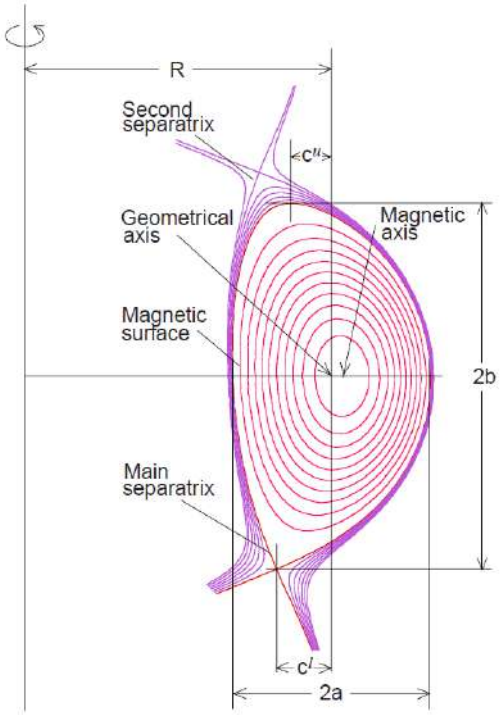

Figure 2.3 – Cross section of the tokamak magnetic configuration

exit yet. If a set of parameters that are believed to determine the behaviour of this quantity can be written down, then, application of established techniques for finding appropriate dimensionless parameters can provide significant information on the relationship among the original set of engineering parameters. Also in the case where the governing equations are established, but they are impossible to solve analytically or numerically in the situation of interest, the use of dimensionless parameter scaling techniques can lead to the identification of a few key parameters that characterize the behaviour of the system.
The most common dimensionless analysis is the Buckingham theorem or the Π theorem. It is used to determine the number of dimensionless groups required to describe a phenomena. According to this theorem, "the number of dimensionless groups to define a problem is equal to the total number of variables (n) minus the fundamental dimensions (k)". Any physical system can be described by an equation of the general form:

$$f(q_1, q_2, ..., q_n) = 0 \tag{2.24}$$

where the q_i are the n independent physical variables, and they are expressed in terms of k independent physical units. Then the above equation can be restated as:

$$f(\pi_1, \pi_2, ..., \pi_p) = 0 \tag{2.25}$$

where the π_i are dimensionless parameters constructed from the q_i by $p = n - k$ dimensionless equations of the form:

$$\pi_i = q_1^{\alpha_{i,1}} q_2^{\alpha_{i,2}} ... q_n^{\alpha_{i,n}} \tag{2.26}$$

where the exponents a_i are rational numbers [22].
Dimensional analysis of the type of the Π theorem was first applied to tokamak plasmas by Kadomtsev [23]. The dimensional plasma parameters to describe the tokamak $\{a, R, B, B_p, c, e, m_e, m_i, T_i, T_e, n, \mu_0\}$ are set, where B_p is the poloidal magnetic field, c is the speed of the light in vacuum, e is the charge of the electron, m_e and m_i are the mass of the electron and of the ion and T_e and T_i are the electron and ion temperature. Four ratios of like parameters are noted immediately:

$$\{r\} = \{\frac{R}{a}, q, \frac{m_e}{m_i}, \frac{T_e}{T_i}\} \tag{2.27}$$

Then, the number of independent dimensionless variables is reduced to eight since the number of dimensions is four (mass, length, time, electron current). Applying Buckingham theorem the eight dimensionless variables are:

— Poloidal ion Larmor radius normalized to machine size $\rho_* = \frac{\rho_{p_i}}{a}$;

— Normalized collision frequency $\nu_{mfp} = \frac{qR}{\lambda_c}$ with λ_c the electron mean free path defined as the product of the Debye length and the number of particles in the Debye sphere;

— Ratio of kinetic to poloidal magnetic pressure $\beta_p = \frac{2\mu_0 nT}{B_p^2}$;

— Number of particles in Debye sphere $N = (\frac{4\pi}{3})\lambda_D^3 n$;

— Aspect ratio: $\frac{R}{a}$;

— Temperature ratio: $\frac{T_e}{T_i}$;

— Safety factor: $q = \frac{aB}{RB_P}$;

— Mass ratio: $\frac{m_e}{m_i}$

If the equations governing the behaviour of a plasma are assumed to be known, the technique of scale invariance can be used to derive the necessary dimensionless relationships between the variables that appear in the equations. Connor and Taylor formalized this analysis to obtain the scaling of a confinement time in several different limits [24]. Assuming that quantum physics can be neglected, in the electrostatic, collisionless limit, the plasma is assumed to be described by the Vlasov equations for

the distribution functions f_j of electrons ($j = e$) and ions ($j = i$) [25]:

$$\frac{\partial f_j}{\partial t} + \boldsymbol{v} \cdot \nabla f_j + \frac{e_j}{m_j}(\boldsymbol{E} + \boldsymbol{v} \times \boldsymbol{B}) \cdot \frac{\partial f_j}{\partial \boldsymbol{v}} = 0 \qquad j = i, e \tag{2.28}$$

where e_j and m_j are the charge and the mass of each component of the plasma and v is the particle velocity. B is the fixed magnetic field and the electrostatic field E is determined by the quasi-neutrality condition:

$$\sum_j e_j \int d^3 v f_j = 0 \tag{2.29}$$

The principle of scale invariance considers the scale transformations of the form:

$$f_j \to \alpha f_j, \qquad v \to \beta v, \qquad x \to \gamma x, \qquad t \to \delta t, \qquad E \to \mu E, \qquad B \to \nu B \tag{2.30}$$

In these transformations each of the variables is multiplied by power of the scale factor such that the equation remains unchanged. There are three independent transformations of this type that may be expressed as:

$$A_1 \qquad f_j \to \alpha f_j, \tag{2.31}$$

$$A_2 \qquad v \to \beta v, \quad B \to \beta B, t \to \beta^{-1} t, \quad E \to \beta^2 E \tag{2.32}$$

$$A_3 \qquad x \to \gamma x, \quad B \to \gamma^{-1} B, \quad t \to \gamma t, \quad E \to \gamma^{-1} E \tag{2.33}$$

The particular specifications A_1 through A_3 are arbitrary to the extent that any three independent products of these transformations would also leave equations (2.28) and (2.30) invariant. Now the scale invariance principle implies that any variable derived from these equations, such as a confinement time, must transform appropriately under A_1 through A_3.
Consider a power-law scaling for the confinement time of the form:

$$\tau = n^p T^q B^r a^s \tag{2.34}$$

Recalling the definitions:

$$n = \int d^3 v f \qquad nT = \int d^3 v (\frac{m v^2}{3}) f \tag{2.35}$$

The transformations A_1 to A_3 can be substituted in turn in equation 2.34. Equating the powers of α, β and γ on the two sides of the resulting equations then provides three constraints on the indices p, q, r and s:

$$p = 0, \qquad 2q + r = -1, \qquad s - r = 1 \tag{2.36}$$

Therefore, only the index q is independent and:

$$B\tau = F(\frac{T}{a^2 B^2}) \tag{2.37}$$

For the left-hand side of this last equation the cyclotron frequency $\Omega = \frac{e_j B}{m_j}$ provides a convenient normalization, since it has the correct units and is proportional to B. The quantity in the parenthesis on the right-hand side scales like the square of the gyroradius $\rho = \frac{\sqrt{T m_j}}{e_j B}$ normalized to the physical size of the plasma a.
The above result may be extended to include the effects of collisions by the addition of a Fokker–Planck operator into the Vlasov equations. Finite β effects may be included by introducing a self-consistent magnetic field that satisfies the Maxwell equations. The dimensionless confinement time then has the more general form:

$$\Omega\tau = F(\rho_*, \nu_*, \beta, \{r_i\}) \tag{2.38}$$

where the r_i are ratios of quantities with like dimensions.

The standard set of dimensionless parameters characterizing energy and particle transport can be identified, consistently with both the dimensional analysis of Kadomtsev and the scaling invariance approach of Connor and Taylor. Therefore, the scaling of the confinement time with dimensionless parameters can be written as [26]:

$$\Omega_i \tau = \rho_*^{\chi_{\rho_*}} \beta^{\chi_\beta} \nu_*^{\chi_{\nu_*}} q^{\chi_q} M^{\chi_M} B^{\chi_B} \epsilon^{\chi_\epsilon} k^{\chi_k} \tag{2.39}$$

Since τ_E (2.23) scales with the four dimensional variables $(\hat{n}, \hat{T}, R, B)$ only, then $\omega\tau_E$ is expected to scale with (ρ_*, ν_*, β) only. Because the number of variables reduces from four to three, the power exponent of the fourth variable has to vanish in the transformation $\tau_E = G(\hat{n}, \hat{T}, R, B) \rightarrow \omega\tau_E = H(\rho_*, \nu_*, \beta, B^0)$
Therefore, applying the Kadomtsev transformation, it is possible to shift from the dimensional coefficients to the dimensionless ones such that: [27]

$$\chi_M = \frac{5\alpha_M + 3\alpha_R + 3\alpha_I + 4\alpha_P - \alpha_n}{5(1 + \alpha_P)} \tag{2.40}$$

$$\chi_k = \frac{\alpha_k + \alpha_P}{1 + \alpha_P} \tag{2.41}$$

$$\chi_\epsilon = \frac{2\alpha_\epsilon - 3\alpha_R + \alpha_I - 5\alpha_P + 2\alpha_n}{2(1 + \alpha_P)} \tag{2.42}$$

$$\chi_q = \frac{\alpha_R + 3 - 4\alpha_I + 3\alpha_P - 2\alpha_n}{5(1 + \alpha_P)} \tag{2.43}$$

$$\chi_\rho = \frac{2(-3\alpha_R + 3\alpha_I - 9\alpha_P + \alpha_n)}{5(1 + \alpha_P)} \tag{2.44}$$

$$\chi_\nu = \frac{-\alpha_R - \alpha_I - 3\alpha_P + 2\alpha_n}{5(1 + \alpha_P)} \tag{2.45}$$

$$\chi_B = \frac{5 + 5\alpha_B - 4\alpha_R + \alpha_I + 3\alpha_P + 8\alpha_n}{5(1 + \alpha_P)} \tag{2.46}$$

Kadomtsev constraint imposes $\chi_B = 0$. [23]

To analyse the impact of each parameters on the energy confinement time, a large database based on different tokamaks is needed.
The first L-mode database was initiated in the early eighties by S. Kaye [20]. It led to the ITER89-P scaling. The present L-mode database consists of 2938 observations from 14 tokamaks: Alcator C-mod (CMOD), ASDEX, DIII, D3D, FTU, JET, JFT2M, JT-60U, PBXM, PDX, TEXTOR, TFTR, Tore Supra (TSUPRA) and T10. Only 1881 points are in L-mode phase. The number of entries for the scaling analysis of τ_E (ITER89-P) is 1798, while, the number of discharges available for the τ_{th} (ITER96-L) scaling analysis is 1312. Moreover, the following assumption are taken into account:

— only L-mode pulses are selected;

— the fast ions energy content is ≤ 40%;

— discharges with electron preferential heating are selected ($\frac{P_{ohm}+P_{icrh}+P_{ecrh}+P_{lh}}{P_{tot}} \geq 0.5$)

In the table 2.1, the coefficients obtained applying a linear regression to ITER89-P and ITER96-L (both dimensional and dimensionless) databases are summarized [20]. The α_R exponent for both scaling laws has been modified so that the scaling laws fulfill the Kadomtsev constraint as suggested in [[28], p 2206].

Parameters	**ITER89-P**	**ITER89-P (dim.less)**	**ITER96-L**	**ITER96-L (dim.less)**
Constant	0.037	-	0.023	-
I_p	0.74	-	0.96	-
B_T	0.02	0	0.03	0
k	0.67	1.95	0.64	3.74
R	1.69	-	1.83	-
A	-0.31	0.25	0.06	0.04
n_e	0.24	-	0.40	-
M_{eff}	0.26	0.57	0.20	0.67
P	-0.57	-	-0.73	-
ρ_*	-	-1.93	-	-1.85
ν_*	-	-0.13	-	0.19
β	-	-0.63	-	-1.41
q	-	-1.59	-	-3.74
$RMSE$	16%	16%	15.8%	15.8%
R^2	0.98	0.98	0.97	0.97
Entries	1798	1798	1312	1312

Table 2.1 – scaling coefficients for ITER89-P and ITER96-L (dimensional and dimensionless)

An extended version of the H-mode database formed the basis of the such scaling expression as ITERH92-P(y) and ITERH93-P scaling, describing the global thermal energy confinement time in ELMy and ELM free discharge respectively. The assembly of the latest version of the ITER H-mode confinement database (ITERH.DB3) was completed in September 1997. This version contains 3813 entries from 18 tokamaks: ASDEX Upgrade (AUG), COMPASS-D, JET, TCV, TEXTOR, JFT2M, JT-60U, MAST, NSTX, START, T10, TdeV, Alcator C-MOD, D3D, PBXM, PDX and TUMAN-3M. Recently, experimental evidence has been collected suggesting that the coverage by the standard subset of the database, on which the IPB98(y,2) scaling is based, may be improved in certain regions of the parameter domain expected to be relevant for operation of future fusion reactors. Therefore, a new version of this database has been published in 2015 [29].
The selection criteria for the new version still are the same of the ITERH.DB3 version and they are [30]:

— H-mode data only;

— Pellet discharges are excluded (injection of high speed pellets of frozen hydrogen isotopes directly into the plasma core);

— No discharges with strong internal transport barriers (no formal definition for

such a criterion exists);

— Steady state energy content $-0.05 \leq \frac{(\frac{dW'}{dt})}{P} \leq 0.35$. For TFTR this is relaxed to $-0.10 \leq \frac{(\frac{dW'_{mhd}}{dt})}{P} \leq 0.35$;

— Total radiated power less than 60% of the injected power;

— $q_{95} \geq 3$;

— fast particles carrying less than 40% of the total plasma energy. For TFTR this constraint is ignored;

— Plasmas well below the β limit ($\beta_{\max} = \frac{\beta_N I}{aB_0}$, where I is the plasma current, B_0 is the external magnetic field, and a is the minor radius of the tokamak. β_N was determined numerically, and is normally given as 0.028. It changes dramatically with the shape of the plasma);

— Ratio of core ion and electron temperatures not more than 2.5, $0.04 \leq \frac{T_i(\psi=0)}{T_e(\psi=0)} \leq 2.5$;

— No hot ion H-mode ($T_i > T_e$);

— Internal inductances lower than 2 ($l_i(3) = \frac{2V\langle B_\theta^2\rangle}{\mu_0^2 I^2 R_0}$).

If the ELMy H-mode discharges are selected, such scaling is known as IPB98(y,2), otherwise, if the ELM free H-mode are chosen, the scaling is called ELM free H-mode scaling expression.
It is important to remind that for these scaling laws the elongation is defined as $\frac{S_{area}}{\pi a^2}$ (where S_{area} is the area of the plasma cross section and a the minor radius).
Also, a pure gyro-Bohm (local ion heat diffusivity is proportional to $\chi_{GB} = \rho_* \chi_B$ where $\chi_B = \frac{cT}{eB}$, here c, T, e, B are, respectively, speed of light, electron temperature, electric charge of electrons, and magnetic field) and electrostatic scaling which gives a better representation of the data compared to ITER98(y,2) exists and it is known as DS03 scaling. It is derived from the ELMy H-mode database but selecting only the pulses with ion mass equal to 2 [31].
In the table 2.2 the coefficients for both dimensional and dimensionless parameters of the three scaling are reported [30].

A general comment is that for both L-mode and H-mode scalings a power degradation of the confinement is always observed in a range of $P^{-0.5/-0.7}$, as well as a positive trend with respect to the plasma current above $I_p^{0.7}$. The dependence of the elongation is still positive, while the aspect ratio coefficient varies from positive to negative value. Concerning the $\rho_\star$ coefficient, it is almost -3 for the H-mode database, confirming a gyro-Bohm-like.

Param.	**IPB98(y,2)**	**IPB98(y,2) (dim.less)**	**DS03**	**DS03 (dim.less)**	**ELM free**	**ELM free (dim.less)**
Const.	0.0562	-	0.028	-	0.031	-
I_p	0.93	-	0.83	-	0.94	-
B_T	0.15	0	0.07	0	0.27	0
k	0.78	3.29	0.75	2.29	0.68	2.97
R	1.97	-	2.11	-	1.98	-
A	-0.58	-0.73	-0.30	1.30	-0.10	0.46
n_e	0.41	-	0.49	-	0.34	-
M_{eff}	0.19	0.14	0.20	0.81	0.43	1.82
P	-0.69	-	-0.55	-	-0.68	-
ρ_*	-	-2.68	-	-3.00	-	-2.90
ν_*	-	-0.01	-	-0.14	-	-0.12
β	-	-0.90	-	0	-	-0.97
q	-	-3.00	-	-1.71	-	-2.86
$RMSE$	15.6%	15.6%	34%	34%	15.6%	15.6%

Table 2.2 – scaling coefficients for IPB98(y,2), DS03 and ELM free H-mode (dimensional and dimensionless)

Although it is the most widely used technique for extrapolating the performance of future reactors, and statistical analysis can yield great results, it is important to bear in mind that the quantities of inputs are not truly linearly independent. Linear regression may lose its significance if the parameters show a large correlation. Among these is the known correlation between density and plasma current.

2.5 Statistical techniques

As explained in the previous section, scaling laws are widely used to study the performance of fusion machines. The easiest way to reproduce scaling laws is through statistical modelling. Under the assumption that the input parameters are linearly independent, the most commonly used method for estimating the energy confinement time are linear models, such as linear regressions, etc.
But since the plasma parameters used for the scaling law are not truly fully independent, other models were used in addition to the classical linear regression based on an ordinary least squares method, in order to make the prediction more accurate.

Statistical modelling is the use of mathematical models and statistical assumptions to generate sample data and make predictions about the real world. A statistical model is a collection of probability distributions on a set of all possible outcomes of an experiment. Also, performing statistical analysis on the data and the fitting model

are useful to answer questions such as if the model accurately explains the data, which factors in the model is more relevant or if there are parameters that do not contribute significantly to the predictive power of the model.
In principle, for a set of dependent variables Y, and independent variable X, the aim is to find a mathematical relationship or model between Y and X. In general, for a mathematical model as a function $Y = f(X)$, knowing the function $f(X)$, it is possible to compute the value Y for any of values X. If the function $f(X)$ is an unknown, but the data for the observations $\{y_i, x_i\}$ are available, the function $f(X)$ can be parameterized and the values of the parameters can be fitted.
A common example of parametrization is the linear model $f(X) = \beta_0 + \beta_1 X$, where β_0 and β_1 are the parameters of the model. If the data points are more than the number of free parameters a least-square fit that minimizes the norm of the residual $r = Y - f(X)$ could be used. Moreover, the data can be affected by an uncertainty, for example due to the measurement noise. This uncertainty in the data can be described as random variables: $Y = f(X) + \epsilon$. Depending on how the random variables appear in the model and what distributions the random variables follow, different types of statistical models are obtained.
A statistical model is also useful when x_i is a vector with control knobs that are recorded together with each observation. An element in x_i may be relevant or not for predicting the observed outcome y_i. An important aspect of the statistical model is to determine which explanatory variables are relevant. Determining if a model accurately explains the data is another essential aspect of statistical modelling.
Therefore, the typical statistical model is $f(X) = \beta_0 + \beta_1 X + \epsilon$ and it is known as simple linear regression if X is a scalar, multiple linear regression if X is a vector and multivariate linear regression if also Y is a vector. The model can be fitted using an "ordinary least squares" (OLS). In the case of multivariate linear regression and the element in Y independent and normally distributed with equal variance, the method used is known as "generalized least squares" (GLS) and "weighted least squares" (WLS). Anyway, the most important assumption is that the residuals are independent and normally distributed [32].
In the following subsections all the models used in the data analysing are described. For all the methods, the target value is expected to be a linear combination of the independent values. In mathematical notation, if $\hat{y}$ is the predicted value:

$$\hat{y}(w, x) = w_0 - w_1 x_1 + ... + w_p x_p \tag{2.47}$$

where the vector $w = (w_1, ... w_p)$ is known as coefficients and w_0 as interception or constant.

2.5.1 Ordinary least squares method

The "ordinary least squares" is a type of linear least squares method. It chooses the parameters of a linear function of a set of variables minimizing the residual sum of squares between the observed targets in the data and the targets predicted by the

linear approximation. Mathematically it solves a problem of the form [33]

$$m = \frac{\int (x_i - \overline{x})(y_i - \overline{y})}{\int (x_i - \overline{x})^2} \tag{2.48}$$

Where x are the independent variables, y the dependent ones, $\overline{x}$ and $\overline{y}$ are the average of the independent and dependent variables.
Geometrically, it corresponds to the squared distances, parallel to the axis of the dependent variable, between each data point in the set and the corresponding point on the regression surface (figure 2.4). The smaller the distances, the better the model fits the data [34].

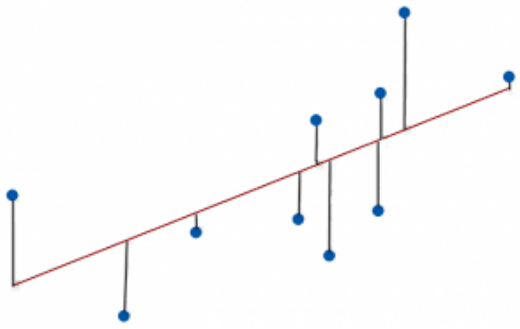

Figure 2.4 – squared distances between each data point in the set and the corresponding point on the regression surface for a ordinary least squares model.

A large data set is necessary in order to obtain reliable results. The regression results are sensitive to functional form if the error term is not adequately interpreted, which can lead to widely varying conclusions depending on how the regression is initially set up. Furthermore, the results are especially sensitive to outliers, since the “best” performer along any dimension serves as the anchor for the estimate. Thus, the performance scores are very sensitive to outliers. [33].

2.5.2 Weighted least squares method

"Weighted least squares method" (WLS) is a generalization of ordinary least squares and linear regression in which the errors covariance matrix is allowed to be different from an identity matrix [35]. In statistics, a covariance matrix is a square matrix giving the covariance between each pair of elements of a given random vector. In the matrix diagonal there are the covariance of each element with itself [36].
In the loss function, the weight to every residual is added as in the formula:

$$loss = \frac{1}{2} \sum_i w_i (\hat{y} - y_i)^2 \tag{2.49}$$

Where y are the dependent variables and $\overline{y}$ are the average of the and dependent variables.
This method is useful when there are imbalances in the data due to different origins of the data or heteroscedascity. To overcome imbalance a weighting factor inversely proportional to the source of the imbalance can be added [37].

2.5.3 Generalized least squares method

The generalized linear model (GLM) is a flexible generalization of ordinary linear regression that allows for response variables that have error distribution models other than a normal distribution. The GLM generalizes linear regression by allowing the linear model to be related to the response variable via a link function and by allowing the magnitude of the variance of each measurement to be a function of its predicted value.
Ordinary linear regression predicts the expected value of a given unknown quantity as a linear combination of a set of observed values. This implies that a constant change in a predictor leads to a constant change in the response variable. This is appropriate when the response variable has a normal distribution. However, these assumptions are inappropriate for some types of response variables. For example, in cases where the response variable is expected to be always positive and varying over a wide range, constant input changes lead to geometrically varying, rather than constantly varying, output changes.
In a generalized linear model (GLM), the mean, μ, of the distribution depends on the independent variables, X, through:

$$E(Y) = \mu = g^{-1}(X\beta) \tag{2.50}$$

where $E(Y)$ is the expected value of Y, $X\beta$ is the linear predictor and g is the link function. The GLM consists of three elements [38]:

— An exponential family of probability distributions;

— A linear predictor $\eta = X\beta$;

— A link function g such that $E(Y|X) = \mu = g^{-1}(\eta)$

This model is also useful to fit the model subject to linear equality constraints. The estimation creates a new model with transformed design matrix and converts the results back to the original parameterization [39].
This method is therefore very useful for calculating the dimensional coefficients of the scaling law for WEST in order to directly include the Kadomtsev constraint in the model itself. The calculated coefficients, therefore, are computed to satisfy the following equation:

$$5\alpha_B - 4\alpha_R + \alpha_I + 3\alpha_P + 8\alpha_n = -5 \tag{2.51}$$

2.5.4 Feature selection

This method can be used for feature selection/dimensionality reduction on sample sets, either to improve estimators accuracy scores or to boost their performance on very high-dimensional datasets.
Given an external estimator that assigns weights to features, the recursive features elimination (RFE) selects features by recursively considering smaller and smaller sets of features. First, the estimator is trained on the initial set of features and the importance of each feature is obtained either through a coefficient attribute or through a feature importances attribute. Then, the least important features are pruned from current set of features. That procedure is recursively repeated on the pruned set until the desired number of features to select is eventually reached [33].

All these statistical techniques were used throughout the first part of the PhD work. They were used to analyse the WEST database and to compare it with the existing scaling laws proposed to predict energy confinement time. The first analyses were done with a classical ordinary least square method, this was then implemented with weighted least square method to take into account the weight that each tokamak has on the scaling law that depends on the total number of discharges for each tokamak in the database. Furthermore, a second improvement was inroduced with GLM, which allows the regression coefficients to be calculated taking the kadomtsev constraint into account a priori.
The results of this first part of the work are presented in the next chapter.

2.6 Transport in plasma

Confinement is limited by thermal and particle losses and radiation.

The one of the mechanism of transport is the Coulomb collisions, which affect the charged particles gyromotion around the field lines. If two field lines are close enough, the particles of each line can interact through the coulombian repulsion and create a random diffusive process by making these particles moving from a field line to another. This is the classical transport. Its diffusion coefficient can be expressed by:

$$D_{classical} = r_L^2 \nu \tag{2.52}$$

Where $r_L = m v_\perp / (qB)$ is the Larmor radius and it represents the displacement of a particle after a collision, and ν is the collision frequency proportional to $nT_e^{-3/2}$ for

electrons. For a typical Deuterium discharge, this diffusive coefficient is of the order of $10^{-4}/10^{-2} m^2 s^{-1}$.

One must also take into account that, tokamak plasmas being toroidal devices, the radial variation of magnetic field induces other diffusion processes responsible of transverse transport. However, anomalous or turbulent transport, caused by instabilities in the plasma, is the main contributor to the total particle, heat and momentum transport [40] [41].

Predicting how the system evolves is of fundamental importance, which is why it is necessary to code the system through a series of equations that take into account all possible types of transport in the plasma.
In general, in the plasma core, particle, heat and momentum follow the local transport equation. The transport equation for particles and heat are [42]:

$$\frac{\partial n}{\partial t} + \vec{\nabla}\cdot\vec{\Gamma} = S \tag{2.53}$$

$$\frac{3nk_B}{2}\frac{\partial T}{\partial t} + \vec{\nabla}\cdot\vec{q} = W \tag{2.54}$$

where n is the particle density, Γ the particle flux in $[m^{-2}s^{-1}]$, S is the particle source in $[m^{-3}s^{-1}]$, T is the temperature, q the heat flux in $[Wm^{-2}]$ and W the heat source in $[Wm^{-3}]$.

In absence of particle source and in steady-state, and assuming that the transport can be modelled by diffusion plus convection mechanisms, it is possible to rewrite the equation 2.53 as:

$$\Gamma = -D\nabla\cdot n + Vn \tag{2.55}$$

$$D = D_{turb} + D_{neo} \tag{2.56}$$

$$V = V_{turb} + V_{neo} \tag{2.57}$$

where D and V are the diffusion and convection coefficients.
Therefore it has been assumed that the neoclassical and turbulent transports are simply additive.

2.6.1 Neoclassical transport

Neoclassical transport describes the collisional transport. It provides a model for the transport of particles, momentum, and heat due to Coulomb collisions in confined plasmas in complex magnetic geometries, assuming that the plasma is in a quiescent state [43].

The theory starts from the Kinetic Equation for the mean particle distribution function $f_\alpha(x, v, t)$:

$$\frac{\partial f}{\partial t} + \boldsymbol{v} \cdot \frac{\partial f}{\partial \boldsymbol{x}} + \frac{e_j}{m_j}(\boldsymbol{E} + \boldsymbol{v} \times \boldsymbol{B}) \cdot \frac{\partial f}{\partial \boldsymbol{v}} = (\frac{\partial f}{\partial t})_c \tag{2.58}$$

where is the velocity, E is the electric field, B the magnetic field and the term on the right-hand side is the collision operator. Once the collision operator is derived, the moments of the Kinetic Equation can be computed.
The theory takes into account all particle motion associated with toroidal geometry, specifically, ∇B (in a magnetic field with a transversal gradient the particle orbit has a smaller radius of curvature on the part of its orbit in the stronger magnetic field and this leads to a drift perpendicular to both the magnetic field and its gradient) and curvature drifts (when a particle's guiding centre follows a curved magnetic field line it undergoes a drift perpendicular to the plane in which the curvature lies), hence passing and trapped particles (particles in the outer side of the torus, having a small velocity parallel to the magnetic field undergo a magnetic mirror reflection as they move into the region in higher field. In the absence of collisions the particles are trapped in the low field region.). The theory is valid for all collisionality regimes. An important prediction of the theory is the bootstrap current [44].
The neoclassical theory has a range of limitations due to a fixed geometry, the linearity of the model and the locality.

The dominant role of neoclassical transport for high-Z impurities has been already recognized in several previous studies, in conditions of good energy confinement, and both in the core and in the pedestal of H-modes, where turbulent transport is largely suppressed. Tungsten with high Z is more sensitive than D to coulombian collisions, In particular the importance of the neoclassical transport for tungsten in H-mode plasmas and in hybrid scenarios has been deeply analysed [45]. However, as will be explained in the following, neoclassical transport can also be responsible for the central accumulation of tungsten in L-mode tokamaks.

There are several neoclassical codes, at different levels of complexity. An example is NEO [46] that solves the full drift kinetic equation, providing a first-principle calculation of the transport coefficients directly from the kinetic solution of the distribution function. It uses the full linearized Fokker Planck collision operator [47]. The full drift kinetic equation is a form of the Fokker-Planck equation which describes the evolution of f under conditions where it occurs slowly in time compared to the gyro-period and gradually in space compared to the gyro-radius of the particle orbits. The Fokker-Planck equation describes the dominant effect of collisions in a plasma that occurs through the cumulative contribution of many small angle scattering. NEO accounts for the effect of poloidal asymmetries on W distribution. Theoretical works have pointed out that the neoclassical transport of heavy impurities can be strongly

modified in the presence of poloidal asymmetries of the impurity density. This implies that the strong localization of impurities has two unfavorable consequences, the strong increase of the neoclassical transport and the reduction of the relative weight of the temperature screening. Therefore, the poloidal asymmetries reduces the strength of temperature screening inducing the presence of low field side localization of the tungsten density. NEO needs about 12 CPU hours for 1s of plasma on 16 processors.

2.6.2 Turbulent transport

Turbulent transport of particles, heat and momentum results from fluctuations induced by instabilities at the microscopic scale. In tokamak plasmas, instabilities can develop due to the presence of finite gradients of the plasma temperature and density [48]. The presence of plasma microinstabilities leads to a turbulent state that in tokamaks produces the largest part of the radial cross-field transport of energy, particles, and momentum.
This main contributor dominates the transport in the core plasma as well as in the edge. It represents one of the most important issues in tokamak physics because of its large impact on the degradation of the confinement time. In fact, as shown in section on confinement time, τ_E has a negative strong correlation respect to the total power. Therefore, more power means steeper gradients, hence more turbulence.

The description of turbulent transport determining the plasma profiles is highly non-trivial due to the nonlinear dependence of the amplitude of radial diffusion on the plasma equilibrium quantities and the magnetic geometry. Also, the properties of turbulent transport can change significantly from the core to the edge of the plasma, and from H-mode to L-mode, due to strong changes in the plasma parameters [49] [50].

In order to understand and predict turbulent transport in current and future experiments, several computational tools have been developed over time, with various degrees of accuracy and therefore various computational requirements. Different turbulent transport codes are GYSELA [51] (a non-linear 5D gyrokinetic code), ORB5 [52], GENE [53], GYRO [54] (non-linear gyrokinetic codes), GKW [55], QuaLiKiz [56] [57] [58] [59], TGLF [60] (gyrokinetic quasi-linear approach) and the Bohm-GyroBohm model [61] (very fast semi-empirical model based on scaling laws and coefficients empirically tuned on experimental measurements).
Both neoclassical and turbulent transport are important to predict particle sources as well, they are needed for the integrated modelling.

2.7 Integrated modelling

The use of an integrated modeling tool is mandatory in order to evolve many plasma quantities at the same time until steady-state is reached.
Each plasma parameter, or module, is evolved by a specific code. Several codes are available per plasma parameter, so the user can choose the level of complexity needed for each module depending on the purpose of his/her study.
An integrated modeling tool can be run in two different modes:

— Interpretive mode, the plasma profiles are not evolved by a code, but read from experimental fits. The outputs of such a simulation are the heat, particle and momentum transport coefficients;

— Predictive mode, the density, temperature and rotation measurements are used as initial and boundary conditions. The transport modules predict the fluxes and the outputs of such a simulation are the predicted density, temperature and rotation profiles.

Different integrated modelling platforms are currently used is fusion research.
The code ASTRA (Automated System for TRansport Analysis) is developed in IPP Garching, in Germany. It solves a user-defined set of transport equations in toroidal geometry. ASTRA includes an extended library of physical modules, a graphic interface, plotting and post-run viewing facilities [62].
CRONOS was developed at CEA in France since 1999 and has been used to analyze data from several tokamaks including Tore Supra, JET and ASDEX Upgrade [63].
JINTRAC is developed at CCFE, in the United Kingdom. It is a system of 25 interfaced Tokamak-physics codes for the integrated simulation of all phases of a Tokamak scenario. JINTRAC predictions reflect the physics and assumptions implemented in each module and extensive comparison with experimental data is needed to allow validation of the models and improvement of Tokamak-physics understanding. If the modeling focuses on the plasma core, the integrated modeling platform is called JETTO. It also includes first-principle based turbulent and neoclassical transport codes [64].
RAPTOR (RApid Plasma Transport Simulator) was first developed within F. Felici's EPFL PhD thesis work. It is a 1D tokamak transport code specially designed for rapid execution compatible with needs for real-time execution or for use in nonlinear optimization schemes [65].

2.8 WEST tokamak

WEST [66] [67] (tungsten environment in steady state tokamak) is a metallic machine built starting from the superconducting Tore Supra tokamak and designed for

operating in lower single null (LSN, X-point in the bottom part of the plasma), upper single null (USN X-point in the upper part of the plasma) and double single null (DSN two X-points in the bottom and in the upper part of the plasma) configuration. The major upgrade consisted in covering the inner wall with bulk or coated tungsten tiles. The main purpose consists of operating in a metallic environment with a high heat flux ($10 MW/m^2$) on the divertor targets during long pulses (1000s). It is targeted at supporting ITER divertor construction and operation thanks to the tungsten mono-blocks PFUs designed for its divertor. the WEST key missions are:

— Paving the way towards the ITER actively cooled tungsten divertor;

— Mastering integrated plasma scenarios over relevant plasma wall equilibrium time scale in a metallic environment.

The main WEST specifications are summarized in the table 2.3:

WEST parameters	
$I_p(q_{95})$	$1MA$
$B_T(R = 2.5cm)$	$3.5T$
$n_{GW}(1MA)$	$1.5 \cdot 10^{20} m^{-3}$
R	$2.5m$
a	$0.5m$
A	$\sim 5-6$
k	1.35
δ	0.5
Plasma volume	$15m^3$
ICRH heating power	$9MW$
LHCD heating power	$7MW$
flat-top duration	up to $1000s$

Table 2.3 – WEST specifications

As it is possible to notice from the table 2.3, WEST is dominantly electron heated and no torque is applied.
WEST allows flexible magnetic configurations from lower (far and close X-point configurations) and upper single null to double null. It includes 18 NbTi superconducting toroidal field coils cooled by super-fluid helium at 1.8K (figure 2.5a) and 6 conventional copper poloidal field coils water cooled (figure 2.5b) plus two divertor coils and a central solenoid. The toroidal filed is directed clockwise, view from top, and the $B \times \nabla B$ drift is directed downwards. The divertor in-vessel coils are water cooled copper coils.

The main plasma facing components (PFCs) include (figure 2.6):

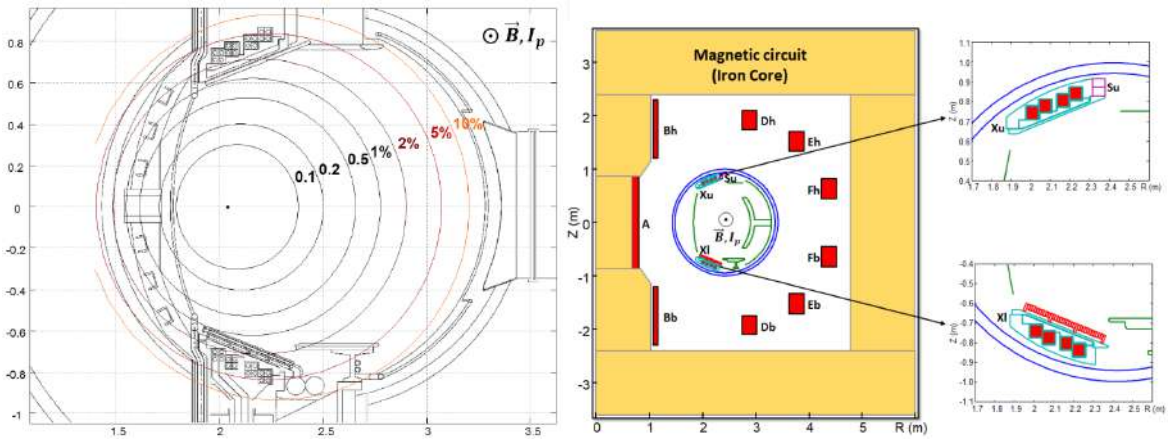

(a) Toroidal field coils induced magnetic ripple. (b) Poloidal field coils. A, Bb and Bh are the central solenoid, Dh, Eh, Fh, Db, Eb, Fb are the poloidal coils and Xu, Su and XI are the divertor coils.

Figure 2.5 – WEST magnetic configuration

— The lower divertor target, where the ITER divertor technology is tested [68];

— The upper divertor target, allowing upper single null operation [69];

— The baffle, channeling neutrals towards the pumping systems in the lower vertical ports [70];

— A set of inner bumpers and a movable outer limiter, protecting the vessel [71];

— The ripple (the finite number of toroidal field coils destroy the perfect axisymmetry of the device producing a short wavelenght 'ripple' in which the particles could be trapped)/Vertical Displacement Events (VDE) protections, located on upper vertical port [69];

— The antennas protections [69];

The lower divertor is based on the ITER technology (tungsten mono-blocks), while the remaining plasma facing components use tungsten coatings. The remaining vessel is protected by water cooled stainless steel panels.

The additional heating and current drive are provided by radiofrequency (RF) waves, in particular the Ion Cyclotron Resonance Heating (ICRH) and the Lower Hybrid Current Drive (LHCD) are available.
The first one has been designed to deliver 9MW for 30s, 6MW for 60s and 3MW for up to 1000s from three identical antennas respectively in horizontal ports in torus

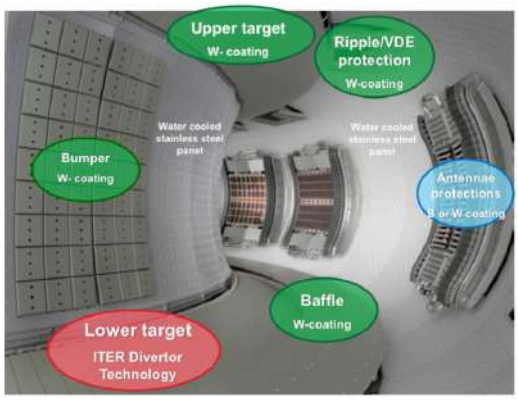

Figure 2.6 – Plasma facing components

quadrants Q1, Q2 and Q4. The nominal operating frequency is 55.5±2MHz. All the antennas can be moved radially between the discharges. Each of them is composed of four straps inside a box and behind a Faraday screen. Moreover, on each side, CFC limiters coated with 100μm layer of tungsten protect the antenna front face from the plasma. [72]
The LHCD system is composed of two antennas powering respectively 4MW of the Full Active Multijection (FAM) launcher and 3MW for the Passive Active Multijunction (PAM) launcher. Each antenna is equipped with two limiters in carbon with a tungsten coating and with a local gas injection (2.5×10^{21} el/s per launcher) [73].

One of the two major characteristics of WEST is that it has a full tungsten environment. W has an atomic mass A=184 and a charge Z=74. Even for ITER core temperatures, W does not get fully ionized. W radiation depends on W and electron densities, and on a cooling factor which depends on the electron temperature and the W charge state [74]. When W concentration exceeds a certain amount in the plasma core, typically around 2×10^{-4} radiative losses balance the heating supply, which can lead to a radiative collapse.
This phenomena is also observed in JET during current ramp up [75] even at high power discharges and even during DT experiment [76], in FTU [77] and in AUG [78].
W transport is a combination of neoclassical and turbulent components. The neoclassical contribution dominates on the inner half, while turbulent component dominates the outer half.

The other WEST characteristic is its aspect ratio. Compared to all other tokamaks, WEST has an aspect ratio of about 5-6 where JET, and AUG are almost 3.

Both of these characteristics affect the energy confinement time. That is why it is important to analyse their impact on WEST plasma performance.

3 Confinement time scaling laws

In this chapter confinement time scaling laws are proposed based on multi-machine databases including WEST L-mode.
First of all, the ITER89-P and the ITER96-L scaling laws are reproduced and compared to each other in order to understand their differences [20].
WEST L-mode database is compared to the existing multi-machine one. The impact of the aspect ratio is discussed.
Finally, the WEST energy confinement is analysed alone, in order to isolate the differences with respect to ITER89-P and ITER96-L.

3.1 Multi-machine L-mode confinement time analysis

The first step of the analysis consists in reproducing the ITER89-P and ITER96-L scaling laws starting from the version 3.2 of the ITPA L-mode database [20].
The difference between the two scaling laws consists in the definition of the confinement time τ. For the ITER89-P scaling the energy confinement time is defined as:

$$\tau_E = \frac{W_{tot}}{P_L} \tag{3.1}$$

where W_{tot} is the total plasma energy and P_L is the estimated total heating power corrected for $\frac{dW}{dt}$ but not for change exchange, unconfined orbit losses and radiated power. The number of entries is 1798.
While, for the ITER96-L scaling the energy confinement time is defined as:

$$\tau_{th} = \frac{W_{th}}{P_{LTH}} \tag{3.2}$$

where W_{th} is the estimated thermal plasma energy and P_{LTH} is the estimated total heating power corrected for $\frac{dW}{dt}$ and for change exchange and unconfined orbit losses, but not for radiated power. The number of entries is 1312.
The range covered by the plasma current, the magnetic field, the elongation, the major radius, the aspect ratio (A), the line averaged electron density, the effective mass and

the total power are the same for the two databases except for the total power and the lower limit of the line-average electron density. The range are reported in the table 3.1. To highlight the difference between the two databases, the numbers of entries per tokamaks are shown in table 3.2. The main difference comes from JT-60 and DIIID tokamaks.

	$I_P[MA]$	$B_T[T]$	k	$R[m]$	A	$n_e[10^{19}m^{-3}]$	$M_{eff}[AMU]$	$P_{tot}[MW]$
min	0.12	0.61	0.95	0.66	2.41	0.73 (1 ITER96)	1	0.31 (0.25 ITER96)
max	5.01	5.27	2.08	3.18	7.78	18.52	2.5	26.65 (20.70 ITER96)

Table 3.1 – Range of the variables for ITER89-P and ITER96-L database

Tokamak	**ITER89-P**	**ITER96-L**
CMOD	55	55
ASDEX	73	73
DIII	210	0
DIII-D	147	129
FTU	0	0
JET	320	325
JFT2M	125	129
JT60	410	174
PBXM	30	30
PDX	28	40
T10	20	20
TEXTOR	82	82
TFTR	143	188
TSUPRA	68	68
Total	1798	1312

Table 3.2 – Entries per tokamaks for the ITER89-P and ITER96-L databases

Then, the common linear regression is applied to the database obtained by filtering the version 3.2 of the ITPA L-mode database considering the assumptions in Ref. [20]. The scaling is made with respect to τ_E and to τ_{th} to compare with the reference value of the scaling reported in Ref. [20]. In table 3.3 the coefficients of ITER89-P, ITER96-L and the ones computed from the linear regression are reported.

Variable	ITER89-P	Reproduction	ITER96-L	Reproduction
Constant	0.037	0.037	0.023	0.024
I_P	0.74	0.75	0.96	0.98
B_T	0.20	0.18	0.03	0.04
K	0.67	0.67	0.64	0.63
R	1.69	1.69	1.83	1.78
A	-0.31	-0.31	0.06	0.06
n_e	0.24	0.23	0.40	0.40
M_{eff}	0.26	0.26	0.40	0.40
P_{tot}	-0.57	-0.57	-0.73	-0.73
Entries	1798	1791	1312	1313
RMSE	16%	16.6%	15.8%	15.8%
R^2	0.98	0.98	0.97	0.97

Table 3.3 – ITER89P and ITER96P dimensional scaling reproduction

The coefficients, the RMSE and the R^2 of the fitting are very close to the reference values.

To check if the scalings are physically correct, the Kadomtsev transformations [27] are applied to shift from the dimensional to dimensionless scaling coefficients. The scalings are consistent only if the Kadomtsev constrain is respected ($\chi_B = 0$ [27]). For ITER89-P the scaling exponent of major radius has been slightly modified from 1.69 to 1.74 to satisfy the Kadomtsev constraint, this is an arbitrary choice that has been justify in ref. [28]. The results are reported in table 3.4 and the results are very close to the reference values.

Variable	ITER89-P	Reproduction	ITER96-L	Reproduction
q	-1.59	-1.62	-3.74	-3.74
B_T	0	0	0	0
K	1.95	1.98	3.22	3.26
A	0.25	0.18	0.04	0.05
M_{eff}	0.57	0.52	0.67	0.74
ρ_*	-1.93	-1.82	-1.85	-1.99
ν_*	-0.13	-0.13	0.19	0.16
β	-0.63	-0.64	-1.41	-1.39
Entries	1798	1791	1312	1313
RMSE	16%	16.6%	15.8%	15.8%
R^2	0.98	0.98	0.97	0.97

Table 3.4 – ITER89P and ITER96P dimensionless scaling reproduction

The difference in aspect ratio coefficient for ITER89-P and its reproduction is not so week, this is due to the fact that the major radius coefficient has been modified. In fact, if we modify the R coefficient also for the case of the reproduction scaling, the coefficient for the aspect ratio matches 0.25.
Since the main difference between the two scalings deals with the aspect ratio coefficient, this parameter has been more deeply analysed. First of all, the histogram for the aspect ratio of the two databases is plotted (figure 3.1a). This difference is due to JT-60. As seen in the figure 3.1b, the discharges of JT-60 cover a very large range of aspect ratio. The highest A are in single null configuration (SN). In fact, if these pulses are removed in ITER89-P database, the aspect ratio coefficient is close to ITER96 (table 3.5). They correspond to the discharges for which τ_{th} is not available. The pulses with this configuration are characterized by a small plasma volume (figure 3.1c), probably, it is responsible of the energy confinement time degradation. In fact, JT60 was made for the outboard midplane single null (SNO) but they tried to do the lower single null without dedicated coils, which lead to a smaller plasma volume and larger A.

Variable	**ITER89-P**	**ITER96-L**	**ITER89-P without JT60 SN**
A	0.25	0.04	0.03
Entries	1791	1313	1512
Entries for JT-60	424	174	145

Table 3.5 – ITER89P without JT-60 shots in SN configuration

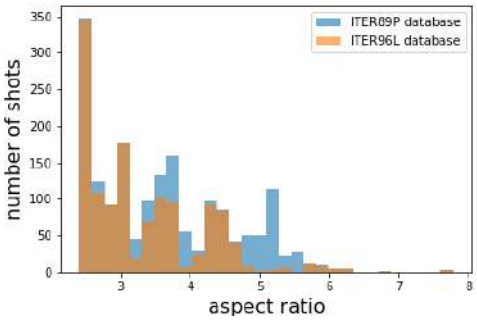

(a) Comparison between aspect ratio range covered by ITER89-P and ITER-L databases

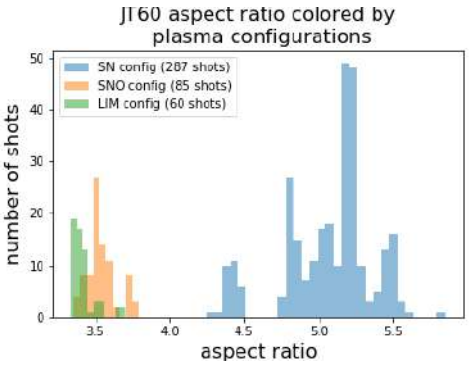

(b) JT-60 aspect ratio colored by configurations

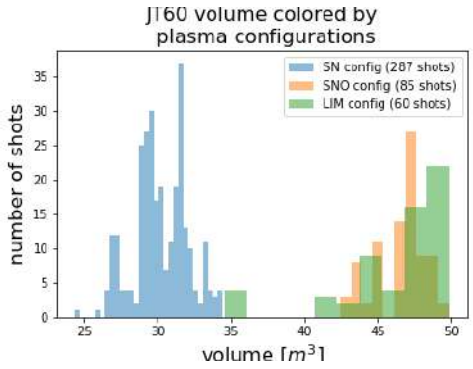

(c) JT-60 plasma volume colored by configurations

Figure 3.1 – Aspect ratio analysis in ITER98P and ITER96L databases.

3.2 WEST confinement time analysis

3.2.1 How the database is constructed

The WEST database is built starting from the outputs of about 50 diagnostics measurements like bolometers, visible light spectroscopy, etc. Then the data are treated using IMAS workflow [79] as shown in the following figure 3.2.

The database is based on plateau phases and it contains the mean values and the standard deviations of different diagnostic measurements on each plateau (quasi-steady-state). The plateaus are identified intersecting the total power plateaus and the plasma current plateaus. The minimum flattop time duration can be set manually, in the performed studies it is set to 0.3s. The database is constructed starting from the data collected during the C3 and C4 campaigns (2018-2019, 2924 pulses and 3775 plateaus).

Figure 3.3 shows an example of how the quasi-steady states are identified. The blue line is the signal of plasma energy content $W_{mdh,polarimetry}$ provided by polarimetry constrained equilibrium reconstructions for pulse 55539 using the NICE code [80].

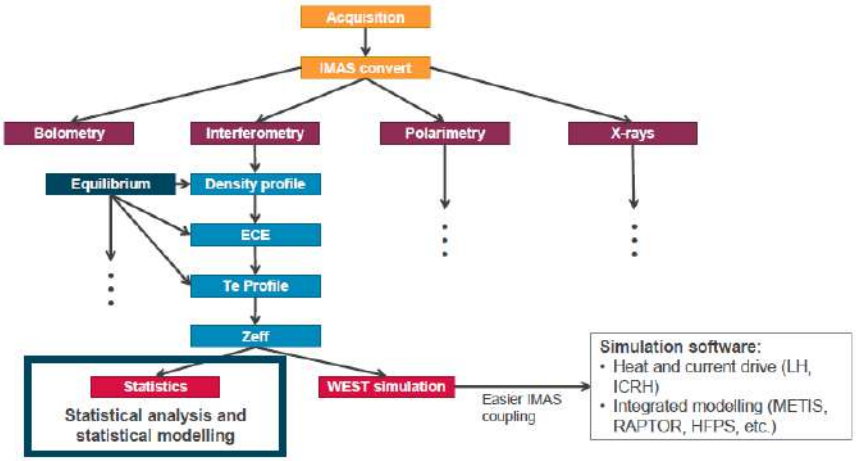

Figure 3.2 – WEST IMAS Data Processing Workflow.

The dashed lines mark the time intervals in which the plateaus are identified. The yellow, green and red horizontal lines are the averaged values of the signal stored in the database.

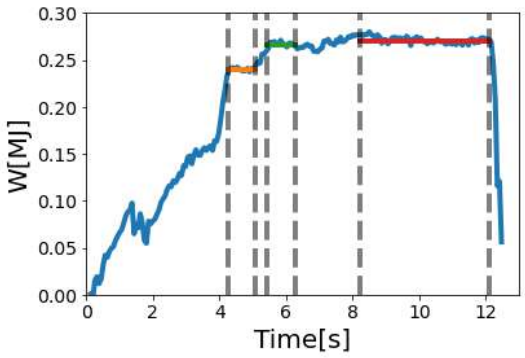

Figure 3.3 – The blue line is the energy content signal during pulse 55539 computed by NICE. The vertical dashed lines mark the initial and final times of the identified plateaus. The yellow, green and red horizontal lines are the averaged values of the signal on the identified plateaus stored in the database.

The energy confinement time is computed as:

$$\tau_{mhd} = \frac{W_{mhd,polarimetry}}{P_{tot} - \frac{dW_{mhd,polarimetry}}{dt}} = \frac{\frac{3}{2}\int_V P dV}{P_{ohmic} + P_{aux} - \frac{dW_{mhd,polarimetry}}{dt}} \tag{3.3}$$

Where P is the total plasma pressure, P_{aux} is the auxiliary power, P_{ohmic} is the ohmic power and P_{tot} is the total power.

Since WEST plateaus include ohmic pulses as well as helium discharges, the database is filtered applying the following criteria:

— The ohmic pulses are excluded imposing a $P_{aux} > 0.5MW$ (1740 pulses filtered out);

— Only the deuterium pulses are kept and helium discharges are excluded;

— Only pulses that have equilibrium reconstructions with low errors with respect to interferometry line integrated density measurements are considered, maximum authorized relative error of reconstructed line integrated density is fixed to 20% (208 pulses filtered out);

— Lower single null configuration plasmas are selected (142 pulses filtered out);

With these restrictions, the present WEST database contains 1083 entries.

A few histograms of the database are reported in figure 3.4. The majority of the plateaus are at plasma current of 0.5MA with a few discharges at 0.3MA, 0.4MA and 0.7MA (figure 3.4a). The line averaged electron density is in the range of $1-7\cdot10^{19}m^{-3}$ (figure 3.4b). The height of the X point is in the range of 0.04m to 0.12m (figure 3.4c). The total power is in the range 0.5MW to 8MW with P_{ICRH} in the range of 0-3MW and P_{LH} in the range of 0-5MW (figures 3.4d, 3.4f and 3.4e). The fraction of the radiated power in the bulk is on averaged about 50% 3.4g.

3.2.2 Exploring WEST confinement time

The aim of the work is to check if WEST L-mode confinement is well aligned with the other tokamaks and to investigate the aspect ratio effect on L mode confinement. It has been observed that if the aspect ratio changes, the fraction of trapped particles also changes. In particular, larger aspect ratio leads to less trapped particle, hence less drive for TEM. Inversely, lower aspect ratio leads to more trapped particles but also for passing particles spending more time on the good curvature side [81]. It is also important to remind that more trapped particles leads to more bootstrap current, which is good for steady state operation, more non-inductive current. Moreover, lower A tokamaks allow to reach higher beta that impacts the turbulent transport greatly. [82]
WEST is well suited for this analysis because it is characterized by an aspect ratio large compared to other tokamaks.

The only available value for the energy confinement time in WEST is τ_{mhd}. Therefore, a subset of the ITPA L-mode database is selected such that τ_{mhd} is available and taking into account that the difference between τ_{mhd}, τ_E and τ_{th} dose not exceed 30%. The entries for which τ_E, τ_{th} and τ_{mhd} stand in the range of 30% numbered to 795

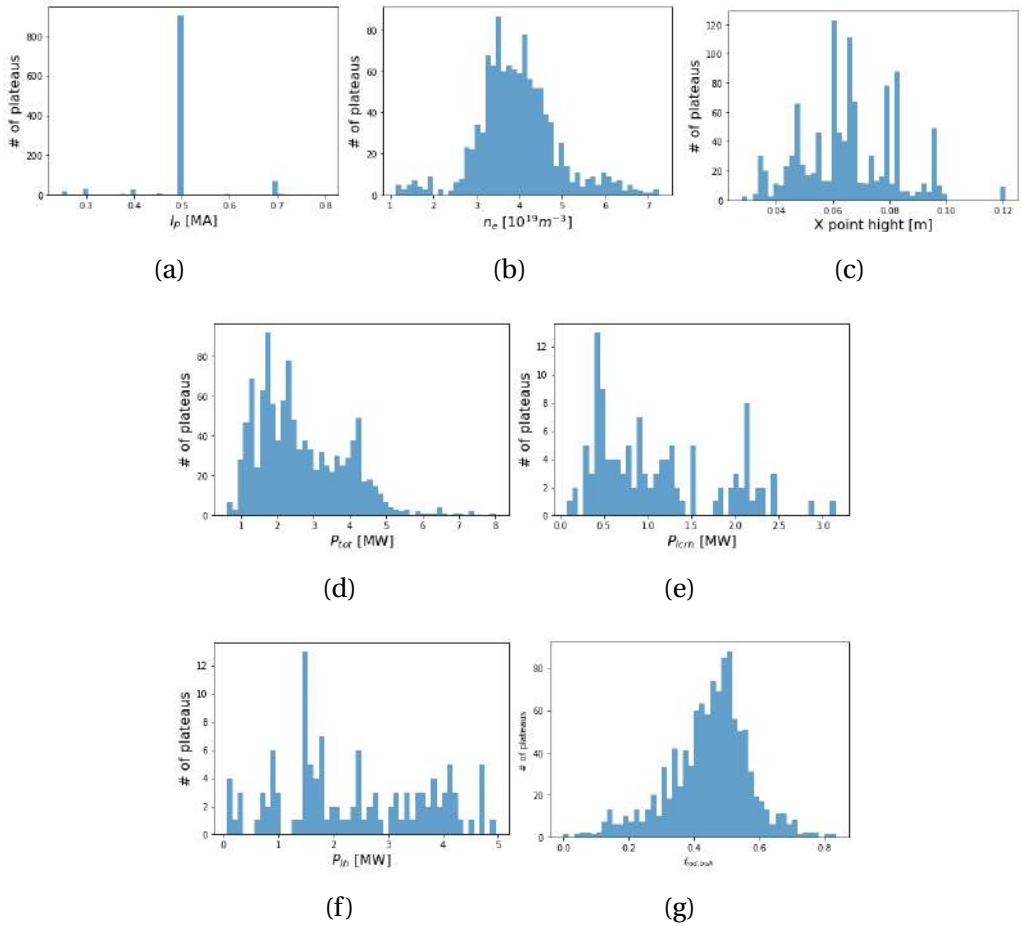

(a) (b) (c)

(d) (e)

(f) (g)

Figure 3.4 – Histogram of plasma current (a), line averaged electron density (b), X point height (c), total power (d), ICRH power injection (e), LHCD power injection (f) and the fraction of the radiated power in the bulk.

and this new subset of L-mode database will be called W_{mhd} database. The number of pulses for each tokamak in the three databases (ITER89-P, ITER96-L and W_{mhd}) are shown in table 3.6. Some tokamaks did not provide τ_{mhd} such as DIIID, JT60. While other tokamaks had more pulses with τ_{mhd} than τ_E and τ_{th}. This could impact the scaling.
The histogram of the aspect ratio range is plotted in figure 3.5.

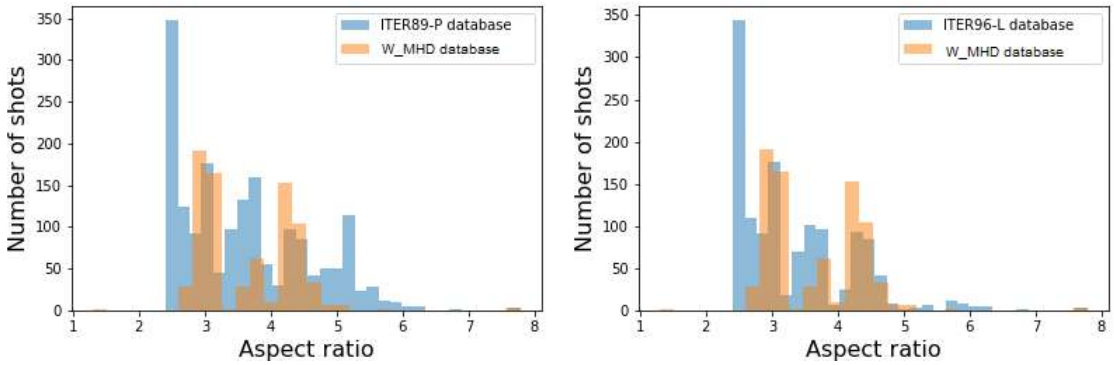

(a) Aspect ratio histogram comparing W_{mhd} and ITER98-P database.

(b) Aspect ratio histogram comparing W_{mhd} and ITER96-L database

Figure 3.5 – W_{mhd}, ITER89-P and ITER96-L aspect ratio histogram

Tokamak	**ITER89-P**	**ITER96-L**	W_{mhd}
	τ_E	τ_{th}	τ_{mhd}
CMOD	55	55	140
ASDEX	73	73	194
DIII	210	0	0
DIIID	147	129	0
FTU	0	0	0
JET	320	325	0
JFT2M	125	129	101
JT60	410	174	0
PBXM	30	30	0
PDX	28	40	29
T10	20	20	4
TEXTOR	82	82	61
TFTR	143	188	264
TSUPRA	68	68	0
NSTX	0	0	2
Total	1798	1312	795

Table 3.6 – Shots for each tokamak of W_{mhd}, ITER89-P and ITER96-L database

To assess the impact of the modified number of entries and the different weight of each tokamak, the W_{mhd} database has been used with τ_E and τ_{th} and compared to ITER89-P and ITER96-L respectively. The results are summarized in the table 3.7 for the dimensionless scaling laws and table 3.8 for the dimensional ones. The method used to switch from engineering to dimensionless coefficients is explained in section 1.4.

Variable	W_{mhd}	**ITER89-P**	W_{mhd}	**ITER96-L**
	τ_E	τ_E	τ_{th}	τ_{th}
q	-1.85	-1.59	-2.34	-3.74
B_T	0	0	0	0
K	1.63	1.95	1.86	3.22
A	0.01	0.25	-0.03	0.04
M_{eff}	0.38	0.57	0.60	0.67
ρ_*	-1.58	-1.93	-1.54	-1.85
ν_*	-0.15	-0.13	-0.02	0.19
β	-0.68	-0.63	-0.87	-1.41
Entries	795	1791	795	1313
RMSE	13.8%	16.6%	14.5%	15.8%
R^2	0.98	0.98	0.97	0.97

Table 3.7 – Comparison of W_{mhd} database dimensionless scaling laws with ITER89-P and ITER96-L dimensionless scaling laws.

Variable	W_{mhd}	**ITER89-P**	W_{mhd}	**ITER96-L**
	τ_E	τ_E	τ_{th}	τ_{th}
$constant$	0.04	0.037	0.04	0.023
I_p	0.92	0.75	0.90	0.96
B_T	-0.03	0.18	-0.03	0.03
K	0.34	0.67	0.42	0.64
A	-0.06	-0.31	-0.05	0.06
M_{eff}	0.27	0.26	0.32	0.20
R	1.36	1.69	1.51	1.83
n_e	0.16	0.23	0.27	0.40
P_{tot}	-0.54	-0.57	-0.61	-0.73
Entries	795	1791	795	1313
RMSE	13.8%	16.6%	14.5%	15.8%
R^2	0.98	0.98	0.97	0.97

Table 3.8 – Comparison of W_{mhd} database dimensional scaling laws with ITER89-P and ITER96-L dimensional scaling laws.

There are some important differences between the W_{mhd} database and the ITPA database scalings. The problem comes from the uncertainty in the transformation, in fact, the exponents of the dimensionless parameters in the scaling laws change significantly with the transformation because of the dependence of the dimensionless variables on the dimensional parameters used in the regression [26]. However, using

the Kadomtsev transformation [27], the big problem seems to be the $(1+\alpha_{P_{tot}})$ term appearing as denominator in each coefficients transformation formula (as it is possible to see in section 1.4 formula from 1.38 to 1.44). Therefore, as $\alpha_{P_{tot}}$ is close to -1 a weak variation leads to a large change in the dimensionless coefficients because we are dividing by a small number. Also, the number of entries and the tokamaks in the database play a role in the analysis.

The aim is to find a subset of the database that is coherent and consistent with the L-mode database despite the fact that the linear regression is done with respect to τ_{mhd}. Therefore, considering the W_{mhd} database we perform also a regression taking into account τ_E and τ_{th} (tables 3.7 and 3.8), the scaling with respect to τ_{mhd} is also made (table 3.9 for dimensionless and table 3.10 for engineering parameters). From these tables we observe that the discrepancies between W_{mhd} database and the L-mode scalings are larger if we look at the dimensionless rather than at the dimensional coefficients. This is explained by the small $(1+\alpha_{P_{tot}})$ term at the denominator of the transformation formulas. Now, if we take only W_{mhd} database and perform regressions considering τ_E, τ_{th} and τ_{mhd}, we observe that exponents are relatively close for dimensional (table 3.9) and dimensionless scalings (table 3.10). In addition, we notice that the aspect ratio effect is weak in the majority of cases.

Variable	W_{mhd}	W_{mhd}	W_{mhd}
	τ_E	τ_{th}	τ_{mhd}
q	-1.85	-2.34	-2.19
B_T	0	0	0
k	1.63	1.86	1.71
A	0.01	-0.03	-0.04
M_{eff}	0.38	0.60	0.16
ρ_*	-1.58	-1.54	-1.41
ν_*	-0.15	-0.02	-0.08
β	-0.68	-0.87	-0.83
Entries	795	795	795
RMSE	13.8%	14.5%	15.9%
R^2	0.94	0.94	0.95

Table 3.9 – Comparison of dimensionless coefficients obtained scaling W_{mhd} database respect to τ_E, τ_{th} and τ_{mhd}.

From figure 3.6a, it can be noticed that τ_{mhd}, τ_{th} and τ_E values are not exactly matching and, therefore, the coefficients of the three scalings are not precisely the same even if they are very close to each other.
From this section, it can be robustly concluded that the aspect ratio has a negligible impact on the energy confinement time. In figure 3.6b the τ_{mhd} of the W_{mhd} database

Variable	W_{mhd}	W_{mhd}	W_{mhd}
	τ_E	τ_{th}	τ_{mhd}
$constant$	0.04	0.04	0.04
I_p	0.92	0.90	0.95
B_T	-0.03	-0.03	-0.08
k	0.34	0.42	0.35
A	-0.06	-0.05	0.06
M_{eff}	0.27	0.32	0.19
R	1.36	1.51	1.35
n_e	0.16	0.27	0.20
P_{tot}	-0.54	-0.61	-0.58
Entries	795	795	795
RMSE	13.8%	14.5%	15.9%
R^2	0.94	0.94	0.95

Table 3.10 – Comparison of engineering coefficients obtained scaling W_{mhd} database respect to τ_E, τ_{th} and τ_{mhd}.

has been plotted as a function of the aspect ratio and it is colored depending on the tokamak. The same energy confinement time can be obtained using different aspect ratio values and also a large range of energy confinement time can be obtained using the same value of aspect ratio, the overall data dispersion is large. However, it must be remembered that the energy confinement time depends on many factors. A possible future analysis could look at all discharges with similar characteristics except for the aspect factor, to better see the impact on the confinement time to validate this last statement.

3.2.3 Exploring diverted configurations in deuterium plasmas

The W_{mhd} database still has hydrogen and limiter configuration discharges.
To better understand the effect of the plasma configuration on the energy confinement time, only the single null (SN), the lower single null (LSN) and the double null (DN) configuration are selected in the W_{mhd} database. Starting from this subset we also consider shots in deuterium only. In both cases the number of entries is too small to draw substantial conclusions. In fact, as can be seen in tables 3.11 for dimensionless parameters and 3.12 for dimensional ones, the pulses in diverted plasma only are 427 and the ones that use deuterium are 250. In addition, as can be seen in the figure 3.7, the range of energy confinement time covered by the various subsets is very different from the reference one. The ranges covered by all the variables considered in the scaling law are also very different. This leads to very different and inconsistent results.

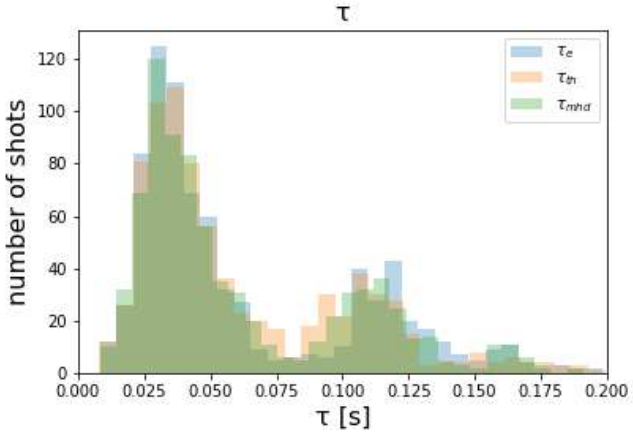

(a) comparison between τ_{mhd}, τ_{th} and τ_E

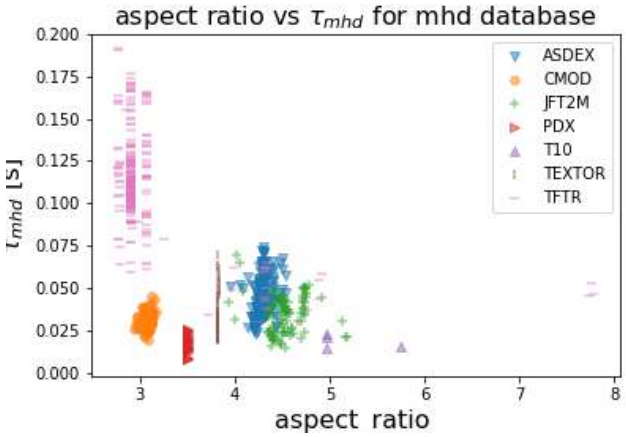

(b) τ_{mhd} as a function of aspect ratio

Figure 3.6 – τ_{mhd} comparison with the other τ definitions and with the aspect ratio

3.2.4 Exploring the impact of WEST database on the W_{mhd} database

Since taking into account the diverted plasmas and the deuterium plasmas only we have not enough entries (only 250 instead of 795), WEST plateaus are added to the W_{mhd} database (hence keeping limited and H discharges). The scaling is made with respect to τ_{mhd}, τ_{th} and τ_E and the results are summarized in the table 3.13. Again, the WEST pulses are well aligned to the others L-mode tokamaks in the W_{mhd} database, despite the fact that WEST aspect ratio is larger than previous pulses (figure 3.8).

In general, the coefficient for the aspect factor is always larger when the WEST data are added probably due to the fact that the WEST data are more than twice as large as the source database, which is why the WEST database is added totally and partially to

Variable	W_{mhd} **database**	**Diverted plasma only**	**Diverted and D plasma**
	τ_{mhd}	τ_{mhd}	τ_{mhd}
q	-2.19	-1.06	-1.28
B_T	0	0	0
k	1.71	0.38	0.79
A	-0.04	0.04	-0.54
M_{eff}	0.16	0.94	0.73
ρ_*	-1.41	-2.32	-1.55
ν_*	-0.08	-0.27	-0.14
β	-0.83	-0.11	-0.64
Entries	795	427	250
RMSE	15.9%	8%	1%
R^2	0.95	0.74	0.74

Table 3.11 – Effect of diverted plasma configuration and deuterium plasma on the energy confinement time using dimensionless parameters.

Variable	W_{mhd} **database**	**Diverted plasma only**	**Diverted and D plasma**
	τ_{mhd}	τ_{mhd}	τ_{mhd}
$constant$	0.04	0.08	0.1
I_p	0.95	0.77	0.67
B_T	-0.08	0.12	0.19
k	0.35	-0.13	0.23
A	0.06	-0.83	-1.18
M_{eff}	0.19	0.45	0.45
n_e	0.2	0.2	0.16
R	1.35	1.68	1.58
P_{tot}	-0.58	-0.42	-0.53
Entries	795	427	250
RMSE	15.9%	8%	1%
R^2	0.95	0.74	0.74

Table 3.12 – Effect of diverted plasma configuration and deuterium plasma on the energy confinement time using dimensional parameters.

the W_{mhd} database to check if the number of discharges has an impact on the scaling. The scaling coefficients are reported in table 3.14, the scaling is made with respect to τ_{mhd}. The histograms of the aspect ratio are useful to give a visual idea of the amount of WEST pulses that are added each time compared to the initial database (figure 3.9). The coefficients show an important variation especially for α_{ρ_*} which decreases and for α_β which increases.
Moreover, the β coefficients tends to decreases when the WEST data are added, this is

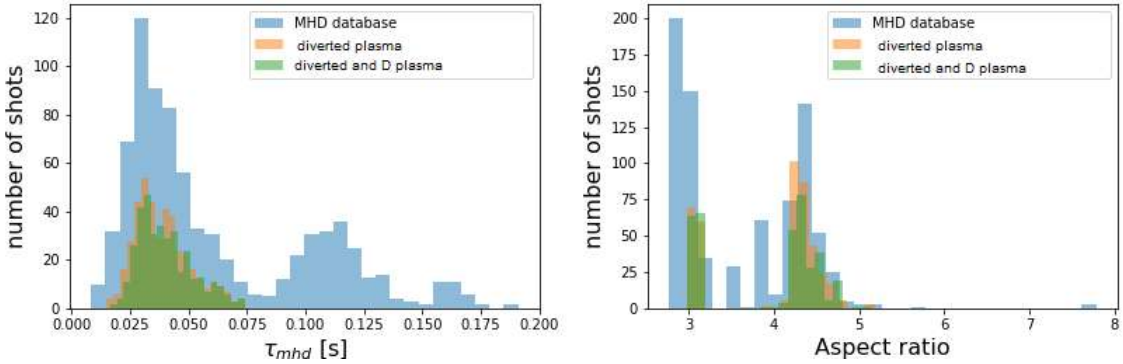

(a) Histogram of the energy confinement time using W_{mhd}, diverted plasma only and diverted plus deuterium plasma only.

(b) Histogram of the the aspect ratio using W_{mhd}, diverted plasma only and diverted plus deuterium plasma only.

Figure 3.7 – Comparison between W_{mhd}, diverted plasma only and diverted plus deuterium plasma only.

Variable	**WEST** + W_{mhd}	W_{mhd}	**WEST** + W_{mhd}	W_{mhd}	**WEST** + W_{mhd}	W_{mhd}
	τ_E	τ_E	τ_{th}	τ_{th}	τ_{mhd}	τ_{mhd}
q	-2.69	-1.85	-2.93	-2.34	-2.88	-2.17
B_T	0	0	0	0	0	0
k	1.80	1.63	1.74	1.86	1.85	1.77
A	-0.13	0.01	-0.21	-0.03	-0.13	-0.02
M_{eff}	0.26	0.38	0.41	0.60	0.03	0.22
ρ_*	-1.26	-1.58	-1.09	-1.54	-1.24	-1.55
ν_*	-0.14	-0.15	-0.06	-0.02	0.04	-0.11
β	-1.51	-0.68	-1.65	-0.87	-1.56	-0.77
Entries	1882	795	1882	795	1882	795
WEST entries	1087	-	1087	-	1087	-
RMSE	14.7%	13.8%	15%	14.5%	15.8%	15.9%

Table 3.13 – WEST plateaus added directly to ITER89-P and ITER96-L database

due to the fact that β in WEST is very small, in the range of 0.001 and 0.003.

The most important thing is that the coefficient for the aspect factor and the one for β are very close to the coefficient of the W_{mhd} database by adding only a percentage of the WEST data taken randomly. Probably the number of entries plays an important role in the scaling law as the entry data are not homogenous by entering all the WEST data.

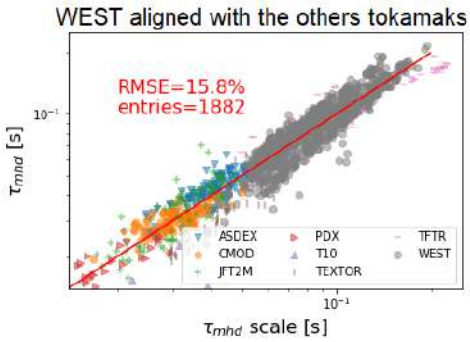

Figure 3.8 – Scaling of W_{mhd} database plus WEST database

Variable	W_{mhd}	**18% of WEST**	**30% of WEST**	**All WEST**
	τ_{mhd}	τ_{mhd}	τ_{mhd}	τ_{mhd}
q	-2.17	-2.33	-2.42	-2.88
B_T	0	0	0	0
k	1.77	1.94	1.88	1.85
A	-0.02	0.02	-0.01	-0.13
M_{eff}	0.22	0.18	0.16	0.03
ρ_*	-1.55	-1.50	-1.44	-1.24
ν_*	-0.11	-0.10	-0.10	0.04
β	-0.77	-0.98	-1.08	-1.56
Entries	795	991	1122	1882
WEST entries	-	196	327	1087
RMSE	15.9%	16.3%	16.2%	15.8%

Table 3.14 – WEST plateaus added totally and partially to W_{mhd} database

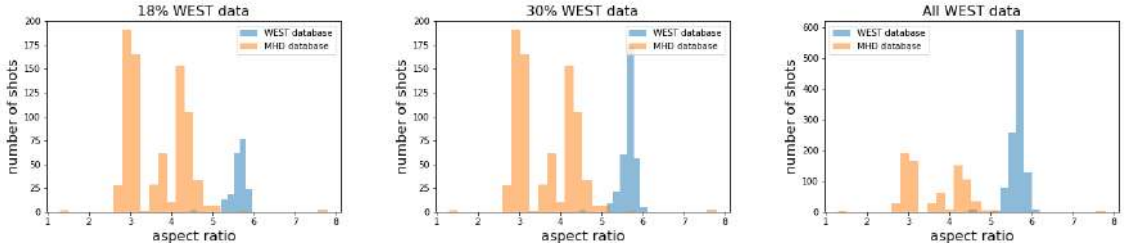

(a) 18% of WEST data added to W_{mhd} database

(b) 30% of WEST data added to W_{mhd} database

(c) All of WEST data added to W_{mhd} database

Figure 3.9 – Effect of WEST number of pulses on the scaling

3.2.5 WEST confinement comparison with ITER96-L scaling law

Since A, B, k, R and M do not exhibit large variations in the WEST present database, the WEST scaling law is derived with respect to the plasma current, line averaged electron density and total power (first line of table 3.15). The WEST discharges have a stronger plasma current dependency and an unfavourable effect of the density on the confinement with respect of to ITER-L scaling law (line 2 of table 3.15). Moreover the correlation between I_p and n_e is 0.12 as it is possible to see in table 3.16. On JET, in H-mode, higher I_p and lower n_e exponents were found with the metallic wall when compared to the previous JET configuration with the carbon wall, like the ITER 96-L database [83]. Therefore, this effect may be due to the metallic walls that characterise both JET and WEST.
Concerning the impact of density on the scaling law, at first it is interesting to note that in [20] the density dependence is $n^{0.4}$ if using the τ_{th}, but is reduced to $n^{0.24}$ when using τ_E. Therefore, the robustness of this trend is questionable. We observe a degradation of the confinement with higher density when including all I_p, and all heating schemes. The dominant LHCD heating might add some specificities as explained in the modelling presented here where we show that the central heating shifts outward for denser plasmas. Also, the coupling is more challenging at higher I_p which themselves are accompanied by higher densities.
Concerning the plasma current coefficient, as shown in figure 3.4a, the range covered by the database is 0.3-0.7 MA in which the majority of the points are at 0.5MA. Having more points between 0.3 and 0.7MA in the future will lead to a revision of the present scaling law. When the ITER96-L mode scaling law is applied to WEST data, the RMSE between predicted energy content and the measured one is 21%, while it is reduced to 12.7% when the regression is performed using WEST database.

Since, up to now, the standard L-mode scaling law is ITER96-L, the only one where WEST data could be added in the future, we add the latter to the ITER96 L-mode database. It contains 1312 entries coming from 12 different tokamaks. It is important to remind that only the τ_{mhd} is available for WEST data, while the one used for ITER96-L database is the thermal energy confinement time. It is assumed that τ_{mhd} is close to τ_{th} in WEST. Until we have the data needed to calculate τ_{th} during the WEST experiments, we cannot quantify the error between τ_{th} and τ_{mhd}, but, as shown in chapter 3.2.2 and shown in table 3.9, scaling with respect to different definitions of τ does not lead to great variations. For the moment, we consider this choice reasonable. The results of both dimensional and dimensionless scaling laws are reported in lines 3 and 5 of table 3.15. Even if WEST has an aspect ratio larger than the other tokamaks used for ITER96-L scaling law, the regression coefficient for the aspect ratio is still close to zero, this means that WEST L-mode data allow to confirm that A does not play an important role in the scaling. Although the WEST discharges are well aligned with the ITER96-L mode scaling law, there are some important differences when comparing the exponents of the dimensionless parameters. The uncertainty

on these parameters is intrinsically larger than that on the dimensional parameters [26]. When the Kadomtsev transformation is used, $(1+\alpha_P)$ appears as denominator in each coefficients transformation formula and a weak variation of α_P leads to a big change in the dimensionless coefficients.

Variable	I_P	n_e	P_{tot}	**A**	B_T	**k**	**R**	M_{eff}	**Ent.**
τ_{mhd} WEST	1.30	-0.20	-0.73	-	-	-	-	-	1083
τ_{th} ITER96	0.96	0.40	-0.73	0.06	0.03	0.64	1.83	0.20	1313
ITER96 + WEST	1.06	0.23	-0.73	0.15	0.09	0.53	1.55	0.19	2396
Variable	**q**	B_T	**k**	**A**	M_{eff}	$\rho_\star$	$\nu_\star$	β	**Ent.**
τ_{th} ITER96	-3.74	0	3.22	0.04	0.67	-1.85	-0.19	-1.41	1313
ITER96 + WEST	-3.92	0	3.18	-0.15	0.49	-1.57	0.02	-1.84	2396

Table 3.15 – Coefficients of the dimensional and dimensionless scaling laws for WEST database (line 2), ITER96 database (line 3 and 6 and WEST database merged with ITER96 database (line 4 and 7).

To highlight the level of correlation between the regression parameters, the correlation matrix is reported in table 3.16.

Variable	I_P	B_T	P_{tot}	n_e	**k**	**R**	M_{eff}	**A**
I_P	1	-	-	-	-	-	-	-
B_T	0.32	1	-	-	-	-	-	-
P_{tot}	0.74	0.45	1	-	-	-	-	-
n_e	0.12	0.30	0.17	1	-	-	-	-
k	-0.04	-0.10	-0.18	0.19	1	-	-	-
R	0.45	0.48	0.52	-0.26	-0.08	1	-	-
M	-0.12	0.15	-0.21	0.12	0.33	0.07	1	-
A	-0.77	0.16	-0.45	0.03	0.17	0.05	0.26	1

Table 3.16 – Correlation matrix for WEST database merged with ITER database.

As expected, there is a general correlation between plasma current and the heating power. The correlation between plasma current and aspect ratio is the result of the $B_{tor}/(I_p A)$ dependence of the safety factor q which does not vary by more than a factor 2 for most of the discharges.

It is important to note that in the ITER96-L database the radiated power has not been subtracted from the total power as this is a small fraction of the total power. For WEST, this assumption is not valid, as the radiated power in the core is high due to the rather large density of tungsten but the fraction of the input power which is radiated

is weakly sensitive to the power and density. When the radiated power is subtracted to the input power the coefficients are weakly affected as shown in the table 3.17. The power used to evaluate the energy confinement time and the regression coefficient is computed as $P_{tot} - P_{rad,bulk}$. The latter is computed for the inverse of bolometry has explained before in the thesis.

Variable	I_P	n_e	P_{tot}	**A**	B_T	**k**	**R**	M_{eff}	**Ent.**
τ_{th} ITER	0.96	0.40	-0.73	0.06	0.03	0.64	1.83	0.20	1313
ITER + WEST	1.01	0.26	-0.76	0.15	0.18	0.63	1.68	0.22	2396
Variable	**q**	B_T	**k**	**A**	M_{eff}	$\rho_\star$	$\nu_\star$	β	**Ent.**
τ_{th} ITER	-3.74	0	3.22	0.04	0.67	-1.85	-0.19	-1.41	1313
ITER + WEST	-4.30	0	3.22	0.01	0.73	-1.62	-0.09	-2.18	2396

Table 3.17 – dimensional and dimensionless scaling laws for WEST database (line 1), ITER database (line 2 and 5 and WEST database merged with ITER database (line 3 and 6).

3.2.6 Impact of radio frequency heating scheme on the energy confinement time

To better understand the effect of different heating schemes on the energy confinement time, the WEST database has been split such that: $P_{LH} > 1MW$ (859 plateaus), and $P_{ICRH} > 1MW$ (119 plateaus).
As previously, the linear regression is made taking into account the plasma current, the line-averaged electron density and the total power, since all the other variables are constant. The same analysis has been made taking into account the total radiated power in the bulk. Therefore, a new value of the energy confinement time is defined: $\tau_{rad} = \frac{W_{mhd}}{P_{sep}}$ with $P_{sep} = P_{tot} - P_{radbulk}$.
All the coefficients obtained are summarized in table 3.18, and in figure 3.10 the experimental data are plotted as a function of the scaling law. The plasma current is used as colourbar to highlight the fact that for the ICH scaling law a more restricted range of I_p values is used.

The number of high power ICRH pulses is probably too low to conclude its impact on energy confinement time. Nonetheless, the dependency with respect to density with LHCD is the inverse of the one wit ICRH. This might reflect the fact that dense plasmas lead to LHCD absorption more outward.
It is important to note that the density ranges are both quite large with a maximum around $7x10^{19}m^{-3}$ and a minimum of $1.2x10^{19}m^{-3}$ for the LH database and $3x10^{19}m^{-3}$ for the ICH database. Both have most discharges around $4x10^{19}m^{-3}$.
Interestingly, the power degradation exponent is larger when the bulk radiation is

	I_p	n_e	P_{tot}	$RMSE$	**Ent.**
τ_{icrh}	0.99	0.16	-0.75	6.5%	119
$\tau_{icrh,rad}$	1.05	0.22	-0.80	7.3%	119
τ_{lh}	1.28	-0.23	-0.73	13.7%	859
$\tau_{lh,rad}$	1.32	-0.18	-0.82	15.1%	859

Table 3.18 – Comparison between the LH and ICRH RF heated plateaus ($P_{LH} > 1MW$ and $P_{ICH} > 1MW$) with and without the power radiated in the bulk

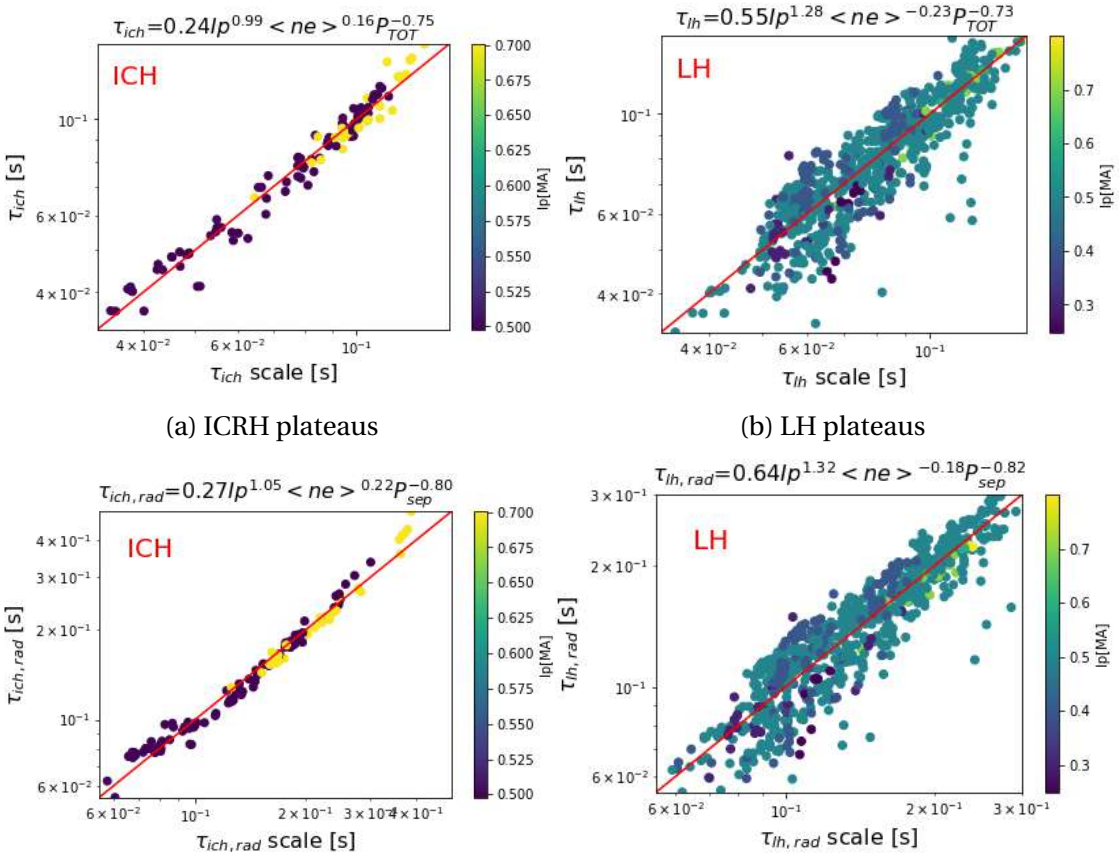

(a) ICRH plateaus

(b) LH plateaus

(c) ICRH plateaus and τ_{rad}

(d) LH plateaus and τ_{rad}

Figure 3.10 – Experimental energy confinement time plotted as a function of the scaling value

removed. In this database, $\frac{P_{rad,bulk}}{P_{tot}} \sim 50\%$. Hence, the degradation of the confinement time due to the turbulent transport only is larger than with both turbulent and radiative losses.

3.2.7 Density impact on the energy confinement time

The ohmically heated pulses are analysed, therefore, the database is filtered taking into account only the ohmic phase. Plotting the experimental energy confinement time as a function of the line-averaged electron density (figure 3.11a) the change of confinement time from linear ohmic confinement regime (LOC) to saturated ohmic confinement regime (SOC) has been observed [84]. At low density, there is a linear increase in the global energy confinement time (often called Alcator scaling), which saturates at high density. The confinement saturation density is seen to increase at higher I_p.

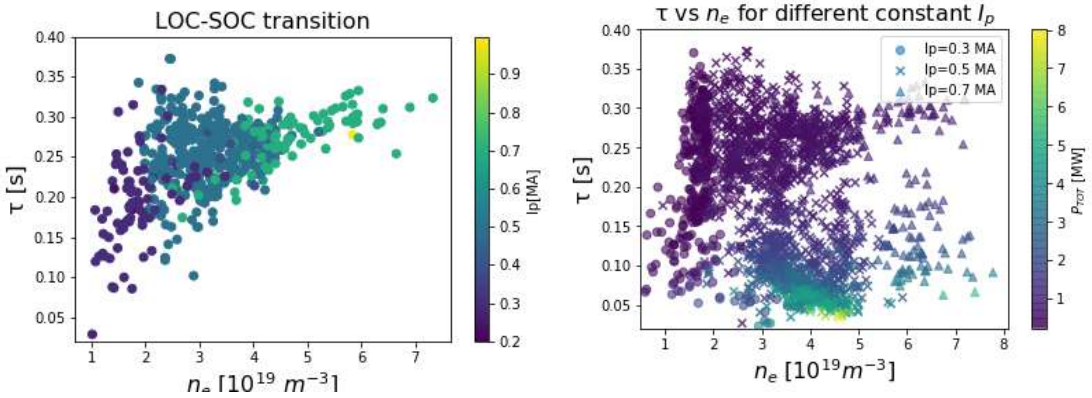

(a) LOC-SOC transition for the ohmic WEST pulses

(b) Experimental energy confinement time plotted as a function of the line-averaged electron density for three plasma current.

Figure 3.11 – Density effect on WEST energy confinement time

Then, all the plateaus have been considered and the database has been split into three plasma current ranges, around 0.3 MA, 0.5 MA and 0.7 MA. Again, the experimental energy confinement time is plotted as a function of the line-averaged electron density and the points have been colored by the total power. The figure 3.11b confirms that for low powers, the LOC-SOC transition is also observed for increasing plasma current that allow higher densities. On the contrary, for increasing power, we enter L mode and no LOC nor SOC trends are visible.

To understand how the coefficients vary as a function of injected power, the database has been filtered by a range of increasing P_{aux} level. The first regression is made on the whole database, then a threshold in P_{aux} is imposed and the linear regression is applied on the plateaus with P_{aux} larger than the threshold. Three P_{aux} are selected: 1 MW, 2 MW and 3 MW. The same analysis is made also subtracting the power radiated in the bulk (figure 3.12). Concerning the latter, the confinement degradation is enhanced up to $P_{aux} = 2MW$ as reported in table 3.18 for LH and ICH, while at $P_{aux} = 3MW$ the power degradation is significantly reduced. This will be further inves-

tigated in the future WEST operation as high power discharges become more common.

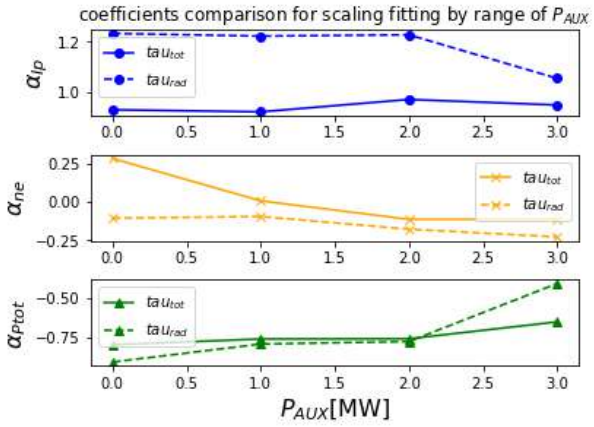

Figure 3.12 – Coefficients behaviour with respect to P_{aux} level, and subtracting (dashed lines) or not the $P_{rad,bulk}$ (full lines).

The same trend is observed on the scaling exponents considering the total power and the total power minus the power radiated in the bulk. For α_{I_p}, the coefficient variation is not too large. Regarding the line-average electron density coefficient, not only is the variation large, but the coefficient also changes sign. At large P_{tot} the interval of variation of n_e is very narrow, this means that the density coefficient is not really meaningful, but the variation from $Paux = 0MW$ and $Paux = 2MW$ still important. To conclude, some difficulties arise in obtain the density coefficient using a power law. In fact, as shown in figure 3.11b, a large dispersion of points arises if the line averaged electron density is plotted as a function of the energy confinement time in other words, a linear correlation between density and energy confinement time is not visible in the same way as, for example, it is visible with total power or plasma current.

3.2.8 Best features selection

After analysing in details the standard eight dimensional and dimensionless variables of the linear power law, the work has focused on looking for best variables which provide an optimized fit to the data.
Even thought the plasma current is a good parameter to extrapolate the energy confinement time thanks to its linear dependence robustly observed on of each machine and in between machines, at highest current the plasma is unstable when $q_{95} < 2$.

Characterization of energy confinement in tokamaks is essential for developing and testing candidate theories and models for energy confinement and for identifying the parameters that should be emphasized in the design of the next generation of experiments. It is difficult to characterize these data. First, The confinement losses

clearly depend on other variables as well, such as the plasma profile, current profile, heating profile, MHD behaviour and plasma-wall interactions, so that the set of eight variables normally used is incomplete. A second problem is that the functional form of the dependence of the energy confinement time τ_E on the parameters is unknown. Moreover, there are collinearities in the data which are due to the lack of independent variation of these eight parameters over the database.
The scaling of τ_E with density and plasma current varies strongly from device to device. The dominant scaling of τ_E with I_p is $I_p^{\alpha \pm \beta}$, with $\alpha \sim 1$ and $\beta \leq 0.2$. The variation in β from tokamak to tokamak can be interpreted as being due to the variation in the scaling with respect to q. Moreover, the scalings with current and density are linked because higher current operation is often accompanied by higher operating densities and therefore the density and current variations are correlated. These different dependences may also be due to different operating conditions and parameters that are not included in the database.
Therefore, even though the plasma current is a good parameter to extrapolate the energy confinement time thanks to its linear dependence robustly observed on of each machine and in between machines, the variation in the scaling with current among tokamaks can be included by introducing a factor q_{eng} to reflect the variation with q (and implicitly Ip) defined as [85]:

$$q_{eng} = \frac{5Ba^2k}{I_pR} \tag{3.4}$$

The new scaling coefficients obtained applying the linear regression on the database made up of ITER96-L and WEST database are summarized in the table 3.19.

	coef.	q_{eng}	I_p	B_T	P_{tot}	n_e	M_{eff}	**R**	a	**k**
ITER96-L + WEST	0.033	-	0.95	0.12	-0.73	0.26	0.20	1.60	0.07	0.59
ITER96-L + WEST with q_{eng}	0.16	-1.02	-	1.09	-0.73	0.21	0.20	0.67	1.96	1.57

Table 3.19 – Comparison of the classic scaling coefficients with the ones obtained using q_{eng} instead of I_p

The coefficient for B_T parameter increases when changing from I_p to q_{eng}, while P_{tot} exponent does not change since $\alpha_{P_{tot}}$ is not modified changing from I_p to q_{eng}.

Another important quantity is the amount of loss power. In the L-mode database the power degradation of each machine individually is observed, while both the power and the confinement time increase with increasing size. This latter remark suggests that the power density would be a better parameter and is actually a better engineering variable in order to evaluate a machine efficiency. It is defined as $P^* = \frac{P_{tot}}{\text{Plasma volume}}$. As shown in figure 3.13b, the machines seem to align well with respect to this parameter (except for CMOD). The power density is considered instead of the total power in the linear regression and the results are reported in table 3.20. It can be observed that, once again, the coefficient of the power does not change from P_{tot} to P^*, thus the power degradation remains similar using P^* instead P_{tot}.

	coef.	q_{eng}	I_p	B_T	P^*	P_{tot}	n_e	M_{eff}	**R**	**a**	**k**
ITER96-L + WEST	0.033	-	0.95	0.12	-	-0.73	0.26	0.20	1.60	0.07	0.59
with q_{eng}	0.16	-1.02	-	1.09	-	-0.73	0.21	0.20	0.67	1.96	1.57
with q_{eng} and P^*	0.02	-0.96	-	1.12	-0.74	-	0.22	0.20	-0.07	0.49	0.92

Table 3.20 – Comparison of the classic scaling coefficients with the ones obtained using q_{eng} instead of I_p and P^* instead of P_{tot}

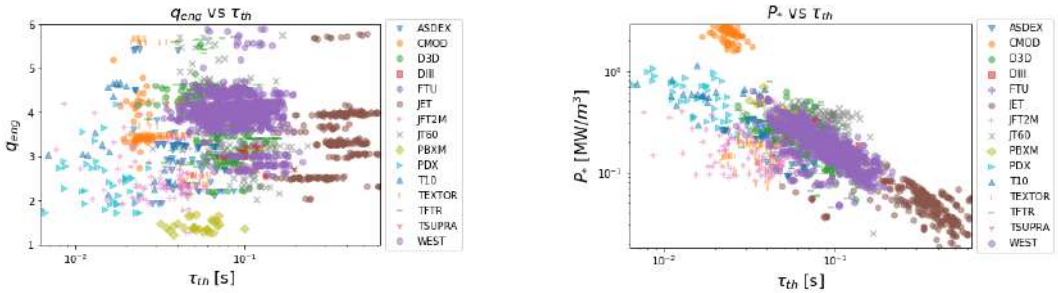

(a) q_{eng} as a function of τ_{th} an colored by tokamaks

(b) P^* as a function of τ_{th} an colored by tokamaks

Figure 3.13 – q_{eng} and P^* as a function of τ_{th}. Note that for the WEST machine the τ_{mhd} are used

The dependence of the energy content on the volume size is already included in P^*, therefore only a linear dependence of τ on the size remains. Assuming that the B exponent, that is very close to 1, is compensated by the q_{eng} dependence, the

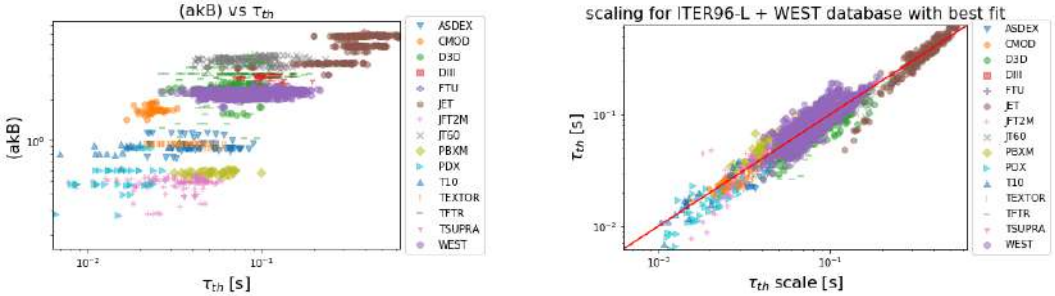

(a) (akB) as a function of τ_{th} an colored by tokamaks

(b) Experimental energy confinement time plotted as a function of the scaling value obtained

Figure 3.14 – Note that for the WEST machine the τ_{mhd} are used

product (akB) is considered as one single variable (figure 3.14a). The scaling is made considering only q_{eng}, P^*, n_e and (akB) and imposing the Kadomtsev constraint:

$$-\alpha_{(akB)} - 15\alpha_P - 8\alpha_n = 5 \tag{3.5}$$

The results are in table 3.21 with a RMSE of 20.4%, hence larger than reference 15.8% (figure 3.14b) [86].

	coef.	q_{eng}	I_p	B_T	P^*	P_{tot}	n_e	M_{eff}	**R**	**a**	**k**	(akB)
ITER96-L + WEST	0.03	-	0.95	0.12	-	- 0.73	0.26	0.20	1.60	0.07	0.59	-
with q_{eng}	0.16	- 1.02	-	1.09	- 0.73	-	0.21	0.20	0.67	1.96	1.57	-
with q_{eng} and P^*	0.02	- 0.96	-	1.12	- 0.74	-	0.22	0.20	- 0.07	0.49	0.92	-
with q_{eng}, P^* and (akb)	0.02	- 0.56	-	-	- 0.66	-	0.53	-	-	-	-	0.70

Table 3.21 – Comparison of the classic scaling coefficients with the ones obtained using q_{eng} instead of I_p and P^* instead of P_{tot}.

Another reasonable approach consists in performing the regression with respect to the three parameters that contain the majority of the information in the scaling with respect to the observed thermal confinement time. Looking at the correlation between τ and the eight engineering parameters, they are I_p, P_{tot} and R. Again, the ITER96-L plus WEST database is considered and the τ_{mhd} of WEST is supposed to be equal to τ_{th}.

The scaling of the thermal energy confinement time obtained is:

$$\tau_{th} = 0.07 I_p^{1.02} P_{tot}^{-0.73} R^{1.60} \tag{3.6}$$

with an RMSE of 22.7%. Nevertheless, these parameters show very high correlation values between them, as shown in table 3.16.

Another approach to identify which are the most relevant parameters that effect the energy confinement time consists in applying a model known as Recursive Features elimination (RFE [30]). In principle, the number of independent variables is increased and the algorithm selects features by recursively considering smaller and smaller sets of features until the desired number of features selected is reached. In this work the number of features selected is three. The three variables chosen from the algorithm correspond to those that minimize the residual sum of squares between the observed targets and the predicted ones, since a linear regression is chosen as the resolving model.

The new independent variables that are taken into account are:

— the fraction of radiated power defined as the ratio between the total radiated power and the total power, $f_{rad} = \frac{P_{rad,tot}}{P_{tot}}$;

— the radiated power P_{rad};

— the products of the minor radius, the elongation and the toroidal magnetic field (akB);

— the density peaking factor defined as the ratio of the line-averaged electron density and the volume electron density, $dpf = \frac{n_e}{n_{e,vol}}$;

— the simplified cylindrical approximation of the safety factor, $q_{eng} = \frac{5B_T a^2 k}{I_p R}$;

— the fraction of the total power and the plasma volume, $P^* = \frac{P_{tot}}{volume}$;

— the value of the safety factor at 95% of the toroidal flux, q_{95};

— the Greenwald function defined as $n_G = \frac{I_p}{\pi a^2}$ measured in $10^{20} m^{-3}$;

The model is applied to ITER96-L database and to ITER96-L plus WEST database

to highlight the effect that WEST has on the L-mode database. In the table 3.22a, the features ranking for ITER96-L is reported, in table 3.22b the ranking for ITER96-L plus WEST is listed.

RFE ranking for ITER96-L			
1	n_G	7	f_{rad}
1	P_{tot}	8	P_{rad}
1	P^*	9	n_e
2	B_{tor}	10	dpf
3	(akB)	11	q_{95}
4	R	12	M
5	I_p	13	q_{eng}
6	k	14	ϵ
RMSE		18.2%	

(a) RFE applied to ITER96-L database.

RFE ranking for ITER96-L+WEST			
1	R	7	f_{rad}
1	I_p	8	P_{rad}
1	P_{tot}	9	q_{95}
2	(akB)	10	q_{eng}
3	B_T	11	dpf
4	P^*	12	n_e
5	n_G	13	ϵ
6	k	14	M
RMSE		21%	

(b) RFE applied to ITER96-L plus WEST database.

Table 3.22 – Ranking made by RFE method

The main eight variables selected by the method are the same but the ranking is different. This might be due to the different correlations that exist between the variables in the two databases. The first thing to note is that the seven first parameters are the same. The second thing is that the three parameters that minimize the error in the ITER96-L database are different from those selected using the regression coefficients presented on table 3.15. Moreover the variable (akB) seems to play an important role in scaling laws, for both ITER96-L and ITER96-L plus WEST database. Furthermore, the Greenwald fraction seems to be more important than the line-average electron density, probably because it has the plasma current at the numerator. The algorithm selects both the total power and the power density, there is probably a high collinearity between the two data. One of the two variables should be eliminated from the analysis to get more consistent results. Therefore, a future work could be to add new variables which are combinations of the original ones instead of replacing them.
Anyway, an important aspect is that the aspect ratio is not among the most important parameters. This shows again that aspect ratio is not a significant regressor for confinement time scaling law in L mode, even if a and R still high in the list.

3.3 Conclusion of the chapter

The two scaling laws ITER89-P and ITER96-L are well reproduced both in dimensional and dimensionless parameters and their different aspect ratio scaling has been analysed. In particular, the differences come from a gap between aspect ratio values between 4.4 and 5.5. This is due to the discharges in single null configuration of JT-60

tokamak. For these pulses the τ_{th} is not available and, moreover, they are characterized by a smaller plasma volume that correlates with degradation of the energy confinement time.

The WEST database is constructed. It contains only L-mode, deuterium pulses, in lower single null configuration and with a low error with respect to interferometry measurements.
At this stage of WEST operation, the only available value for the energy confinement time is τ_{mhd}, therefore a subset of the L-mode database is selected. In particular, only the discharges for which the τ_E, τ_{th} and τ_{mhd} are available and their difference doesn't exceed 30%.
These parameters are used to determine the scaling law for τ_{mhd}. The large dispersion of data points with aspect ratio suggests that this quantity has a limited impact on the energy confinement time.
WEST plateaus are added to this reduced database and a scaling with respect to τ_{mhd} is determined. WEST is well aligned to the other L-mode tokamaks despite the fact that it has a larger aspect ratio confirming the weak aspect ratio dependence on the confinement time reported in ITER96-L.

Since A, B, k, R and M_{eff} are fixed in WEST operation, the scaling law for WEST alone is derived with respect to the plasma current, line averaged electron density and total power. The WEST discharges have a stronger plasma current dependency and an unfavourable effect of the density on the confinement time with respect to the ITER96-L scaling law.
When WEST data are added to ITER96-L, assuming that τ_{mhd} is close to τ_{th} and the scaling in both dimensional and dimensionless variables are determined, the regression coefficient for the aspect ratio is still close to zero.
To analyse the impact of the fraction of the radiated power, the latter is subtracted to the total power and the scaling is applied. Also in this case, the coefficients are weakly affected if the whole WEST database is considered.

In WEST, heating schemes impact is explored. The LHCD heating has a deleterious effect for the density dependence, so that a negative trend is observed (3.10).
Regarding the ohmic pulses, the change of confinement time from linear ohmic confinement regime to saturated ohmic confinement regime is observed.
Finally, using a feature selection algorithm, we show that aspect ratio parameter does not appear to be an important regressor for L-mode confinement time in tokamaks.

4 Confinement regimes and radiative collapses in WEST

4.1 Introduction of the chapter

In this section it is explained how the radiative collapse has been identified in WEST and its time evolution is shown.
First of all, the diagnostics useful for the analysis are introduced. A particular attention has been placed on the bolometry and its inversion, since this diagnostic is used to estimate the tungsten density profiles during the discharges.
Also the ECE radiometer, the hard X-ray and the interferopolarimetry have been described.
Two energy confinement states have been identified in WEST operation: the hot branch linked to a high central electron temperature and the cold branch characterized by a temperature around 1.5 keV.
Then, a simple model to detect the collapse in WEST database is developed. It has been shown that all the collapsing plateaus are in the range of 1.5 keV and 3 keV and this is in agreement with the tungsten cooling factor unstable region.
It has been shown that, in general, a collapse is characterized by a first slow decrease of the temperature and a slow increase of the electron density, a decrease of the signal of the hard X-ray central channel as a signature of the central LHCD absorption modification and a tungsten accumulation in the center of the plasma.
A simple 0D model of the collapse is detailed but a comparison with the experimental data is not possible.
Finally some possible solutions to avoid the collapse are presented, in particular, the boronization and the ICRH heating.

4.2 WEST diagnostics

4.2.1 Bolometry and bolometry inversion

WEST is equipped with two bolometric cameras in one horizontal port (in total 16 lines of sight or chords), that cover the whole plasma cross-section. This diagnostic is used to measure the total spectrum of radiated power from the plasma.

A bolometer measures a line-integrated value of the local radiative emissivity along a viewing line of sight. From this information, we extract the distribution of the

local radiation emissivity in the poloidal cross section of the plasma. The inversion of the radiation from the bolometry measurement is computed. A concentric layer decomposition of local plasma emissivity is assumed together with asymmetric factors in the SOL and edge of confined plasma. Thanks to the inversion, the power emission in W/m^3 for each layer is estimated (figure 4.1).

For the database used in the analysis, the plasma cross-section has been divided in 7 layers. Each layer corresponds to a ψ value (normalised poloidal magnetic flux) at external boundary equal to 0.05, 0.2, 0.4, 0.6, 0.8, 1, 1.15. In figure 4.1 the emissivity map for pulse 55025 in the time interval 8s-8.5s is shown. For each layer the radiated power density is computed and is shown in the plot on the right [87].

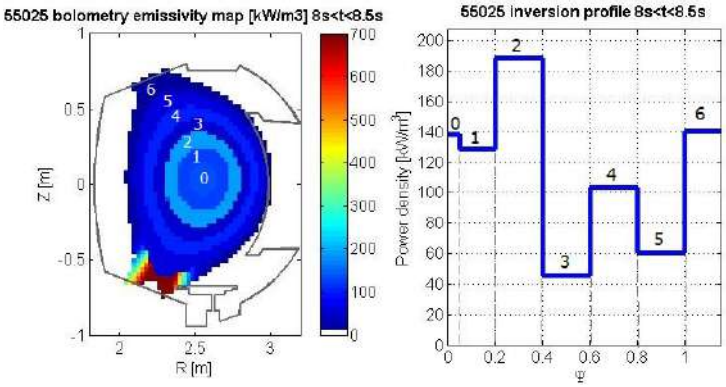

Figure 4.1 – Emissivity map from inverse of bolometry for discharge 55025 for time interval 8s-8.5s. The plasma volume is divided into 7 layers and for each of them the radiated power density is computed.

The tungsten density profiles are estimated from the radial power density. From figure 4.2 in Ref. [88] the cooling factor of different elements as function of the electron temperature is shown. Above 1 keV, for a given concentration, the main radiator is tungsten. Therefore, in a tungsten environment, it is reasonable to assume that the majority of emitted radiation computed by the bolometry inversion is due to tungsten, for $T_e > 1keV$.

The tungsten density profiles have been estimated using the formula:

$$n_W(\psi) \sim \frac{P_{rad,W}(\psi)}{n_e(\psi) L_W(T_e(\psi))}. \tag{4.1}$$

Where $P_{rad,W}$ in [W/m^3] is obtained from the bolometry inversion, $L_W(T_e)$ is the tungsten cooling factor taken from ADAS 50 database and $n_e(\psi)$ is the density profile from interferometry. Moreover, the P_{rad} is an averaged quantity for a given layer whereas n_e and T_e are taken as full profiles. Notice that it is a multiple charge density estimation since the cooling factor is computed for radiation due to recombination including bremsstrahlung and the mean charge of the ionization equilibrium for

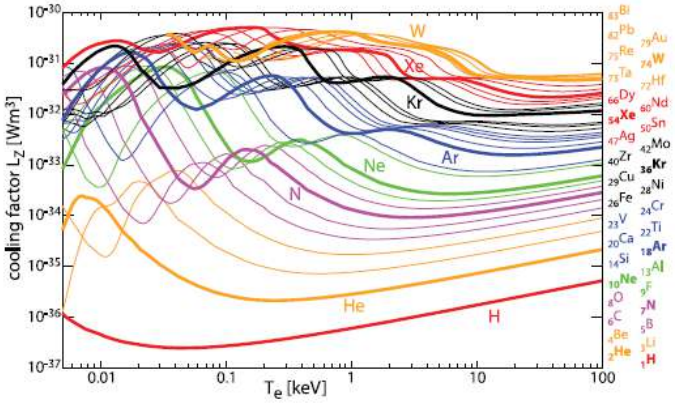

Figure 4.2 – Cooling factor for different elements taken from OPEN-ADAS database. Above 1 keV the main radiator is tungsten [88].

different electron temperatures as explained in ref. [74].
As shown in figure 4.3, a tungsten density profile is computed for each time, therefore it is possible to extract the tungsten density evolution at each layer.

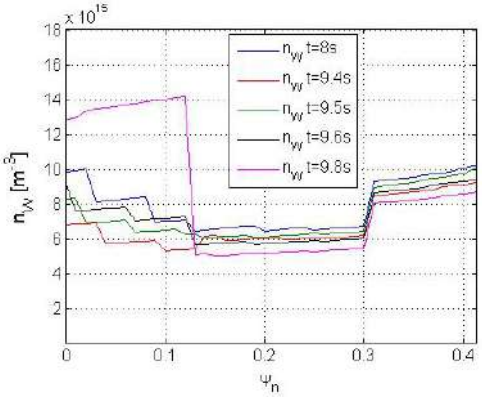

Figure 4.3 – Tungsten density profiles at different times of the pulse 55025.

For this discharge, the profiles are accurate up to $\psi = 0.4$ because the cooling factor of W is not well known for temperature below 1 keV. Hence the inversion from bolometry cannot be applied for $T < 1keV$ [74]. In WEST there are also mid-Z impurities such as Copper as well as low Z impurities such as Carbon, Oxygen and Nitrogen. The cooling factor of copper is 30 times lower than the one of tungsten for a temperature of 3 keV and reconstruction of the central soft X-ray and bolometry chords indicates that copper can be the main radiator at the plasma periphery ($\frac{r}{a} > 0.8$) but does not contribute to the total bulk radiation by more than 20%.

4.2.2 ECE heterodyne radiometer

The electron temperature profiles are computed using the ECE heterodyne radiometer. It is composed by 32 channels and it measures the whole low field side (LFS)

radial Te profile and part of high field side (HFS) profile from a midplane port. The diagnostic collects electron cyclotron emission (ECE), from which the electron temperature profile is determined. Two acquisition systems can be used simultaneously: a standard acquisition mode allows the 32 channels to measure at 1 ms time sampling for the whole plasma duration (useful for temperature profile measurements); a fast acquisition mode allows the 32 channels to measure at $1\mu s$ time sampling for a time window either preset or triggered by a given plasma event (useful for MHD).

The 1D ECE diagnostic produces raw data for 32 channels dispatched in four groups of 8 channels. The data treatment requires a n_e profile derived from interferometry for assessing the optical depth of the plasma. The data treatment produces: calibrated T_e values (eV), with errorbars; a position of the measurement for each time step; an estimate of the optical depth of the plasma at 1 keV, for each channel and time step [89].

Note that in presence of LHCD, fast electrons pollute some channels of the ECE signal, hence $T_e(\rho)$ is available only for $\rho < 0.5$.

4.2.3 Hard X-Ray

Fast electron Bremsstrahlung emission provides an insight of the localization of non-thermal electrons generated by Landau damping of the Lower Hybrid (LH) wave. The fast electron diagnostic is designed to record in real-time this suprathermal emission in the hard X-ray range between 20 and 200keV. The location and energy of the suprathermal electrons created by resonant interaction with LH, as well as the dynamics of their distribution is obtained. This system allows us to constrain the LH power absorption profile.

The diagnostic consists of 38 detectors in a horizontal camera. Photon energies $h\nu$ between 20 and 200 keV are discriminated by an eight-channel spectrometer of width $\Delta h\nu$ = 20 keV for each chord, which allows investigating the electron dynamics from the Maxwellian bulk to the non-thermal tail at all plasma radii [90].

4.2.4 Interferopolarimetry

The diagnostic is a combined Far Infrared 10 channels interferometer and polarimeter.
For the interferometer part, the two used wavelength are 194.7 and 118.6 μm. The polarimetric part uses the 194.7 μm wavelength.
For each channel, 3 detectors are used to characterize the beams: one for the 118.6 μm beam and the 2 others for the perpendicularly polarized components of the 194.7 μm beam.
Before reaching the detectors, the infrared beams are recombined with 100 kHz shifted in frequency beam in order to produce sine signals at this frequency, which enables to measure the phase of the signals. The separation of the 2 wavelength superposed beams is done by a grid before reaching the detectors.

It is used to produce real time line integrated/averaged electron density measurements. Also the post pulse low frequency line electron density measurements and Faraday angles are used for n_e and current density profiles reconstructions.

For each of the 10 channels, 3 detectors are used to characterize the beams. The 8 channels numbered 3 to 10 are the equatorial port channels, the beam crosses twice the plasma as it is reflected on a corner cube mirror that is fixed on an internal panel. They are regularly spaced from the normalized radius $\rho = 0$ to 0.6, the exact value depending on the plasma scenario. Two other channels, named 1 and 2, are coming from a vertical port through mirrors under the baffle, then being reflected on corner cube mirrors. Channel 1 is pointing in the X point region and Channel 2 is an edge plasma measurement in the $0.8 < \rho < 1$, depending on the position of the plasma [91].

4.3 Analysis of the power radiated fraction in the core from inverse of bolometry

Thanks to the bolometry inversion the core radiated peaking factor is computed for whole database. It is defined as the ratio between the power radiated in the core (layer 0 at $\Psi = 0.05$) and the total radiated power. It is interesting to plot this quantity as a function of central electron temperature and colour by the total power for both the LH and ICH pulses (figure 4.4).

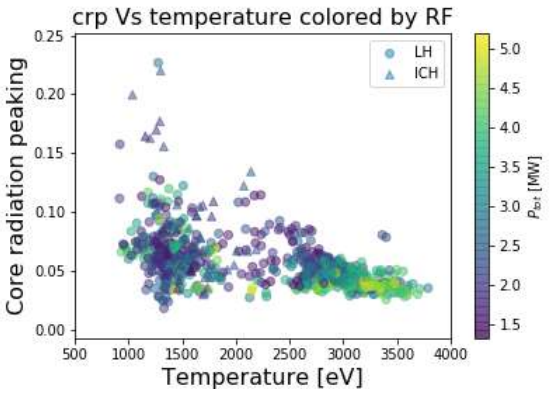

Figure 4.4 – core radiated peaking factor as a function of central electron temperature coloured by the total power for both LH and ICH pulses.

As it is possible to notice, the core radiated peaking factor decreases with increasing central electron temperature. This suggests that high central temperature plasmas are achieved when central radiation peaking is small. Moreover, it is possible to conclude that the RF heating has no impact on the core radiation peaking since the LH and ICH discharges seem to overlap. This conclusion is confirmed with the plot of the core radiation peaking as a function of neutron flux divided by n_e^2. The latter quantity is

used as a proxy of T_i^2. Also no clear difference between LH and ICH is observed on figures displaying core radiation peaking as a function of neutron flux, plasma energy content and density peaking factor as a function of the central temperature (figure 4.5).

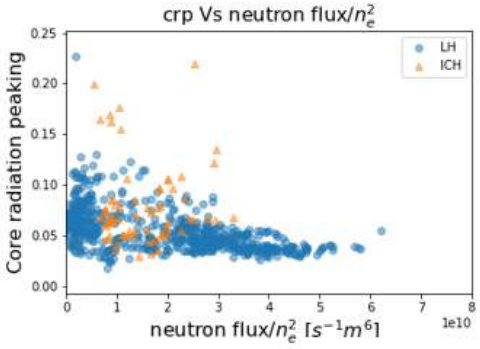

(a) Core radiated peaking factor as a function of neutron flux divided by the square of the electron density and coloured by RF heatings.

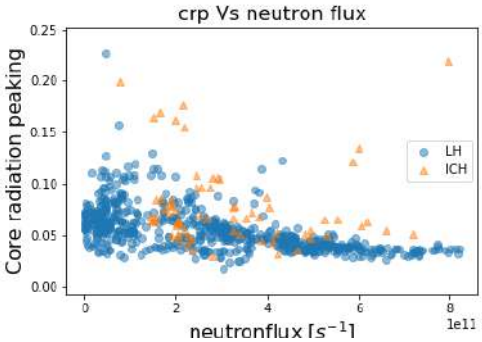

(b) Core radiated peaking factor as a function of neutron flux and coloured by RF heatings.

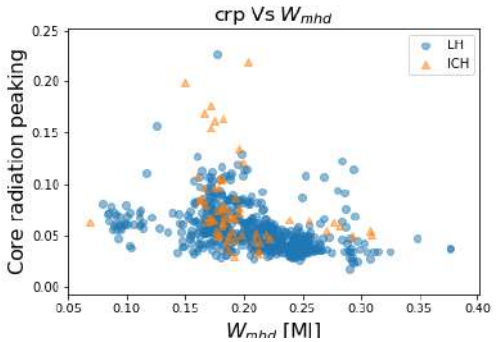

(c) Core radiated peaking factor as a function of plasma energy content and coloured by RF heatings.

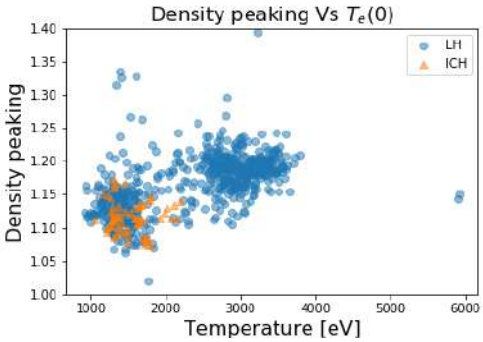

(d) Density peaking factor as a function of central electron temperature coloured by RF heatings.

Figure 4.5 – RF heating impact on core radiation peaking.

Although discharges with only ICH are very few, LH and ICH pulses are quite overlapping. Removing the outlier pulses (the ones with an high core radiation peaking for a low temperature, i.e. low power), the LH and ICH heating systems lead to the same core radiation peaking. The reason why the temperature reached in the center of the plasma using ICRH heating is lower seems to be related to the fact that it heats up more the ions.

4.3.1 H_{WEST} factor and hot/cold branches

In the previous chapter, we explained that WEST 1083 entries have been added to the ITER L mode database [33] and confirm the low aspect ratio dependence of the ITER96 scaling law ($A^{0.06}$). The typical regressors for the energy confinement time are the plasma current (I_p), the total power (P_{tot}), the line averaged electron density ($\overline{n_e}$), the toroidal magnetic field, the major radius, the elongation and the aspect ratio. Since in WEST operation the geometrical parameters and the toroidal field do not vary (within 20%), the data have only been normalized with respect to three main regressors: the plasma current, the total power and the line averaged electron density. Compared to the ITER96-L mode scaling, we find a higher α_{I_p} and a lower $\alpha_{\overline{n_e}}$ exponents. The dominant LHCD heating might add some specificities as explained in the modelling presented here where we show that the central heating shifts outward for denser plasmas and how it is already explained in section 3.2.5.
The obtained regression coefficients (table 4.1) are used to compute a predicted energy confinement time called $\tau_{scaling}$.

	α_{I_p}	$\alpha_{\overline{n_e}}$	$\alpha_{P_{tot}}$	RMSE
ITER96-L	0.96	0.40	-0.73	18.9
WEST	1.35	-0.16	-0.75	13

Table 4.1 – Regression coefficients for ITER96-L and WEST databases.

Dividing the real energy confinement time taken from the experiment by the one from the scaling, H_{WEST} factor is computed with the formula:

$$H_{WEST} = \frac{\tau_{mhd,measured}}{\tau_{scaling}} \tag{4.2}$$

This quantity is a useful to quantify the quality of the confinement time for a given discharge.
The most significant plasma parameters were taken into account, such as:

— central electron temperature, $T_e(0)$;

— temperature peaking, $\frac{T_e(0)}{T_e(0.6)}$;

— internal inductance, li;

— core radiation peaking, $\frac{layer0}{\text{core radiated power}}$;

— neutron flux;

— safety factor at the axis, q_{axis};

— edge electron density at $\rho = 1$, $n_{e,edge}$;

— plasma elongation;

— radial outer gap, ROG (distance in outboard mid-plane between plasma and the closest antenna);

— X point distance, X_{dist} (normal distance between point X and the divertor);

— fraction of radiated power, $f_{rad} = \frac{P_{rad}}{P_{tot}}$;

— fraction of radiated power in the bulk, $f_{rad,bulk} = \frac{P_{rad,bulk}}{P_{tot}}$;

To understand their impact on the WEST performances, H_{WEST} is plotted as a function of the total power and coloured by the different quantities. The first thing to notice is that WEST's discharges seem to be split into two branches, one above 1 and the other below one. The first one has good confinement and high T_e, it is named hot branch, the second has a lower confinement and a lower T_e, we call it cold branch (see figure 4.6a).

Looking figures 4.6 and 4.7, it is possible to notice that the hot branch is characterized by a high central electron temperature (figure 4.6a), temperature peaking factor (figure 4.6b), internal inductance (figure 4.6c), neutron flux (figure 4.6e), X point distance (figure 4.7d), and a low radiation peaking (figure 4.6d), q_{axis} (figure 4.6f), elongation (figure 4.7b), ROG (figure 4.7c) and $f_{rad,bulk}$ (figure 4.7f). The latter does not give us an indication of the difference between hot and cold branch as in the cold branch there are both plateaus with low and with high radiation. An hypothesis could be that cold branch has low confinement, therefore medium and low Z impurities are not well confined and this can translate into an overall lower bulk radiated fraction. Nothing sure can be said about the edge electron density (figure 4.7a) and the f_{rad} (figure 4.7e), as a clear distinction does not appear.

What is interesting is the ROG impact on WEST performances (figure 4.8). It seems that a lower radial outer gap leads to hotter plasmas. Therefore it is deeper analysed. It is plotted as a function of the electron density at $\rho = 1$ coloured by H_{WEST} (figure 4.8a) and T_e peaking (figure 4.8b) and as a function of the elongation coloured by T_e peaking (figure 4.8c). The ROG is well correlated with both quantities, moreover it seems that hot plasmas can be obtained with a low ROG and low elongation that seems to lead to low edge electron density. Therefore, we can say that in WEST we see a correlation between ROG and density at the edge. However, this could be a consequence of optimising the coupling between plasma and RF heating, which causes a higher density at the edge in general. More in-depth studies of this correlation have

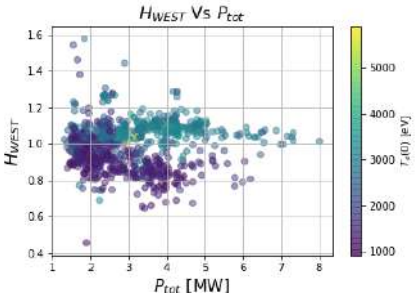

(a) plateaus coloured by $T_e(0)$.

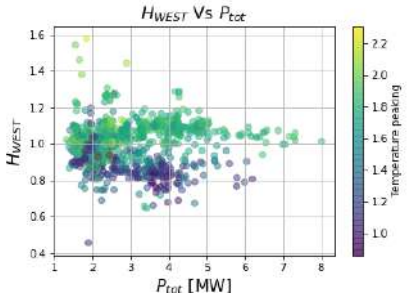

(b) plateaus coloured by $T_{peaking}$.

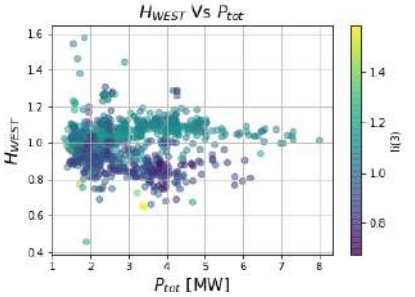

(c) plateaus coloured by internal inductance.

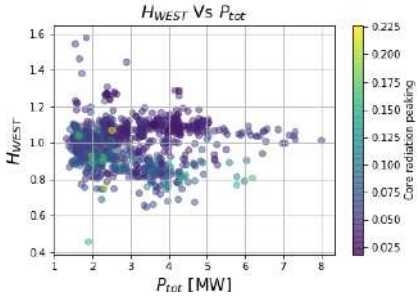

(d) plateaus coloured by core radiation peaking.

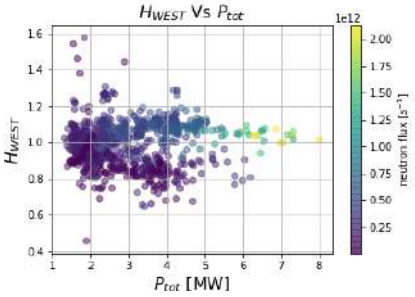

(e) plateaus coloured by neutron flux.

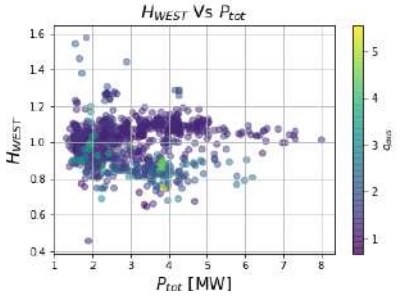

(f) plateaus coloured by q_{axis}

Figure 4.6 – H_{WEST} factor as a function of P_{tot}.

not been carried out.

Since the temperature is a good indicator of good and bad confinement states, another way to see the two clusters is to plot the central electron temperature as a function of the total power divided by the volume electron density. In this way it is possible to better visualize the hot and the cold branches that coexist in WEST. In this case, the database is filtered, we take into account only pulses with 0.5MA of plasma current.

As shown in figure 4.9, the hot branch is characterized by a central electron temperature higher than 2 keV, a higher internal inductance (l_i) and neutron flux. While, the cold one features a temperature around 1.5 keV, low l_i and neutron fluxes.

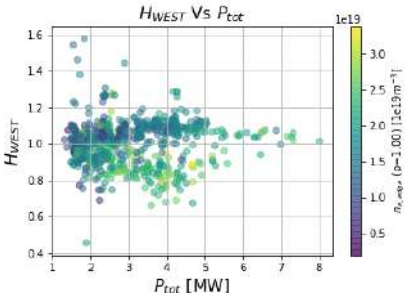

(a) plateaus coloured by $n_{e,edge}$.

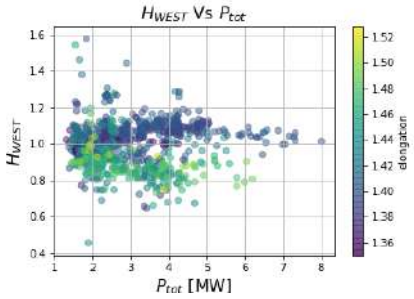

(b) plateaus coloured by elongation.

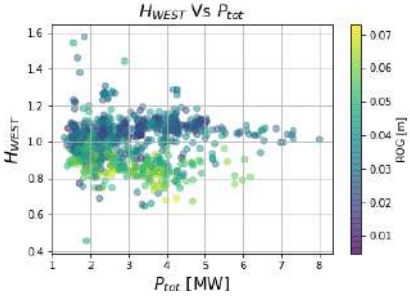

(c) plateaus coloured by ROG

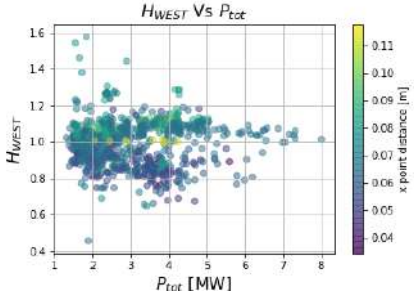

(d) plateaus coloured by X point distance.

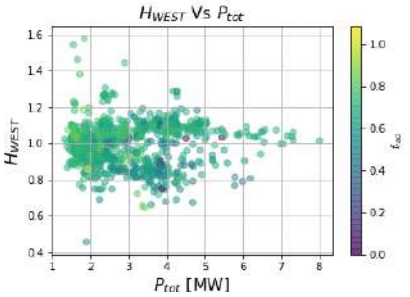

(e) plateaus coloured by f_{rad}.

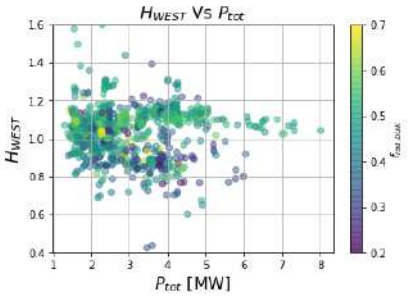

(f) plateaus coloured by $f_{rad,bulk}$

Figure 4.7 – H_{WEST} factor as a function of P_{tot}.

As expected, peaked $T_e(0)$ leads to a more peaked current profile, in presence of LHCD the absorption is improved in hotter plasmas [92] and this leads to a higher li. Another example is reported in the figure 4.9b in which the tungsten density peaking is used as colorbar. It is defined as the ratio between the tungsten density in the layer 0 and the layer 1 (from bolometry inversion). Overall the W profile is rather flat with a core peaking varying from 0.5 to 2.5. The highest values being obtained on the cold branch.

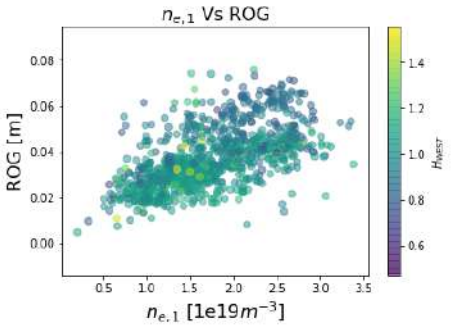

(a) ROG as a function of edge density coloured by H_{WEST}.

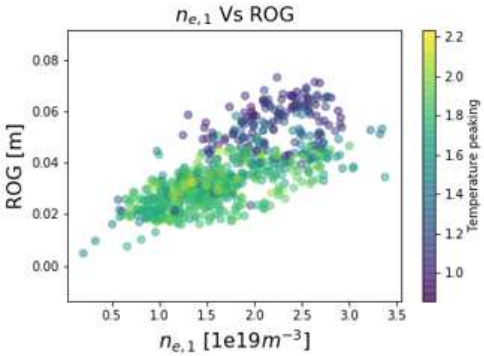

(b) ROG as a function of edge density coloured by T_e peaking.

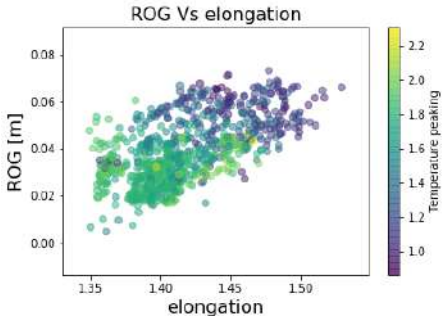

(c) ROG as a function of elongation coloured T_e peaking.

Figure 4.8 – The dependencies of ROG with respect to the edge density and the plasma elongation.

4.3.2 General overview of power density and density profiles

One explanation for why there are good and bad confinement state plateaus could be a different profile of radiated power density. An overview of this quantity is obtained dividing the power density radiated into the layer 0 taken from the inverse of bolometry by all the other layers. The last layer is not taken into account since it corresponds to the scrape of layer (SOL). The values of Ψ that correspond to the end of each layer are 0, 0.05, 0.2, 0.4, 0.6 and 0.8.
The H_{WEST} factor as a function of P_{tot} is coloured by each power density radiated fraction corresponding to each layer. As shown in figure 4.10, two possible radiated power density profiles can be noticed.
In the first one, the core radiation peaking is constant and close to 1 for the first four layers and then it increases in the last layer. In the second case, the core radiation peaking has two peaks, one in the centre and the other in the edge. It seems that only with profiles like the first case it is possible to obtain an H factor greater than 1, i.e. a good confinement plateau.

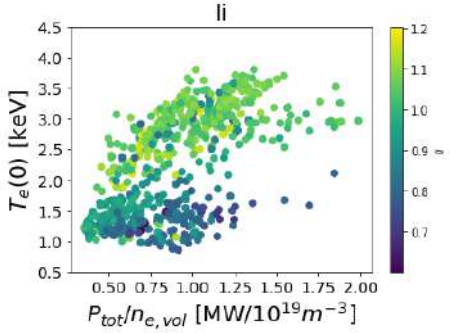

(a) Central electron temperature as function of the total power divided by the volume electron density and coloured by the internal inductance (li).

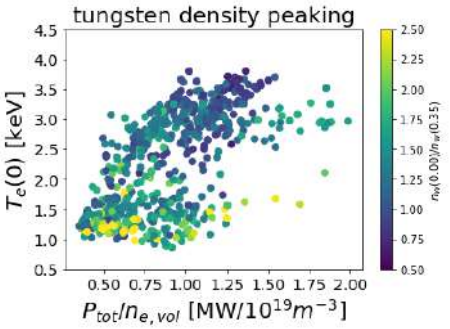

(b) Central electron temperature as function of the total power divided by the volume electron density and coloured by the tungsten density peaking.

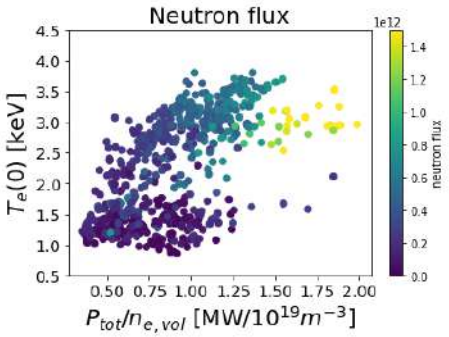

(c) Central electron temperature as function of the total power divided by the volume electron density and coloured by the neutron flux.

Figure 4.9 – Hot and cold branch coexist in WEST operation and the hot branch is linked with a high li, in the cold branch a tungsten accumulation in the core is observed and a lower neutron flux.

This observation is confirmed by looking the emission profiles computed by the inversion of bolometry. Two pulses are chosen, number 55199 and 58893. The first one has a plateau between t=8.05 s and t=9.35 s with an H_{WEST} factor equal to 1.05 and it is identified as hot plateau. The other one has a plateau between t=8.7 s and t=9.3 s with an H_{WEST} of 0.89, in the cold branch. In both cases the emission profile at the beginning, at the middle and at the end of the plateau are plotted. In the case of the hot plateau, the profiles are flat up to Ψ=0.5, then become hollow and increase at the end (figure 4.11a). In the case of the cold plateau, the profiles have two peaks, at the center and at the edge (figure 4.11b).

The same analysis is carried out for the density profile. In the database there are the measurements of the electron density at ρ=0, 0.2, 0.4, 0.6 and 0.8. Therefore a density

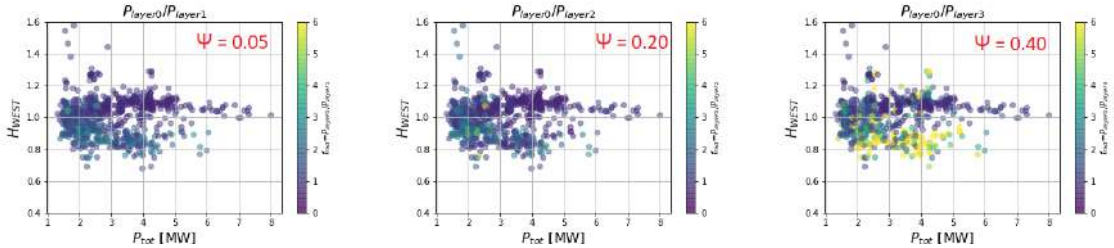

(a) Power density radiated fraction in layer 1.

(b) Power density radiated fraction in layer 2.

(c) Power density radiated fraction in layer 3.

(d) Power density radiated fraction in layer 4.

(e) Power density radiated fraction in layer 5.

Figure 4.10 – H_{WEST} as a function of P_{tot} coloured by the power density radiated fraction into each layer.

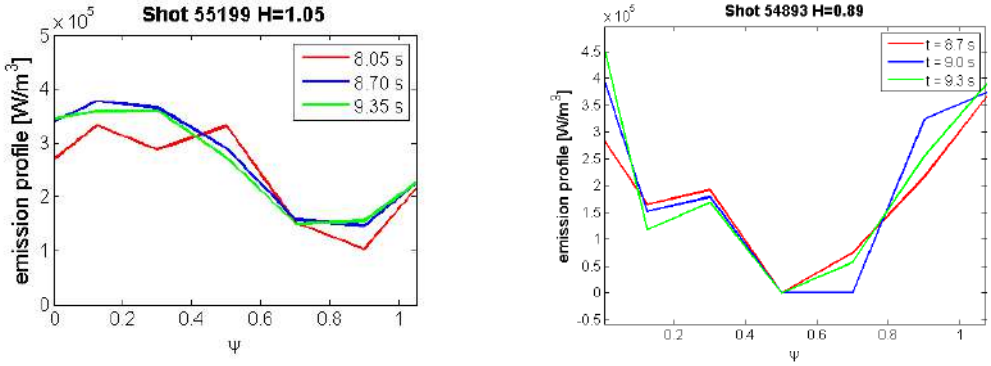

(a) Emission profiles for the stable plateau belonging to pulse 55199.

(b) Emission profiles for the degraded plateau belonging to pulse 54893.

Figure 4.11 – Emission profiles at the beginning, at the middle and at the end of stable and degraded plateau.

peaking factor is defined dividing the density at the centre of the plasma by the other values. For this quantity, the higher the density peaking, the better the confinement (figure 4.12).

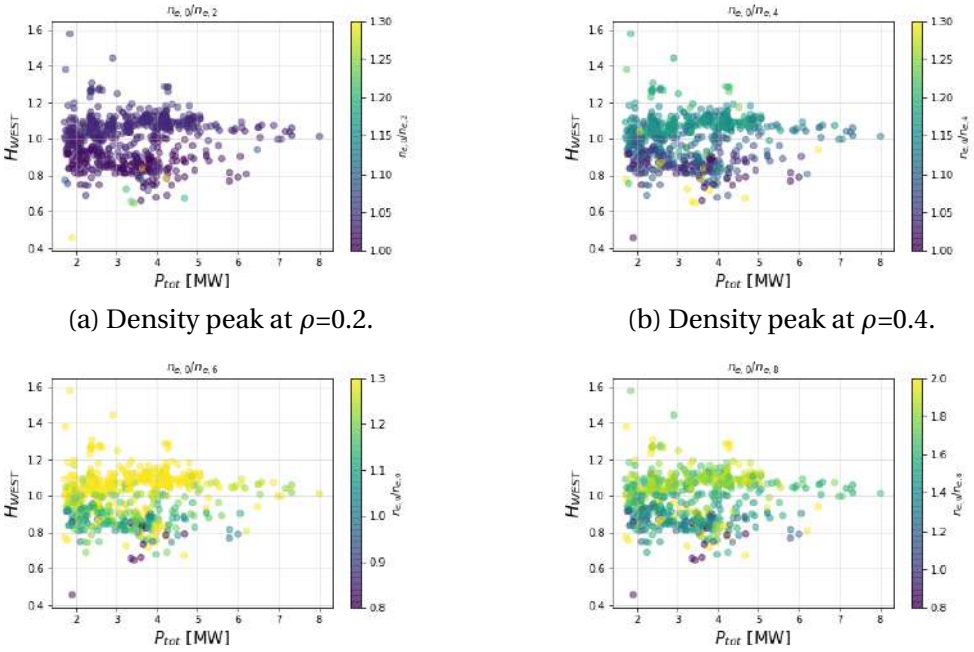

(a) Density peak at ρ=0.2.

(b) Density peak at ρ=0.4.

(c) Density peak at ρ=0.6.

(d) Density peak at ρ=0.8.

Figure 4.12 – H_{WEST} as a function of P_{tot} coloured by the density peak at different values of ρ.

4.3.3 Database analyses of abrupt collapse of central T_e

Deeper analysis of the database has shown that some discharges in the hot branch go to the cold one at given $P_{tot}/n_{e,vol}$. These pulses have in common a rapid collapse of the central electron temperature in about 0.5s. Some of these are followed by a disruption, others continue in a low confinement-time state.

A simple model to detect the collapse in WEST database is developed in order to quantify the percentage of these pulses with respect to the whole discharges. The time evolution of $T_e(0)$ over the flattop is fitted by the following formula as representing a collapsing $T_e(0)$:

$$T_e(0) = -e^{a+bt} + c \tag{4.3}$$

The plateau is identified as:

— **Unstable**: if the central temperature can be fit by the formula (4.3) with $a < 0$ for a negative concavity, $b > 1$ and $\frac{a}{b} > -40$ to avoid to take into account the plateaus in which the pulse ends (figure 4.13a). Or if it fits a linear function with a slope at least < -830 to avoid identifying a fast termination of the discharge as a collapse. This is because many collapses do not happen during the identified plateaus (figure 4.13b). In the figure 4.13 two collapses fit by an exponential function

(pulse 55025 4.13a) and a linear function (pulse 54369 4.13b) are shown.

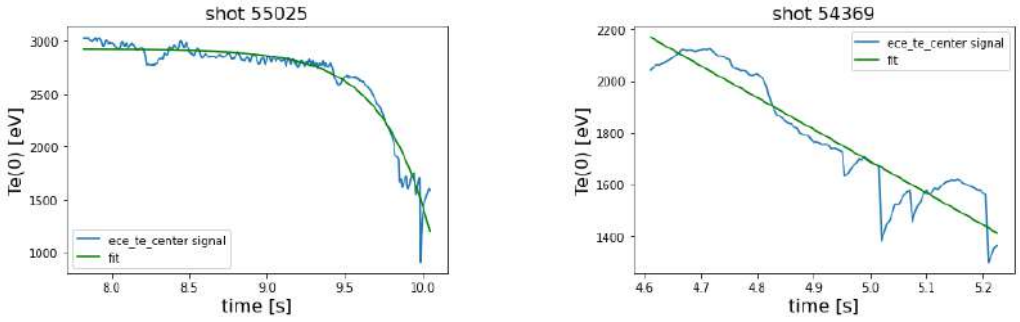

(a) Pulse 55025, the collapse is fit by an exponential function.

(b) Pulse 54369, the collapse is fit by a linear function.

Figure 4.13 – Example of two discharges in which radiative collapse has been identified.

— **Degraded**: if an unstable plateau is followed by a plateau with a H_{WEST} factor less than unity;

— **Stable**: if a collapse is not identified and if the plateau has an H_{WEST} factor greater than unity.

We have found that 25% of the discharges into the hot branch eventually collapse. An example, in figure 4.14a some discharges belonging to the hot (blue lines) and cold (green lines) branch with the same injected power (1MW) at the same time (4.2-4.5s) are filtered and plotted. As can be seen, some of the discharges with an initial temperature of about 3keV eventually collapse (orange lines). In figures 4.14b and 4.14c the line averaged electron density and the P_{LH} as a function of time are plotted for the same discharges. We notice that cold branch plasmas are characterised by high line averaged densities (around $4.5 \cdot 10^{19} m^{-3}$). The collapses occur mostly around 6s. At first sight, there is not a significant difference in density prior to the collapse between collapsing and hot branch pulses (orange and blue lines). At the same time, from 4.5 s to 6 s the heating level is similar.

The profile of the power injected during the discharge is computed for each time step. Thanks to the following formula it is possible to compute the integral of a quantity over the plasma volume:

$$A_V = \rho_{tor} \int_0^1 V' \langle A \rangle dx \tag{4.4}$$

Where A is the quantity to integrate, the brackets mean a flux averaged quantity, ρ_{tor} is the normalized radial coordinate, $V' = \frac{dV}{d\rho}$ is the derivative of the plasma volume V

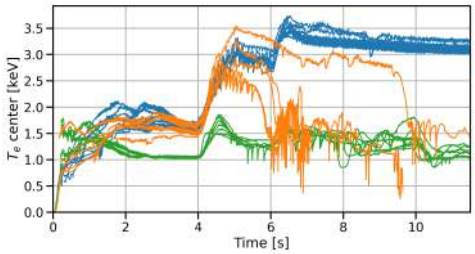

(a) Central electron temperature as a function of time.

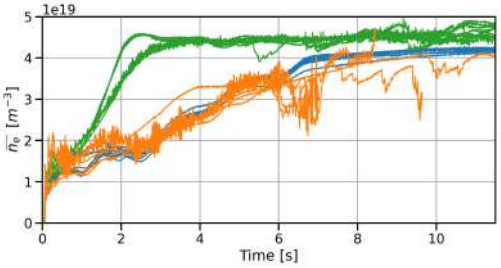

(b) Line averaged electron density as a function of time.

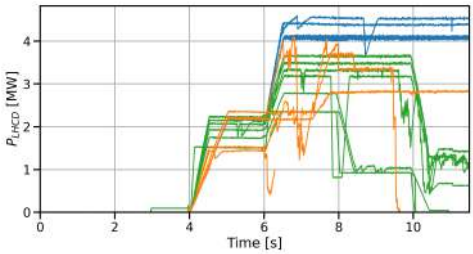

(c) P_{LH} injected power as a function of time.

Figure 4.14 – Discharges characterized by the same injected power at the same time (1MW, at 4.2-4.5s). In blue discharges in the hot branch, in orange the collapsing discharges and in green the discharges in the cold branch.

with respect to ρ_{tor} and dx the unit element in the direction of the normalised radius. The integration is computed for each time steps up to $\rho_{tor} = 0.4$ since the quantity of interest is the power injected in the first plasma layer. Since the function that computes the profile of the injected power is affected by uncertainty especially in the center of the plasma, the first layer is set to $\rho_{tor} = 0.4$ (figure 4.15). Then, the central radiated fraction is computed as the power radiated in the first layer divided the power injected in the same layer.

In figure 4.16a the central radiated fraction is plotted as a function of the central electron temperature and coloured by the plateaus classification. It is possible to notice that all the unstable plateaus are located in the region between 1.5 keV and 3 keV. The majority of the stable plateaus are in the high temperature region, while the degraded plateaus are in the low temperature region.

Figure 4.16b shows the ADAS 50 database for tungsten cooling factor as function of electron temperature, the unstable region is located in the range of 1.5-3 keV in which the cooling factor increases as the temperature decreases. If $T_e(0)$ decreases, radiation increases and it leads to a further $T_e(0)$ decrease and thus to an instability. If temperature decreases slowly due for instance to increasing core density or decreasing core power absorption, this slow dynamics can at a certain point cross the instability

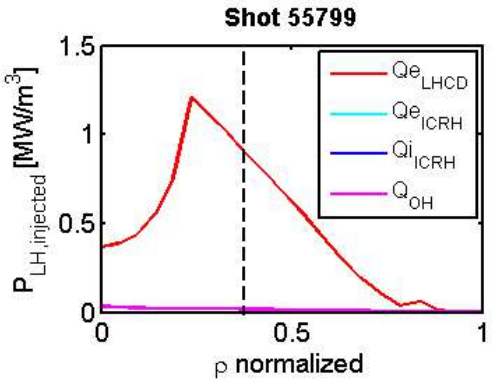

Figure 4.15 – Profile of the power injected for pulse 55799 at t=5.1s. The dashed line correspond to the upper integration limit.

condition and lead to a temperature collapse.

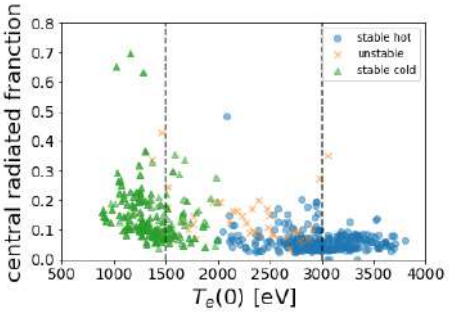

(a) The central radiated fraction as a function of the central electron temperature and coloured by the plateaus' classification. The unstable plateaus are in the region between 1.5-3 keV; the stable plateaus are in the high temperature region, while the degraded ones are in the low temperature region.

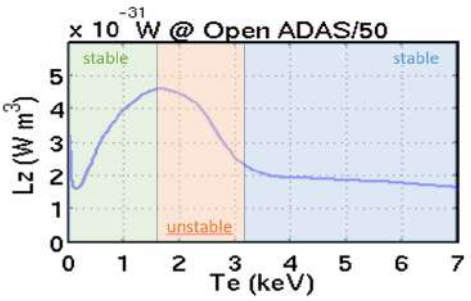

(b) Tungsten cooling factor taken from ADAS database. The unstable region is between 1.5-3 keV where the cooling factor increases as the temperature decreases.

Figure 4.16 – Unstable plateaus are consistent with the tungsten cooling factor unstable range.

The increase in cooling factor is not the only player leading to a collapse. As it will be shown in the next chapter the density increase accompanied by a reduction in the central T_e plays a role on LHCD central heating absorption and tungsten transport. The change in tungsten transport can lead to the accumulation of this impurity in the plasma core.

4.4 Time evolution description of two collapsing pulses

Since reaching plasmas with enhanced stability is fundamental to obtain high tokamak performances, the core radiative collapse is studied in greater detail.

The pulse 55025 goes from the hot to the cold branches as shown in figure 4.17a. It means that a good confinement plateau, but unstable, is followed by a degraded one. It was chosen as an example of a collapse with LHCD power injected through both antennas and because it has a high density. In figure 4.17b the time traces of n_e, I_p, T_e, P_{tot} and P_{LH} are shown.

The LHCD system is composed of two antennas that can inject respectively 4 MW of power for LH1 launcher and 3 MW of power for LH2. Both launchers are actively cooled and are equipped with protection limiters in carbon with a W coating. For the 55025 pulse considered, the plasma current is 0.5MA; the toroidal magnetic field is 3.6T; the total injected power is 2.8MW injected by the two LHCD antennas (P_{LH1} = 1.44MW and P_{LH2} = 1.37MW). The electron density slowly increases during whole the discharge. The central electron temperature collapses at t = 9.5s.

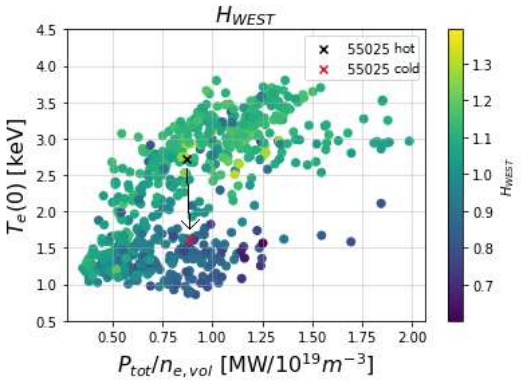

(a) $T_e(0)$ as a function of $P_{tot}/n_{e,vol}$. The crosses represent the plateaus of the 55025 discharge. It goes from a good to a bad confinement state.

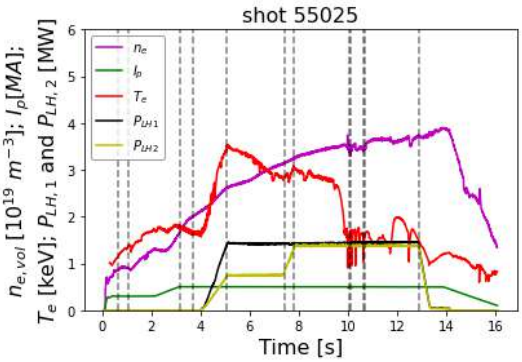

(b) Description of the main parameters of the pulse: The plasma current is 0.5MA; the toroidal magnetic field is 3.6T; the total power is 2.8MW injected by two LH antennas (LH1 = 1.44MW and LH2 = 1.37MW). The electron density slowly increases during all the discharge. The central electron temperature collapse at t = 9.5s.

Figure 4.17 – Description of pulse 55025.

In figure 4.18a the time traces of the electron temperatures at $\rho = 0$, $\rho = 0.2$ and $\rho = 0.4$ are plotted. During the unstable plateau a first slow decrease of central temperature is observed, at the same time volume-averaged electron density increases, then, a fast collapse occurs and, at the end, the plasma goes in a degraded confinement

state with a central temperature around 1.5 keV. The same trend is observed at $\rho = 0.2$. Already at $\rho = 0.4$ the collapse is less evident, especially in the fast phase, where the temperature difference (before and after the collapse) does not exceed 200 eV. This means that the radiative collapse is localised mainly at the plasma center. Also a small shift in time for the fast collapse at different ρ is noticeable.

Potential causes for the central T_e collapse are: the reduction of central LHCD heating and the increase of core radiation due to increase in cooling rate and/or tungsten density. In figure 4.18b, the signal of the hard X-ray central channel for the energy band 60-80 keV as a signature of LHCD absorption (see section 2.2.3) and the estimation of the tungsten central density from bolometry inversion are plotted (see section 2.2.1). The latter is constant during the first part of the collapse and then starts to increase very quickly until it reaches a peak at the point where the temperature is at its lowest. This suggests a tungsten accumulation in the center of the plasma. The LHCD power multi-pass absorption is known to shift further off-axis as the $T_e(0)$ decreases [92]. The LHCD power deposition is maximized near the intersection between the Landau damping limit and the upper caustic ($n_{||+} = \frac{n_{||0}}{1+(\frac{r}{R_0 q})} \times (\frac{-\epsilon_{||}}{\epsilon_\perp})^{\frac{1}{2}}$), whose intersection determines the location of the power deposition. When the temperature increases the intersection moves inward, leading to larger on axis absorption. A modification of LHCD absorption is observed by the HXR signal in the figure 4.18b.

The radiative collapse has an impact also on the plasma shape. In figure 4.18c, the radial outer gap (distance in outboard mid-plane between plasma and the closest antenna) is plotted. It is constant during the first phase of the collapse, then it increases rapidly during the fast $T_e(0)$ drop. This can be explained by the fact that $\beta_p + l_i/2$ changes rapidly, therefore the plasma boundary is modified (these two quantities are linked via Grad-Shafranov equation [93]). We observe that the plasma shrinks, elongation increases, therefore the ROG follows the $\beta_p + l_i/2$ dynamics and changes at the same speed. Lastly, the internal inductance is analysed since it is related to the current density profile. The internal inductance is computed as the ratio between the magnetic energy stored in the poloidal field and the square of the plasma current that is the integral of the toroidal current density on the plasma cross section. l_i is constant and then it decreases during the fast collapse, indicating a flattening of the current profile.

As collapsing plateaus affects 25% of the hot branch in WEST C4 campaign, the same type of analysis was performed for a second pulse, 54802. In contrast to the previous discharge, this was selected as an example of a pulse with only one antenna used and lower density, to ensure that the discharge behaviour during collapse is the same. It shows an increase of electron density before the collapse. The collapse is not followed by a plateau in a degraded confinement state but the discharge ends with a disruption, as shown in figure 4.19. Also in this case, a first slow decrease of central temperature is observed together with a slow increase of n_e, then, a fast collapse occurs and, at the

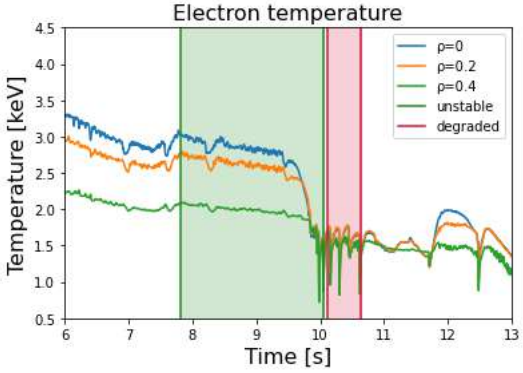

(a) Electron temperature time evolution at $\rho = 0$, $\rho = 0.2$ and $\rho = 0.4$. The central temperature collapses during a good confinement plateau (green region) followed by a degraded confinement plateau characterized by a temperature of about 1.5 keV (red region).

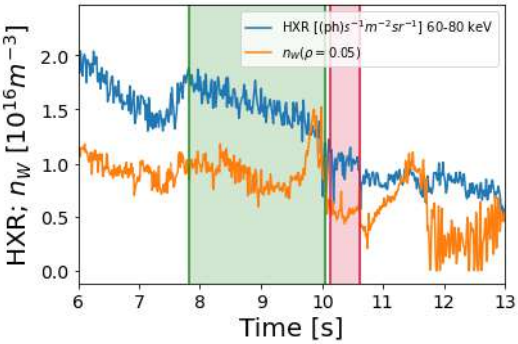

(b) Signal of the hard X-ray central channel (number 20) for the energy band 60-80 keV and the estimation of the tungsten central density. The first follows the temperature evolution; the second increases during the fast part of the collapse.

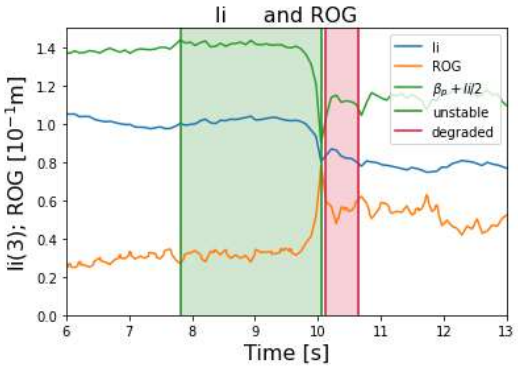

(c) Radial outer gap (ROG) increases rapidly during the fast phase, while the li decreases. $\beta_p + li/2$ is plotted to explain the equilibrium change, see on the ROG variation.

Figure 4.18 – Pulse 55025. The green region denotes the good confinement plateau, while the red region is the degraded confinement plateau.

end, the plasma reaches a temperature close to 1.5 keV. The same trend is observed at $\rho = 0.2$, but at $\rho = 0.4$, the T_e reduction is again much smaller. The same dynamics as explained previously for pulse 55025 are observed (figure 4.20).

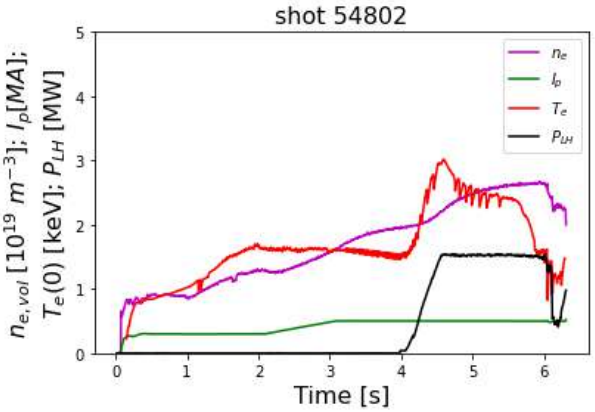

Figure 4.19 – Description of the main parameters of the pulse: The plasma current is 0.5MA; the toroidal magnetic field is 3.6T; the total power is 1.7MW injected by one LH antennas. The electron density slowly increases during all the discharge. The central electron temperature collapse at t = 5.5s.

To conclude, we observe that the main characteristics of the collapse are a drift toward a higher density, a central tungsten peaking and the change of LHCD power absorption at the plasma core.

To identify the causality chain, the modelling of the collapsing phase is necessary. It is important to find out if the assumptions made allow one to simulate the temperature measured in the experiments. Secondly, modelling contributes to a better understanding of the key players involved in the electron temperature collapse. The modelling of these two pulses is presented in chapter 5.

4.5 The 0D model of the collapse

A simple model has been developed by N. Fedorczak (see WEST task force meeting 18/06/2020) for the core temperature collapse. In the following we detail this approach.

Considering a fixed central volume and assuming that electron, ion and impurity density are constant, a given heating power is deposited in this volume (P_{IN}). A fraction of this power (Q) is transported outside of this volume by turbulence and it is a function of the central temperature ($Q = \Gamma T^{\alpha}$). Γ is a transport parameter considered constant and α is a sensitivity parameter equal to 2.5 because a Gyro-bohm transport is considered. Another fraction of the input power is radiated as a function of the central temperature ($P_{rad} = RT^{\beta}$). Where R is a constant radiation parameter and

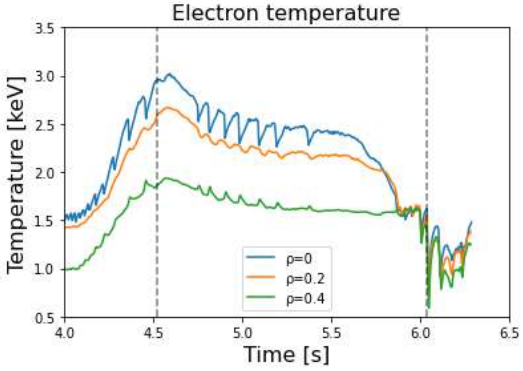

(a) Electron temperature time behaviour at $\rho = 0$, $\rho = 0.2$ and $\rho = 0.4$. The central temperature collapses during a good confinement plateau (green region) followed by a degraded confinement plateau characterized by a temperature of about 1.5 keV (red region).

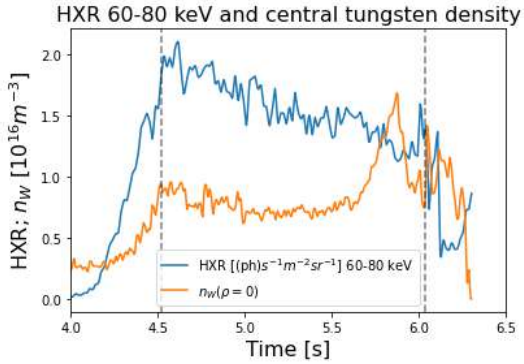

(b) Signal of the hard X-ray central channel (number 20) for the energy band 60-80 keV and the estimation of the tungsten central density. The first follows the temperature behaviour; the second increases during the fast part of the collapse.

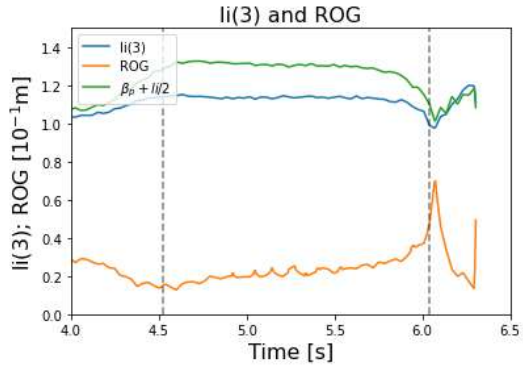

(c) The radial outer gap increases rapidly during the fast phase, while the li(3) decreases. $\beta_p + li/2$ is plotted to explain the equilibrium change.

Figure 4.20 – Pulse 54802. The vertical lines indicate the limits of the unstable plateau identified for the discharge.

β is the radiation sensitivity parameter and it depends on the type of impurity and the temperature range. Considering a simple conservation law for the temperature dynamics:

$$\partial_t T = P_{IN} - P_{rad} - Q = P_{IN} - RT^{\beta} - \Gamma T^{\alpha} \tag{4.5}$$

For a given P_{IN}, R and Γ parameters, it is assumed that a stationary point T_0 exists. Therefore:

$$RT_0^{\beta} + \Gamma T_0^{\alpha} = P_{IN} \tag{4.6}$$

It exists if $P_{rad} < P_{IN}$. Considering stability of variation around this steady-state: $T = T_0 + \delta T$.

$$\partial_t \delta T = P_{IN} - R(T_0 + \delta T)^{\beta} - \Gamma(T_0 + \delta T)^{\alpha} = 0 + \delta T(-\alpha\Gamma T_0^{\alpha-1} - \beta R T_0^{\beta-1}) \tag{4.7}$$

In the limit of $\delta T \ll T_0$. Which can be rewritten as:

$$\partial_t \delta T = -\delta T \frac{\alpha}{T_0}(-\frac{\alpha-\beta}{\alpha} P_{rad,0} + P_{IN}) \text{with} P_{rad,0} \equiv RT_0^{\beta} \tag{4.8}$$

Therefore, the steady-state solution is stable only if $\frac{\alpha-\beta}{\alpha} P_{rad,0} < P_{IN}$.
In the low temperature regime of tungsten radiation ($\beta > 0$) stability is always satisfied if the stationary point exists ($P_{rad} < P_{IN}$). While in the high temperature regime ($\beta < 0$) stability requires $P_{rad,0} < \frac{\alpha}{\alpha-\beta} P_{IN}$.
Assuming a Gyro-Bohm transport ($\alpha = 2.5$) and $\beta \approx -1$, stability become $P_{rad,0} < \frac{5}{7} P_{IN}$ and it requires that $T_0 > \frac{7R}{5P_{IN}}$.
Following this simple model, at high core temperature, stable stationary conditions with tungsten radiation can exist if transport carries a minimum fraction of the input power. On the other hand, if radiation rises slowly in the core, or if the temperature decreases slowly due to the increase of the core density (or the decrease of the core power absorption), this slow dynamics can still be in the stable regime, but at a certain point, it can cross the instability condition and lead to a temperature collapse.
A stable area (figure 4.21) can be defined assuming a Gyro-Bohm transport and a tungsten radiation fraction that depends on the temperature:

$$\partial_t T = P_{IN} - P_{rad}(T) - \Gamma T^{\alpha} \tag{4.9}$$

Comparing to figure 4.16a, also in this case an unstable region is found in the tem-

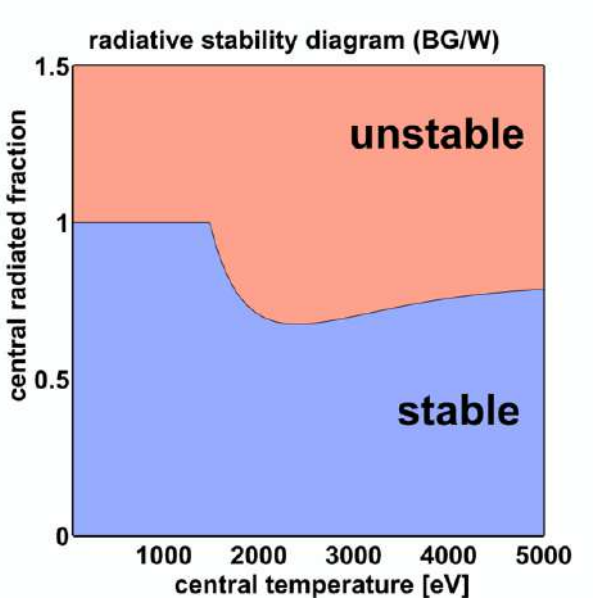

Figure 4.21 – Stability area computed using the simple model of collapse.

perature range of 1.5 keV and 3 keV. This means that in this range a central radiated fraction lower than 1 could lead to a temperature collapse.

The central radiated fraction is computed as $f_{rad} = \frac{P_{rad}}{P_{IN}}$.
As example, two simulations are done. In the first one the stable starting initial condition is $T = 2800eV$ and $f_{rad} = 0.5$. A slow ramp up of the effective tungsten concentration is assumed. The system transits from a stable regime, through unstable regime, into a deteriorated stable condition, with only a few percent increase of tungsten concentration. The second simulation starts from the same radiated fraction but lower initial temperature. The system stays in a stable regime and ends up in a better condition for the same tungsten concentration (figure 4.22).

Interestingly this dynamic is much less frequent during ICRH heating only, even though the total radiation is high. It seems that a turbulent transport acts as a stabilizing mechanism maintaining the central temperature with respect to the radiation.
This model allows a better understanding of the collapse dynamics but, as we will see in the next chapter, other phenomena as LHCD core absorption and tungsten accumulation play a major role in the observed collapse evolution.

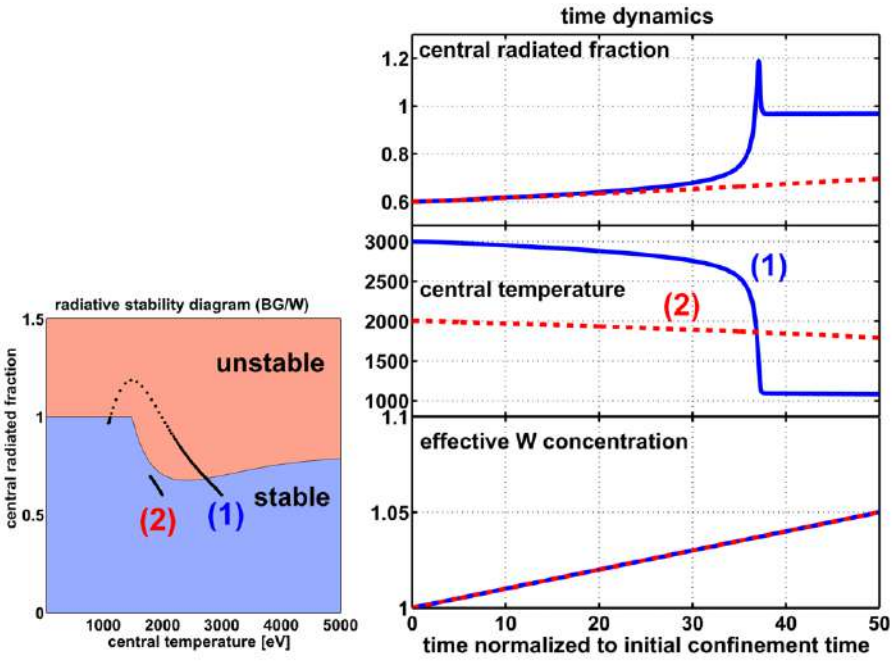

Figure 4.22 – Time dynamics of two simulation made using the simple model.

4.6 Possible solutions to avoid the collapse

4.6.1 Distance from boronization

During the whole C4 campaign boron has been injected, since boronization provides considerably improved plasma conditions. It is an important tool to control tungsten sources and allow reliable operation at low collisionality, as the results of several experiments show. This was done roughly at a frequency of one boronization per week. To analyze the effect of this technique, the pulses that occurred after each boronization were identified. The pulses number are: 53453, 54288, 54403, 54502, 54596, 54719, 54881, 55000, 55138, 55499, 55548, 55747, 55795.
Each discharge was characterized by its distance from boronization, i.e. how many pulses had been done since the last boronization. Then the ohmic discharges have been separated from the L-mode discharges. The effective resistivity, Z_{eff}, ($Z_{eff} = \frac{\sum n_j Z_j^2}{\sum n_j Z_j}$ where n_j is the density of different ion species and Z_j the charge particles) is analysed as function of the distance from boronization (figure 4.23).

It seems that there is no difference between the L-mode and the ohmic discharges. In both cases the minimum Z_{eff} value is above 1 and it increases when moving away from boronization.

To better see the effect of boronization on plasma performance, only L-mode pulses are considered. Z_{eff} is now plotted as a function of the pulse number. The dot-

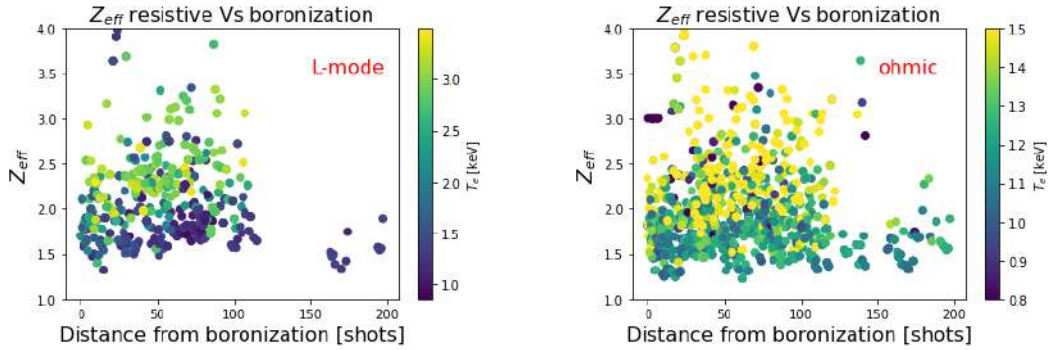

(a) Z_{eff} as a function of the distance from boronization for the L-mode pulses.

(b) Z_{eff} as a function of the distance from boronization for the ohmic pulses.

Figure 4.23 – Z_{eff} as a function of the distance from boronization.

ted black lines in the figure 4.24 indicate the pulse that occurred immediately after boronization. Z_{eff} remains low for a few discharges after boronization, after which it increases rapidly and then returns to around 2.2 during the next boronization. To conclude, the boronization seems to have a beneficial effect on the impurities in the plasma, but a short effect. After a few pulses Z_{eff} increases to a saturation level around 2.5.

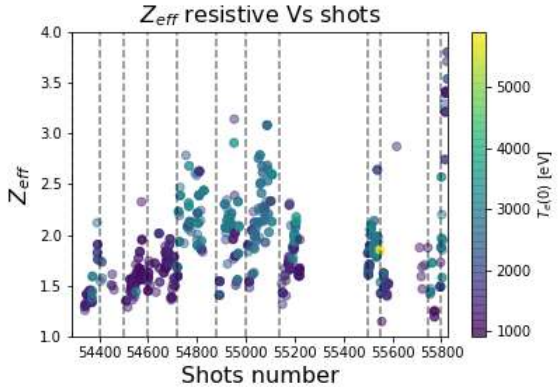

Figure 4.24 – Z_{eff} as a function of the discharge number. The dotted black lines indicate the pulses that occurred immediately after boronization.

Also the impact on the power radiated in the core is analysed. In this case the fraction of the radiated power in the bulk is computed as the power radiated in the bulk divided by the total power. As can be seen in figure 4.25, the effect of the boronization on the power radiated in the core is very short, already after 50 discharges the fraction of radiated power rises over 50%. This means that its effect lasts about two days of operation.

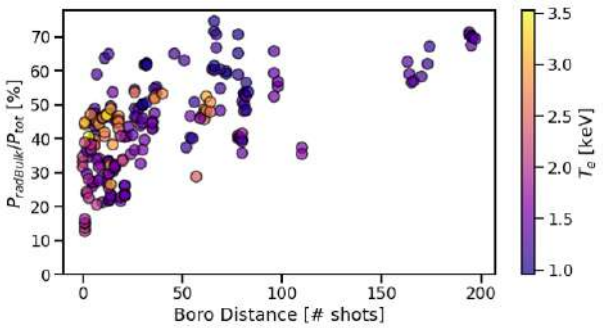

Figure 4.25 – Power radiated in the bulk as distance of boronization. Its effect lasts about 50 discharges.

Regarding the impact on the radiative collapse, the plateaus in which the collapse has been identified are plotted as a function of the distance of boronization. As it is possible to see in figure 4.26, no collapse occurs using only LHCD heating before 20 discharges from boronization. Regarding ICRH discharges very close to boronization, these have a very high tungsten density. We believe that this is due to ICRH induced sputtering on W antenna protections. With high levels of W sources a collapse can more easily occur.

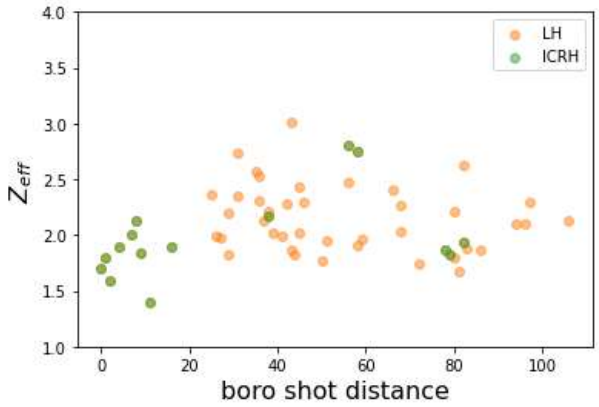

Figure 4.26 – Z_{eff} as function of the distance from boronization for the collapsing plateaus coloured by different heating systems.

4.6.2 Benefit of ICRH heating

Due to the difficulty in controlling the position of the injected power via LHCD because of the multi-pass absorption and the LHCD dependency on the electron temperature, another heating system, as ICRH, is suitable. This system allows a better control of the power deposition location.
It is used successfully in today's experiments as shown in ASDEX Upgrade H-mode

plasmas [94], in JET hybrid plasmas [95] and is relevant for the next step devices.
Despite possible benefits, in tokamaks with high-Z first wall materials it is of great importance to make ICRF antenna operation compatible with neighbouring wall structures, as RF induced sheaths may lead to significant sputtering and self-sputtering effects as shown in different ASDEX Upgrade experiments [96].

As can be seen in figure 4.27, where the fraction of radiated power in layer 0 is plotted as a function of tungsten peaking, there is no clear benefit in using ICRH alone or coupled with LHCD. In fact, no matter what heating scheme is used, the same radiation values and respective tungsten accumulations occur. This is probably due to a not well optimized coupling between the antenna and the plasma.

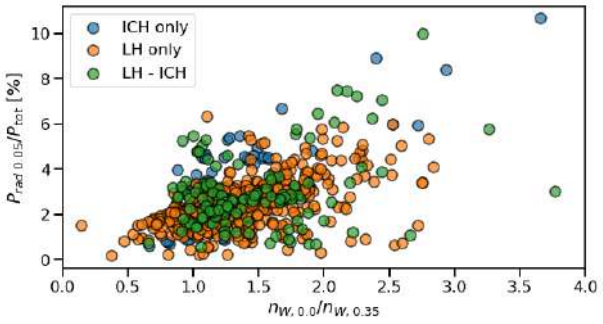

Figure 4.27 – Power radiated in layer 0 as a function of central tungsten peaking coloured by ICH only, LH only and LH-ICH. No evident benefit is noticed in WEST ICRH operation.

However, some discharges in which the radiative collapse is saved using ICRH injection have been found, such as pulses 55194 or 54719.
In figure 4.28 the time history of pulse 55194 is shown. The electron density slowly increases (purple line) during all the discharge. The temperature reaches 3keV when the LHCD is injected (green). After that, a slow temperature decrease followed by a collapse in 0.4s is observed (red line). At the same time, also a central tungsten accumulation is noticed (yellow). At this point, ICRH is (blue line) injected and the discharge seems to be partially stabilized .

4.6.3 Conclusion of the chapter

Thanks to the bolometry inversion it is possible to estimate the tungsten profiles for $T_e > 1keV$ as well as the power radiated fraction in the core.
It has been seen that the RF heating has no impact on the radiated power in the core since the discharges in LHCD only and in ICRH only overlap.

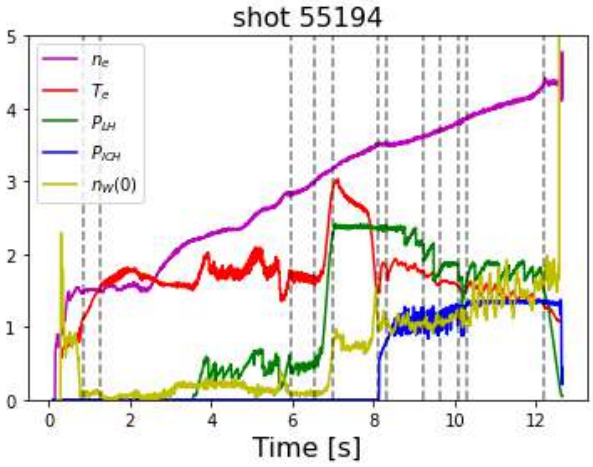

Figure 4.28 – pulse 55194. Electron density in red line, electron temperature in red, LH in green, ICRH in blue and the central tungsten density in yellow. The pulse is saved injecting ICRH.

The H_{WEST} has been computed as the ratio between the real energy confinement time and the one computed from the WEST data scaling. This quantity has been used to quantify the quality of the confinement and two clusters of points are identified. The hot branch is characterized by a high central electron temperature, internal inductance and neutron flux, while the cold one features low temperature, li and neutron flux.

It has been noticed that some discharges in the hot branch go to the cold one. This pulses have in common a rapid collapse of the central electron temperature. A simple criterion to detect the collapse is developed. We have found that 25% of the discharges in the hot branch collapse. Moreover, all the unstable plateaus are located in the region between 1.5 keV and 3keV. This is in agreement with the tungsten cooling factor unstable region, in which a decrease of the central electron temperature increases the radiation and it leads to a further temperature decrease.

In general, the time evolution of the collapse is the following. A first slow decrease of the central temperature is observed and, at the same time, the electron density increases, then a fast collapse occurs. The signal of the HXR central channel for the energy band 60-80 keV decreases, as a signature of LHCD absorption. Regarding the tungsten density, it is flat prior to the collapse and then it peaks during the fast collapse.
We conclude that potential causes for the $T_e(0)$ collapse are: the reduction of the central LHCD absorption and the increase of the core radiation due to the increase in cooling rate and tungsten density.

A 0D model of the collapse has been developed in which only an effective tungsten

concentration is assumed. The simulations show that the system transits from a stable regime into a deteriorated stable condition. This model allows a better understanding of the collapse dynamics but, as we will see in the next chapter, other phenomena as LHCD core absorption and tungsten accumulation play a major role in the observed collapse evolution.

Some solutions of the collapse have been tested. In particular the boronization and the ICRH heating system.
In the first case, is has been shown that the beneficial effect of the boronization lasts about 50 discharges, since, after that, the power radiated fraction in the bulk grows up to 50%. Moreover, no collapse occurs using only LHCD as heating before 20 discharges from boronization.
For ICRH pulses no clear conclusion can be drawn for the moment. More investigations and scenario developments are needed to better evaluate the ICRH effect on the radiative collapse.

5 Integrated modelling of two collapsing pulses

5.1 introduction of the chapter

In this section the integrated modelling framework (figure 5.1) is presented and all the steps that lead to reproduction of the radiative temperature collapse are described. The modelling framework is composed of METIS [97] for the interpretative modelling needed to prepare the simulations and RAPTOR [65] coupled with QuaLiKiz neural network [56] to predictively model the collapse thanks to computed transport coefficients. The LUKE code [98], used in stand alone, is used to determine the LHCD power absorption profile evolution.
Using this framework the pulses 55025 and 54802 are modelled. After the collapse, the first displays MHD activity and the second ends in a disruption. Fort these two pulses the collapse sequence is the same.
In both cases, a general overview of the discharge is given and, then, the two major ingredients that characterize the collapse are explained: the tungsten peaking evolution and the LHCD absorption evolution.

5.2 Modelling tools

5.2.1 METIS

METIS is used to perform an interpretative integrated modelling to verify the consistency of the data and infer some quantities that are not measured. It is a fast integrated tokamak modelling tool combining 0D scaling laws for kinetic profiles with 1D current diffusion modelling and 2D equilibria. The electron temperature and the density profiles used in METIS run are fitted from the ECE measurements and interferometry inversion (see sections 2.2.2 and 2.2.4). The shape of the ion temperature profile follows the square root of the electron pressure and is scaled to match the measured deuterium-deuterium neutron rate. The amount of tungsten and the tungsten profiles are chosen using the bolometry inversion (see section 2.2.1) and the tungsten concentration at the separatrix is adjusted to match the total radiated power. The effective charge Z_{eff} is computed from Bremsstrahlung measurement or in absence of this measurement the flux consumption during the ohmic phase combined with T_e profile from ECE measurements is used to compute the resistive Z_{eff}. Nitrogen is chosen to represent the light impurity content. Nitrogen, carbon and oxygen complete the

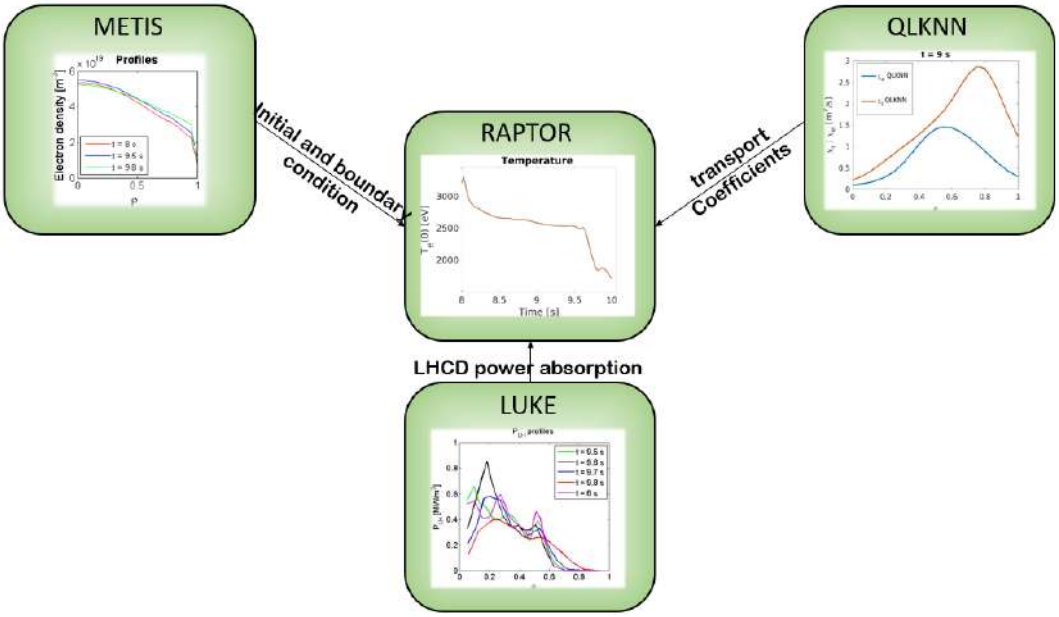

Figure 5.1 – Framework of integrated modelling. METIS is is use to set the initial and boundary conditions; QLKNN is used to compute the transport coefficients and LUKE to compute the LHCD power absorption. RAPTOR is used as transport code.

tungsten content to match the Z_{eff}. The radiated power from line emission and thermal Bremsstrahlung are computed from the cooling rates. Finally, the thermal energy content based on the ion and electron density and temperature profiles is computed and cross-validated using the energy content obtained by equilibrium reconstruction (NICE reconstruction) [97].

5.2.2 RAPTOR

RAPTOR (RApid Plasma Transport simulatOR) is a 1D transport physics code that solves the 1D transport equations for T_e, T_i, n_e and can predict the poloidal flux diffusion $\Psi(\rho, t)$ (the time evolution of the poloidal magnetic flux profile, which is modelled in normalized cylindrical coordinates by a partial differential equation referred to as the magnetic diffusion equation). It is designed for plasma control. The 2D equilibrium is not self consistently evolved but is read from a given reconstruction. More details about the code can be found in ref [65]. To predict T_e, T_i and n_e, the turbulent heat fluxes need to be predicted. QuaLiKiz Neural Network has been coupled and it is presented in the following subsection.

In the context of this work, $j(\rho, t)$, $T_e(\rho, t)$ and $T_i(\rho, t)$ are predicted from the core to $\rho = 1$, while n_e, n_i and Z_{eff} are fixed from experimental measurements and constraints including the tungsten density and the profiles. The radiated power is computed using ADAS 50 for the tungsten cooling factor. The LHCD profiles are computed using the LUKE code and modified in the very central region. More details on the

modelling can be found later in the paper. The neoclassical heat flux is not computed since there is no heat deposited on the main ions except for the collisional equipartition. Adding neoclassical ion heat fluxes would only change the T_i profile in the central part of the plasma $\rho < 0.3$, the rest being dominated by turbulence, the change in equipartition would be reduced due to low collisionality in this central region ($T_e > 1.5keV$).

5.2.3 QuaLiKiz Neural Network

The transport coefficients are computed using a Neural Network regression trained on 300 millions simulations made with the gyrokinetic quasilinear transport model QuaLiKiz in 10D, QLKNN-10D [56].
QLKNN is a surrogate model based on a database of 3×10^8 flux calculations of the quasilinear gyrokinetic transport model, QuaLiKiz [99] [100]. It calculates the heat, particle and momentum turbulent fluxes. It is demonstrated to be rapid enough to ease systematic interface with experiments. In this work we have chosen to use QLKNN since JINTRAC–QLKNN and RAPTOR–QLKNN are able to accurately reproduce JINTRAC–QuaLiKiz $T_{e,i}$ and n_e profiles, but 3–5 orders of magnitude faster. Simulations that take hours are reduced down to only a few tens of seconds. The discrepancy in the final source-driven predicted profiles between QLKNN and QuaLiKiz is on the order of 1%–15%. Therefore, the main reason for choosing this framework is computational speed.
QLKNN is trained on a large regular input parameter hyper rectangle scan to ensure the wide applicability of the obtained model, as explained in the ref. [56]. The range of the parameters covered is quite large (see the table in ref. [56]) and covers WEST operational domain, for example T_e larger than T_i. Nonetheless for $\rho > 0.95$ the normalized electron and ion temperature gradients as well as the normalized density gradients are larger than the range limits. Hence between $0.95 < \rho < 1$ we are using QLKNN outside its training set. We have therefore checked that our modelling is not impacted by changing the boundary condition from $\rho = 1$ to $\rho = 0.95$ and the impact of changing the T_e value at $\rho = 1$ from 50 to 150 eV. Since the time of the training, QuaLiKiz Krook-like collisionality operator on trapped electrons has been improved thanks to comparison with GENE on JET and WEST-like test cases, see the chapter 6 of Ref. [101]. Since Trapped Electron Modes are at play in WEST dominant electron heated pulses studied here, a proxy has been applied on the collisionality input in QLKNN-10D (in the near future a new Neural Network will be retrained on a 1 billion points 11D database using the improved Krook operator). Meanwhile, the collisionality has been divided by 4 in all the simulations presented here. In QuaLiKiz a Krook-like operator has been chosen as detailed in ref. [102]. This operator has been found to predict too flat density profiles in JET electron heated pulses due to an over stabilization of TEM drive (turbulence driven by trapped electron magnetic curvature drift resonance). Therefore QuaLiKiz's collision operator has been tuned against GENE simulations. Meanwhile, dividing the collisions by a factor 4, to compensate for the

over-stabilization of TEM when using the Krook is proposed. This proxy has been shown to allow reproducing QuaLiKiz prediction in JETTO on JET I_p ramp up [103].

5.2.4 LUKE

The structure of the radio-frequency heating source module for the integrated modelling includes the code C3PO [104] coupled with LUKE. The ray equations are solved by the ray-tracing C3PO with a design based on chain derivatives for maximum modularity regarding the choice of coordinate system and dielectric model. LUKE computes the numerical solution of the three-dimensional linearised relativistic and bounce-averaged electron Fokker-Planck equation. This tool allows self-consistent calculations of the bootstrap current (the self-generated current spontaneously arise within the plasma due to collisions between trapped particles and passing particles.) in presence of other external current sources. The code computes the LHCD power absorption profile at each time using the code R5X2 [105] (part of LUKE code) provides a synthetic HXR diagnostic. An upgraded version which takes into account the effects of partial screening on the calculation of the braking radiation and on the collisions is used. More information about the code can be found in Ref. [101].

5.3 Modelling the radiative collapse

The aim is to model the $T_e(0)$ collapse using RAPTOR-QLKNN. Two pulses are targeted, the 55025 and 54802, both presented previously. The initial conditions and the boundary conditions of the RAPTOR-QLKNN simulation are taken from METIS. Moreover, in the simulations, the settings shown in table 5.1 are used.

$T_e and T_i$	P_{LHCD}	n_e	n_W	P_{rad}	$j(r)$	equilibrium
Predicted using QLKNN-10D	LUKE	interpretative	bolometry inversion	consistent with ADAS	predictive	self-consistent inside a fixed LCFS

Table 5.1 – Initial setting of RAPTOR-QLKNN simulations.

5.3.1 Discharge 55025

General data

In figure 5.2a the most important signals for simulations are plotted for the whole discharge to better see the history of the pulse. As can be seen, the volume averaged electron density (purple line) increases linearly until a collapse occurs. The central

temperature of the electrons (red line), once the second power plateau is reached, starts to decrease slowly, due to the increase in density, until it collapses in 0.4s. Regarding the tungsten density (orange line) at the center of the plasma, it is roughly constant throughout the discharge until it increases rapidly during the 0.4s of rapid collapse. The power injected by LH antennas is 2.8MW (green line).

The blue-coloured part in the figure 5.2a shows the time interval of the discharge that will be analysed. As we are interested in reproducing the radiative collapse, only two seconds involving the T_e decrease and fast collapse part will be simulated, from 8s to 10s. In figures 5.2b and 5.2c the profile of the electron temperature and the electron density are plotted for t=8 (start of the T_e decrease), 9.5 (start of the fast collapse) and 9.8s (end of the collapse). As can be noticed, the temperature decreases from the core to $\rho = 0.5$, while the density increases slowly until the end of the collapse when the profile becomes flatter.

The time evolution of the tungsten cooling factor is plotted in figure 5.3. We notice that tungsten radiation increases even if its density profile is constant, but this single ingredient is not sufficient to reproduce the collapse speed.

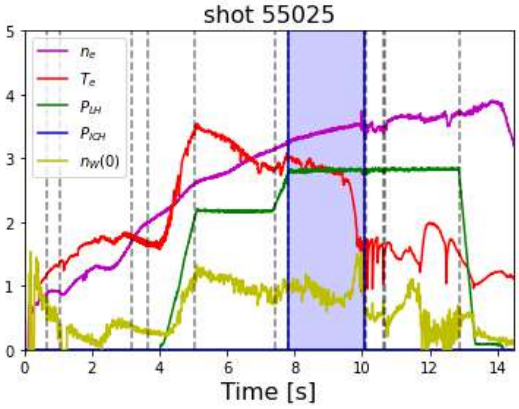

(a) The electron density increases during the whole discharge. The central electron temperature collapses. The central tungsten density increases during the fast collapse. The power injected by LH antennas is 2.8MW.

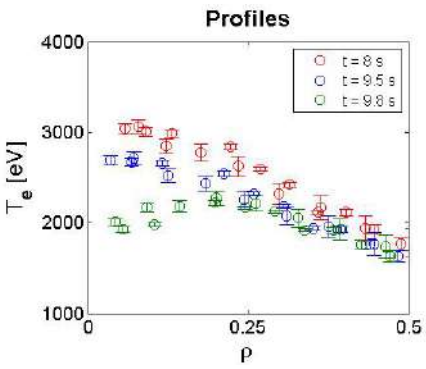

(b) Profile of the electron temperature for t=8 (start of the T_e decrease), 9.5 (start of the fast collapse) and 9.8s (end of the collapse). from $\rho = 0$ to $\rho = 0.5$ due to fast electron pollution of ECE signal by LHCD

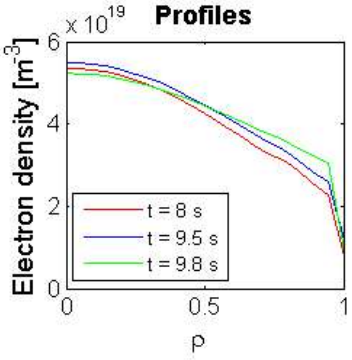

(c) Profile of the electron density for t=8, 9.5 and 9.8s.

Figure 5.2 – Overview of pulse 55025.

Tungsten peaking evolution

We assume that the tungsten profile can be approximated by a Gaussian symmetric function with respect to the center of the plasma with a constant background. To set the initial tungsten value, the peak reached and the timing of the accumulation, we use the results of the bolometry inversion. The Gaussian width of the tungsten profile is varied until the reconstructed line integrated radiative power matches the measured bolometer chords. Three times have been analysed: t=9.4 s, is the time just before the start of the fast collapse, t=9.6 s, is a time during the collapse and t=9.8 s is the end of the collapse.

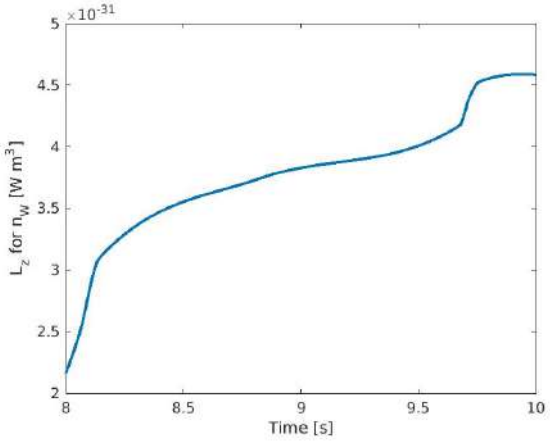

Figure 5.3 – Time evolution of the tungsten cooling factor at $\rho = 0$.

As explained in METIS settings description (5.1.1) the plasma composition is constrained by Z_{eff} and the bolometry measurements. Two impurities are accounted for, N constrained by Z_{eff} and W by bolometry. Due to the cooling factor specificities, the N contributes less than 7% to the central radiation as illustrated at 8s in the figure 5.4.

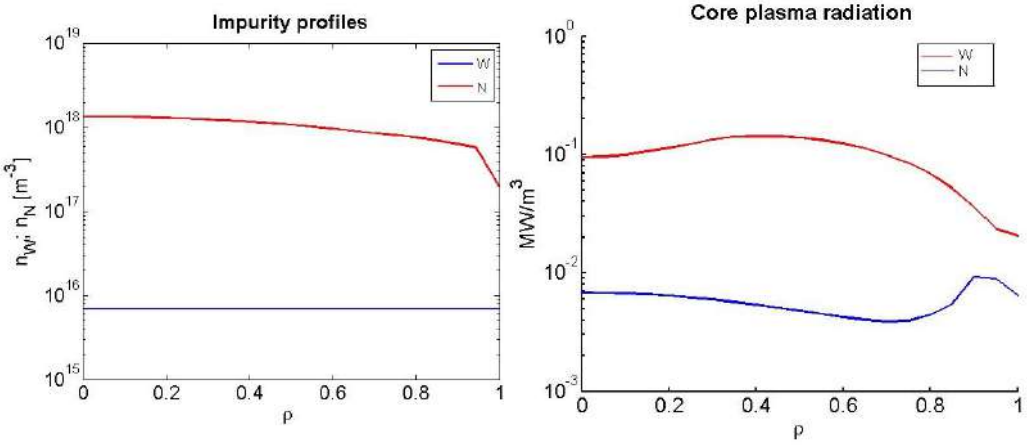

(a) (b)

Figure 5.4 – 5.4a Density profiles of tungsten and nitrogen at time t=8s. 5.4b Profile of the radiated power of tungsten and nitrogen at time t=8 for pulse 55025.

In figure 5.5, the left subplot corresponds to the tungsten density profile. In the right subplot red squares correspond to the measured line integrated radiated power while blue circles are the radiated power for each chord computed from the given tungsten profile using ADAS 50 cooling factor. In figure 5.5a a flat tungsten profile is imposed then a Gaussian profile peaked in the center with a width of 0.5 in normalized radius

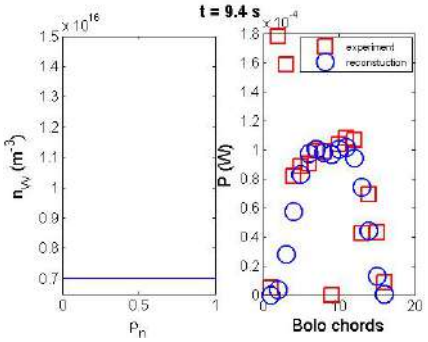

(a) At t=9.4s (prior to collapse), a flat tungsten profile is set.

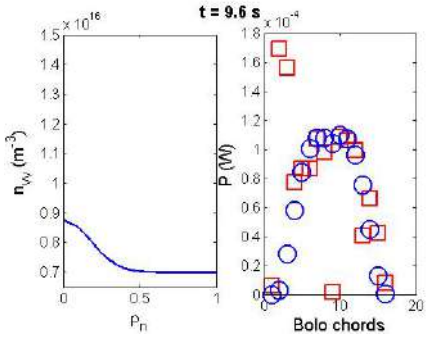

(b) At t=9.6s (during collapse), a peaked profile is set with a width of $0.5\rho_n$.

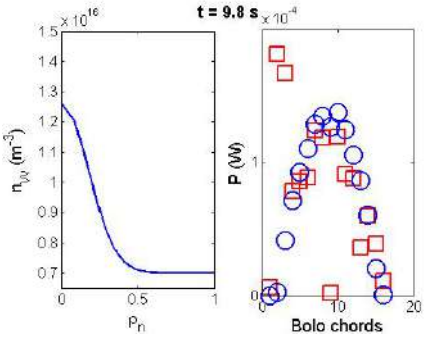

(c) At t=9.8s (at the end of collapse), a stronger peaked profile is set with a width of 0.5.

Figure 5.5 – For each pair of plots: the left subplot shows the given tungsten density profile, in the right subplot red squares correspond to experimental data while the blue circles are radiated power reconstructed from the given tungsten density profile. Chords 2 and 3 are not well reproduced as they point towards the divertor and we think they measure radiation produced by plasma-wall interactions; chord 9 on the other hand was removed during data processing.

is set (Fig. 5.5b). The central value increases linearly until the end of the collapse (Fig. 5.5c). Chords 2 and 3 are not well reproduced as they point towards the divertor and we think they measure radiation produced by plasma-wall interactions; chord 9 on the other hand was removed during data processing.

Since the tungsten accumulation plays a key role, its neoclassical and turbulent transport has been analysed. Neoclassical transport is computed using the drift kinetic code NEO [40]. The full linearised Fokker-Planck operator is used and the geometry is specified using Miller's parametrisation [41]. The discretisation is as follows: 5 Laguerre polynomials (the energy polynomials $\nu = \nu/(\sqrt{2}\nu_{ta})$), 19 Legendre polynomials (the cosine of the pitch angle $\xi = \nu_{||}/\nu$), 21 points in the poloidal direction. Input parameters are taken from a METIS simulation, T_e and T_i are interpretative and

n_e is fixed from the experiment.

To obtain the neoclassical diffusive (D) and convective (V) coefficients for tungsten, a scan in the density gradient is performed. This yields the tungsten peaking factor when the condition $\Gamma_W = 0$ is met or using the relation $R/L_{n_W} = -RV/D$. Using these computed normalised gradients at several radial locations (simulations are performed for $0.05 < r/a < 1$ with 41 radial points), one can reconstruct a tungsten density profile, if a boundary condition is provided. In this case we use the RAPTOR-QLKNN tungsten profile to set the boundary condition at $r/a = 0.3$. A different boundary condition, i.e. at $r/a = 0.8$ has also been tested. In these two cases, turbulent transport has also been computed on the same radial grid points using QuaLiKiz (but not the neural network version). The corresponding D and V have been added to the neoclassical ones to compute the tungsten peaking factors. It was found that inside $\rho = 0.3$, where most of the impurity transport is neoclassical, the turbulent fluxes are vanishing but they are taken into account. At $\rho = 0.8$, the turbulent diffusion is sufficiently large to flatten the tungsten profile.

The central tungsten density is computed between 8 and 10 seconds where the temperature collapse is experimentally observed. It is found in figure 5.6, where in blue is the tungsten density computed from the inversion of bolometry, that there is a mild tungsten accumulation (30% increase, black stars). Similar simulations are also performed changing only the normalised ion temperature gradient (R/L_{T_i}) and keeping all other parameters to the values at 8 s (red square). In orange the measured central electron temperature is plotted. It is observed that the tungsten peaking increases strongly due to a core T_e flattening, leading to T_i flattening by equipartition, hence reducing the neoclassical temperature screening effect. Impurity temperature screening is a favourable neoclassical phenomenon involving an outward radial flux of impurity ions from the core of fusion devices. Quasisymmetric magnetic fields lead to intrinsically ambipolar neoclassical fluxes that give rise to temperature screening. Therefore, we can conclude that the temperature flattening is the main driver for this accumulation.

The impact of nitrogen is also investigated. Indeed the nitrogen content (constrained through a computed resistive Z_{eff}) has a large impact on the reconstructed tungsten profiles due to an increase of the neoclassical tungsten diffusivity in presence of collisions with additional impurities (Figure 5.7).

These results with and without nitrogen are compared to bolometry, using ADAS 50 to compute the emissivity and using the line of sights of the diagnostic. To rebuild the bolometry chords only the tungsten is used since nitrogen has very little impact on the synthetic signal for the central chords. The synthetic signal changes at $t = 8s$ but is less pronounced than for the phase featuring the accumulation at $t = 9.7s$. These changes can be interpreted from changes in the profiles from figure 5.7 where a lower reduction of the tungsten peaking with increased nitrogen content is observed at $t = 8s$. Since the tungsten peaking at $t = 8s$ is relatively low (almost flat profile from the modelling), increased tungsten diffusivity has less impact compared to the case

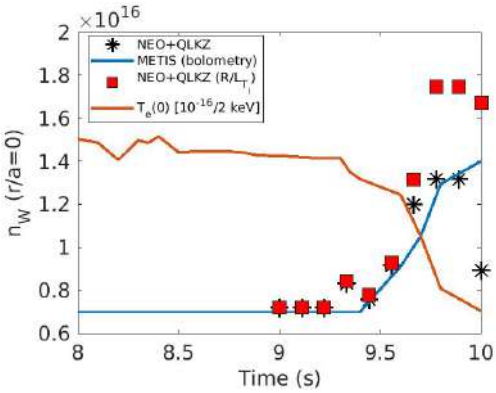

Figure 5.6 – In blue: tungsten density computed from the inversion of bolometry. In orange: the measured central electron temperature. Black stars: tungsten accumulation computed by NEO. Red squares: tungsten computed by NEO but changing only the normalised ion temperature gradient.

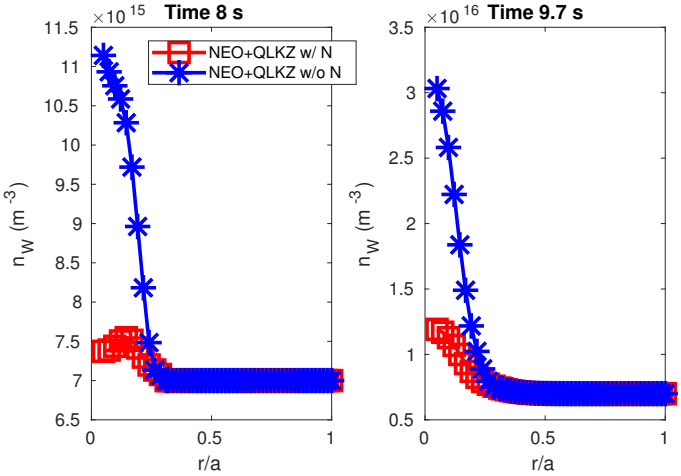

Figure 5.7 – Reconstructed tungsten density profiles using a boundary condition at $r/a = 0.3$ for cases with and without nitrogen at two time slices, before and during the tungsten accumulation.

where the accumulation occurs (at $t = 9.7s$). Only the central chords (6 to 12) should be compared. In Figure 5.8, we see that the impact of nitrogen is needed to recover measured powers (Fig. 5.8a). Indeed, without nitrogen, the tungsten impurity peaking is too large and produces too strong central tungsten densities, in particular during the tungsten accumulation at 9.7s (Fig. 5.8b).

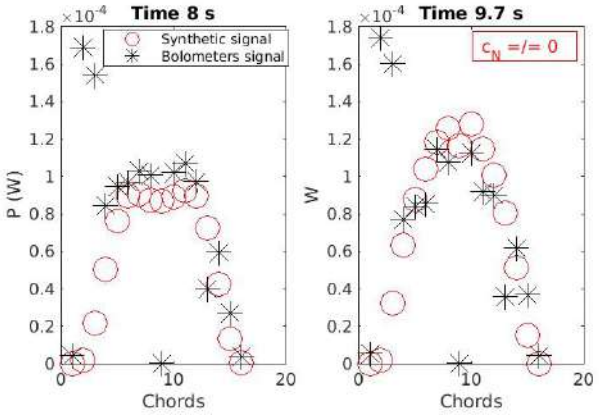

(a) Comparison with nitrogen.

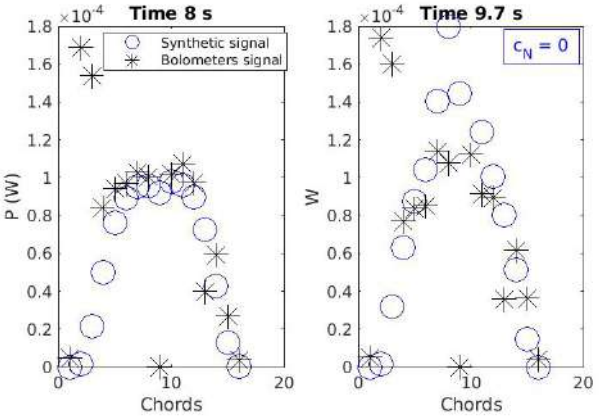

(b) Comparison without nitrogen.

Figure 5.8 – Comparison of the measured powers using bolometry and corresponding synthetic data with the reconstructed tungsten density profiles. Chords 2 and 3 are not well reproduced as they point towards the divertor and we think they measure radiation produced by plasma-wall interactions; chord 9 on the other hand was removed during data processing.

LHCD absorption evolution

The LUKE code is used to model the LHCD absorption during the collapse. LUKE is used in stand alone to prepare the power absorption profiles which are then transferred into RAPTOR. Five times are considered, one time into the P_{LH} flattop (t=8s) and the other four times during the fast collapse (t=9.5, 9.6, 9.7, 9.8s) (Fig. 5.9a).

Since the power at the center is due to fast electrons, the current profiles (J_{tot}) with anomalous transport are used to determine LHCD power absorption profiles (P_{LH}), we consider that heating and current drive follow the same radial profile (figure 5.9a). Moreover, the power absorption in the very core ($r/a < 0.1$) cannot be computed with the required spatial accuracy. RAPTOR simulations can constrain this value, therefore, the central value is adjusted in time to match the temperature evolution. A progressive decrease of the core electron heating by LHCD occurs during the slow density rise.

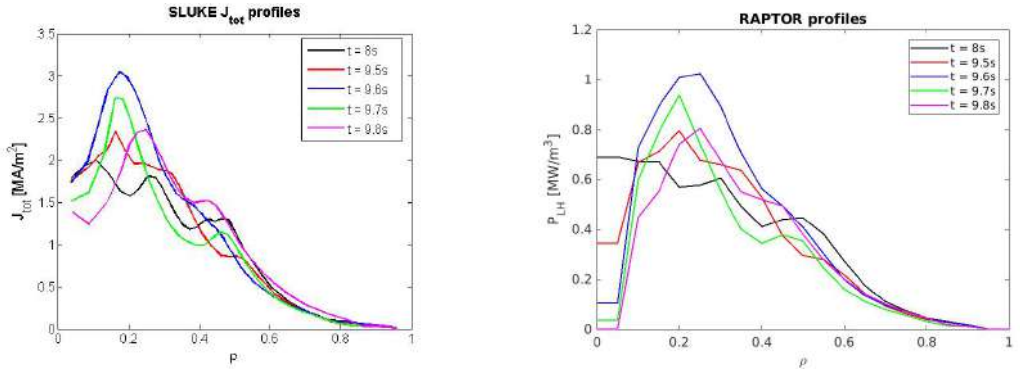

(a) J_{tot} profiles with anomalous transport computed by LUKE.

(b) The five profiles used for RAPTOR simulation. The central value is adjusted in time to match the temperature evolution (see figure 5.10).

Figure 5.9 – LUKE's current profiles were normalised with respect to injected power.

Then it is amplified before the radiative collapse (see Fig. 5.9b). Also as the current profiles are used to compute the LHCD power absorption these profiles need to be normalized to the volume and multiplied by the total injected power.

In order to determine the evolution of the central LHCD power absorption, a sensitivity analysis is done. It consists in finding the optimum between the relative errors of the central electron temperature and the central electron temperature time gradient. The formulas used are the following:

$$\epsilon_{temperature} = \frac{\left| T^{experiment} - T^{simulation} \right|}{T^{experiment}} \tag{5.1}$$

$$\epsilon_{slope} = \frac{\left| (T_{t-1}^{experiment} - T_t^{experiment}) - (T_{t-1}^{simulation} - T_t^{simulation}) \right|}{T_{t-1}^{experiment} - T_t^{experiment}} \tag{5.2}$$

Two times are shown in the figure 5.10. For each time a scan of the central injected LHCD power is performed. Increasing the central injected power, the error on the temperature decreases (light blue and pink lines) but the error on the temperature dynamics (time derivative) increases (blue and red lines), therefore the collapse shape is no longer reproduced. On the other hand, decreasing the power, the error on the temperature gradient reaches a minimum and then it increases again, but the temperature error increases a lot. Therefore, the LHCD electron heat source in the plasma center is chosen in order to have the optimum of the half-sum of the two gradients, as shown in figure 5.10 for the time t=9.5s and t=9.6s.

From LUKE simulations and using of RX52 code, synthetic HXR signals are produced

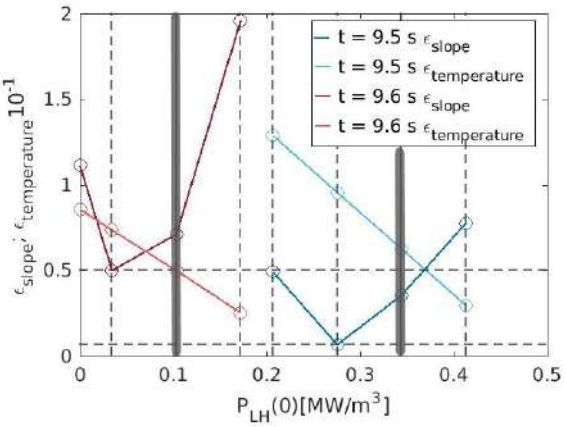

Figure 5.10 – Sensitivity analysis performed to choose the optimum central LHCD deposited power. The blue and the red lines are the central electron temperature time derivative relative error (ϵ_{slope}), while the light blue and the pink lines are the central electron temperature relative error ($\epsilon_{temperature}$). The thick vertical grey lines indicate the central LHCD powers chosen for the performed simulations.

and compared to the measured HXR signal from the 60-80 keV band of energy. We observe that the reconstruction matches well the measurements given the challenge of multipass absorption modelling as explained above (see figure 5.11).

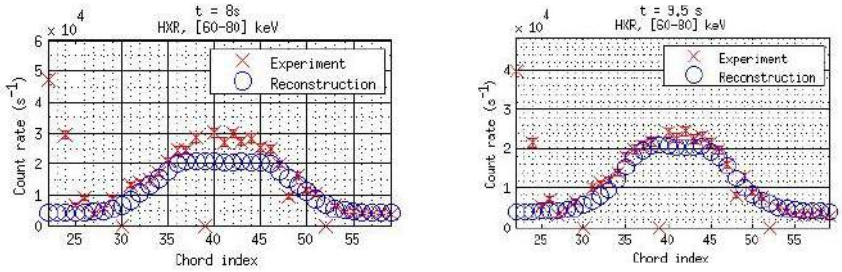

(a) t=8s

(b) t=9.5s

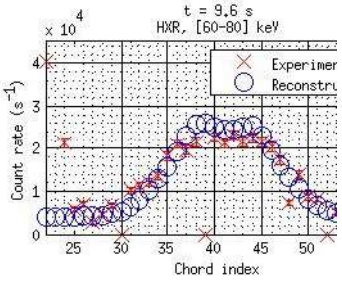

(c) t=9.6s

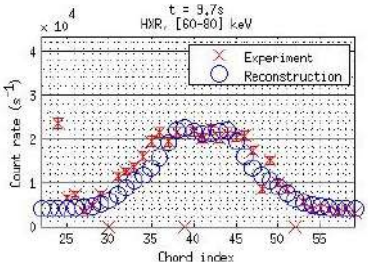

(d) t=9.7s

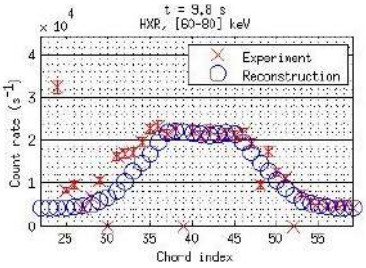

(e) t=9.8s

Figure 5.11 – The experimental value of the HXR signal for each chord (red crosses) is compared with the HXR signal reconstructed by LUKE (blue circles).

RAPTOR-QLKNN simulations

To disentangle the respective role of the increase of tungsten inside $\rho = 0.5$ from the decrease of the central LHCD absorption, different simulations of RAPTOR-QLKNN have been run: flat and constant tungsten concentration with LHCD power absorption computed from LUKE (green dashed line in figure 5.12a), only tungsten increase with a constant profile of LHCD (frozen at t=8s) (purple line in figure 5.12a) and with both, the contribution of tungsten and the LHCD central absorption (orange line in figure 5.12a).

One can notice that the core tungsten peaking only is not sufficient to reproduce the first part of the collapse. Moreover, the fast collapse is not obtained, the electron temperature continues to decrease but not as fast as in the measurement. When

the LHCD profiles from LUKE are added, the slow T_e decrease is reproduced. If only the reduction of LHCD central absorption and the increase of the cooling factor are taken into account, the collapse occurs but the temperature does not fall below 2keV. Moreover, the collapse seems to start a little later. If also the tungsten accumulation is considered, the temperature decreases below 2keV and the speed of the experimental collapse is captured. This is also in agreement with the results found with NEO-QuaLiKiz: T_e decreases making W core concentration to increase that makes T_e to decrease further. Therefore, if W transport is mainly neoclassical, an initial T_e flattening is needed to trigger W accumulation. Then, when the vicious cycle is initiated, both phenomena happen simultaneously. The greater the density of the tungsten, the greater the radiation as shown by the formula 4.1. Therefore, an increase in n_W automatically increases P_{rad} and therefore T_e decreases.

The fraction of radiated power in the core (between $\rho = 0$ and 0.1) is also analysed. The radiated power is calculated using the expression: $P_{rad} = n_e(t) n_W(t) L_z(t)$, where the total power (P_{tot}) is the sum of injected power plus ohmic power inside $\rho = 0.1$. In figure 5.12b the time evolution of the radiated fraction for the three simulations is plotted. The dashed horizontal black line represents the limit where the radiated fraction ($f_{rad} = P_{rad}/P_{tot}$) is unity. In all of the cases the cooling factor (L_z) varies as a function of time (see figure 4.16b). The two cases for which the limit $f_{rad} = 1$ is exceeded are the two modelled cases where the $T_e(0)$ collapse occurs. The green line crosses unity later than the orange line, and in fact, as observed in the simulations, the collapse starts earlier when both the tungsten build-up and the lowering of the LHCD power are considered.

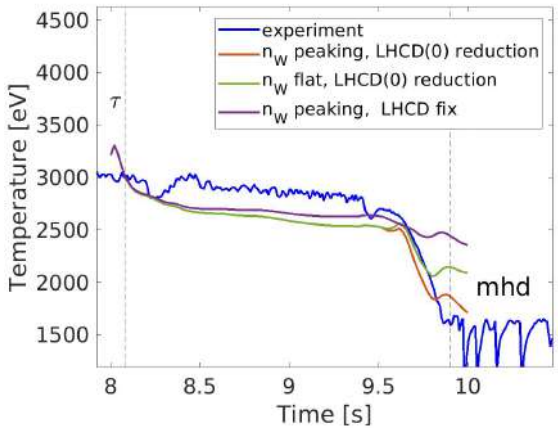

(a) Time behaviour of dynamic collapse for different simulations.

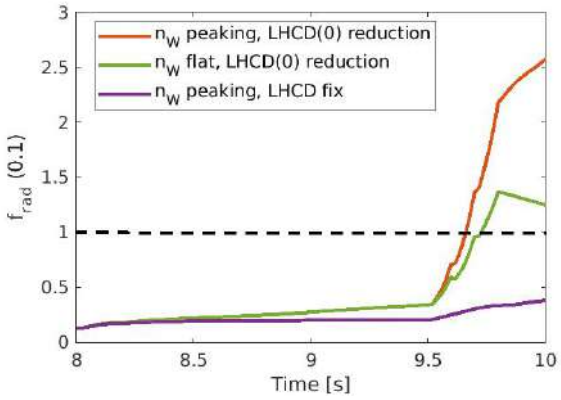

(b) The fraction of radiated power inside $\rho = 0.1$ is computed for each simulation. The horizontal dashed black line corresponds to $f_{rad} = 1$ inside $\rho = 0.1$.

Figure 5.12 – The blues line corresponds to the central electron temperature taken from the experiment, green dashed line corresponds to the simulations in which the flat tungsten profile is constant with LHCD power absorption decreasing, the purple line is the simulation in which only tungsten increases and the orange line is for both, the contribution of tungsten peaking and LHCD absorption decrease.

The temperature profiles at different times can be visualised in figures 5.13. During the fast collapse, the T_e central reduction matches well the experimental data and in particular reproduces the hollowness of the central electron temperature when both the tungsten core peaking and the LHCD central absorption reduction are taken into account. Regarding the ECE signal points for $\rho > 0.5$, these are overestimated due to the effect of fast electrons suprathermal emission.

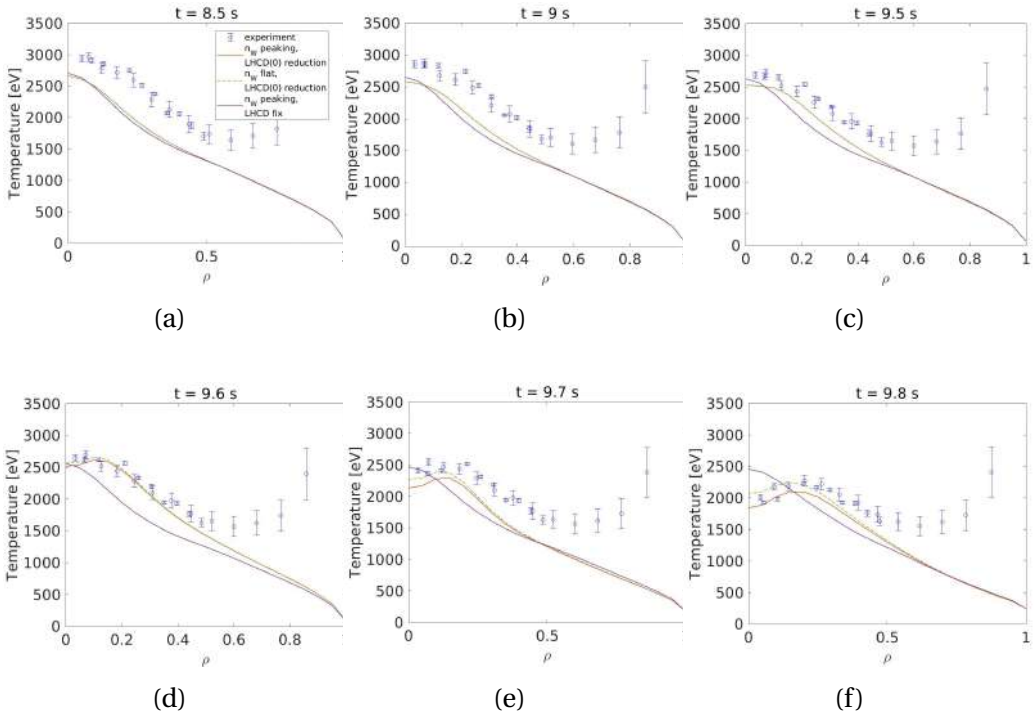

(a) (b) (c)

(d) (e) (f)

Figure 5.13 – In blue the temperature profiles measured by ECE with error bars, in orange the temperature computed for tungsten accumulation with LHCD central absorption decreasing, in dashed green the temperature for flat tungsten with LHCD central absorption decreasing and in purple the temperature for tungsten accumulation and constant LHCD power absorption profile. Figures 5.13a and 5.13b are two times before the collapse, while figures from 5.13c to 5.13f are times during collapse.

V_{loop} and the $l_i(3)$ produced by the RAPTOR-QLKNN simulation accounting for the tungsten peaking and the LHCD central absorption reduction are compared with the measured V_{loop} and the $l_i(3)$ from NICE magnetic reconstruction constrained by polarimetry. The comparison is shown in figure 5.14. Regarding the V_{loop} time behaviour, they are rather close (figure 5.14a). l_i seems underestimated in the modelling probably due to the fact that the simulation underestimates the central value of the electron temperature (figure 5.14b).

Since there are no measurements for the edge electron temperature, the impact of changing boundary conditions was analysed. Therefore the electron temperature at the separatrix is changed from 50 eV to 150 eV. As it is possible to see from figures 5.15a, the central temperature is slightly lower, anyway the collapse happens. Even the effects on the magnetic shear are small (figure 5.15c). It is possible to conclude that the boundary conditions for electron temperature do not influence the temperature profile and thus the transport.

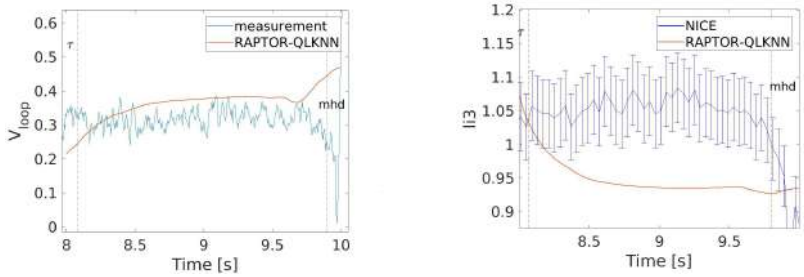

(a) V_{loop} time behaviour comparison (b) $l_i(3)$ time behaviour comparison. Also the error bar for the NICE li3 reconstruction is plotted.

Figure 5.14 – Comparison between RAPTOR computation and NICE reconstruction.

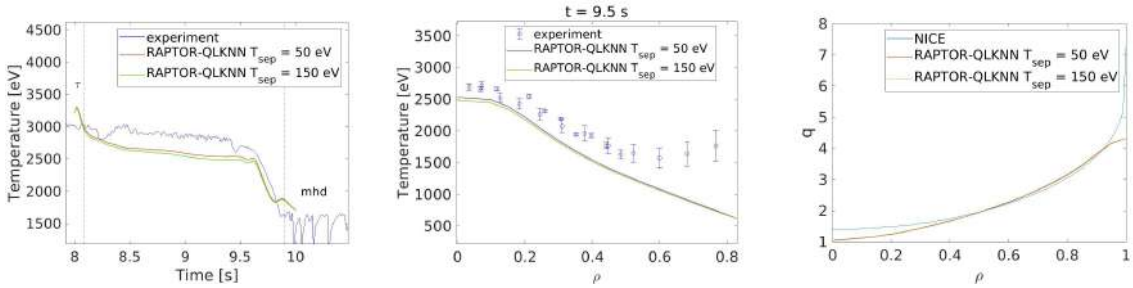

(a) Collapse comparison

(b) T_e profile comparison at t=9.5s.

(c) q profile comparison at t=9s.

Figure 5.15 – 5.15a The boundary condition has been changed from taking $T_{e\,sep} = 50eV$ to $T_{e\,sep} = 150eV$.

5.3.2 Discharge 54802

General data

In figure 5.16a different signals for discharge 54802 are plotted. The same trends as in previous discharge (55025) are found for electron density (purple line), central electron temperature (red line), the central tungsten density (orange line) increases during the fast collapse. The power injected by only one LH antenna is 1.8MW (green line). The blue-coloured part in the figure 5.16a shows the time interval of the discharge that will be analysed, from 4.5s to 5.9s. In figures 5.16b and 5.16c the profile of electron temperature and electron density are plotted for t=4.5s (start of T_e decrease), 5.6s (start of the fast collapse) and 5.9s (end of the collapse). The temperature decreases from the core to $\rho = 0.5$, while the density increases slowly until the end of the collapse when the profile becomes flatter.

The time evolution of the tungsten cooling factor is plotted in figure 5.17. We notice that tungsten radiation increases even if its density profile is constant, but, as for previous pulse, this single ingredient is not sufficient to reproduce the collapse speed.

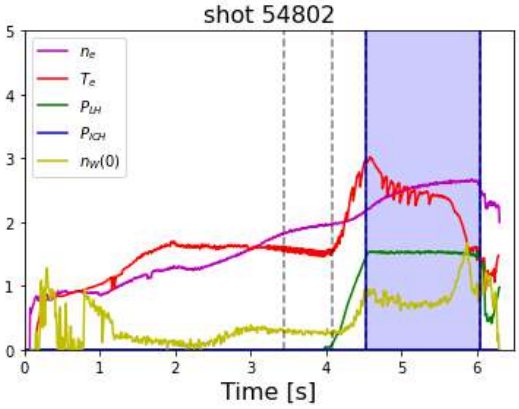

(a) The electron density increases during the whole discharge. The central electron temperature collapse and its behaviour is followed by the HXR signal. The central tungsten density increases during the fast collapse. The power injected by only one LH antenna is 1.8MW.

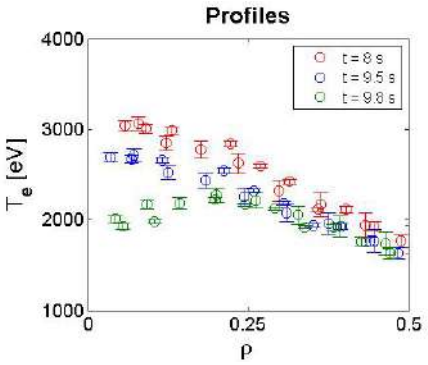

(b) Profile of the electron temperature for t=4.5 (start of the T_e decrease), 5.6 (start of the fast collapse) and 5.9s (end of the collapse) from $\rho = 0$ to $\rho = 0.5$ due to fast electron pollution of ECE signal by LHCD. 5.16c Profile of the electron density for the same times.

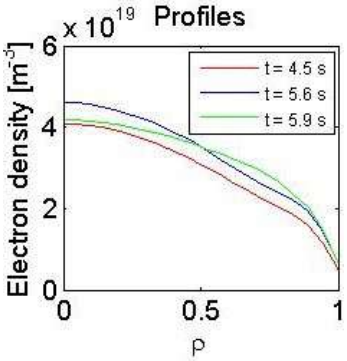

(c) Profile of the electron density for the same times.

Figure 5.16 – 5.16a Overview of pulse 54802.

Tungsten peaking evolution

Tungsten profiles for three times are presented: at t=5.5s, just before the start of the fast collapse, at t=5.7s, during the collapse and at t=5.9s, when the collapse ends. In figure 5.18 the first subplot corresponds to the tungsten density profile and in the second plot the red squares correspond to the measured line integrated radiated power

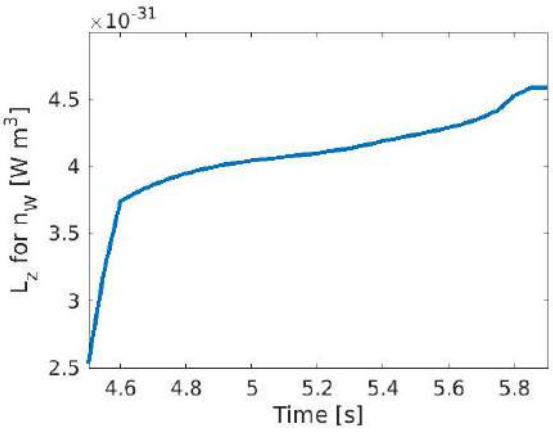

Figure 5.17 – Time evolution of the tungsten cooling factor.

while the blue circles are the reconstructed radiated power from the tungsten profiles. In figure 5.18a a flat tungsten profile is imposed then a Gaussian profile peaked in the center with a width of 0.4 in normalized radius is set (5.18b) and the central value increases linearly up to the end of the collapse (5.18c). In all cases studied the tungsten profiles considered are able to reproduce the central bolometry chords taken from the experiment. This means that tungsten starts to accumulate in the center when the temperature starts to collapse.

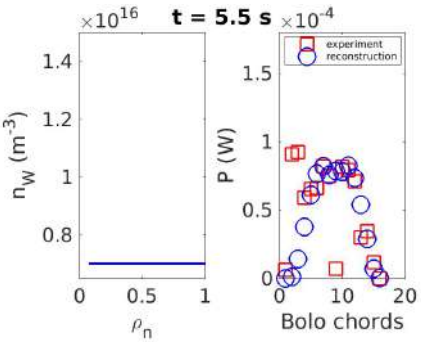

(a) fit=5.5s, a flat tungsten profile is set.

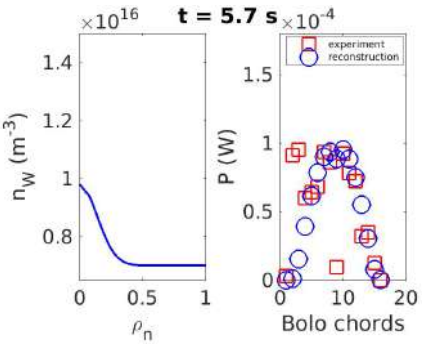

(b) t=5.7s, a peaked profile is set with a width of $0.4\rho_n$.

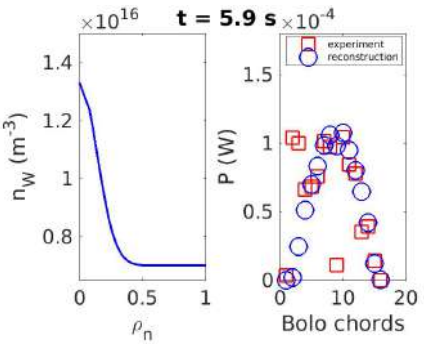

(c) t=5.9s, a peaked profile is set with a width of $0.4\rho_n$.

Figure 5.18 – For each pair of plots: the left subplot shows the imposed tungsten density profile, in the right subplot red squares correspond to experimental data while the blue circles are radiated power reconstructed from the tungsten density profile. Chords 2 and 3 are not well reproduced as they are the two chords that point the divertor and they are polluted due to plasma wall interaction; chord 9 on the other hand was removed during data processing.

LHCD absorption evolution

The LUKE code is used to model the LHCD absorption. Four times are considered, one belonging to the first part of the collapse (t=4.5s) and the other three during the fast collapse (t=5.6, 5.7, 5.9s). As for previous pulse, current profiles with abnormal transport are used to determine LHCD heat radial absorption (Fig. 5.19a). In this case only the central value of the profile at t = 4.5s is adjusted to match central T_e, the other profiles were linearly extrapolated to the center of the plasma (Fig. 5.19b). The profiles are normalized to match the total injected LHCD power.

In figure 5.20 the normalized HXR signals for the 60-80 keV band of energy computed by the code are compared with the experimental values. Since the radial power profiles are normalized, it is not fundamental to have the exact value, what is important is the shape, as this feature reflects the radial power absorption profile. Therefore,

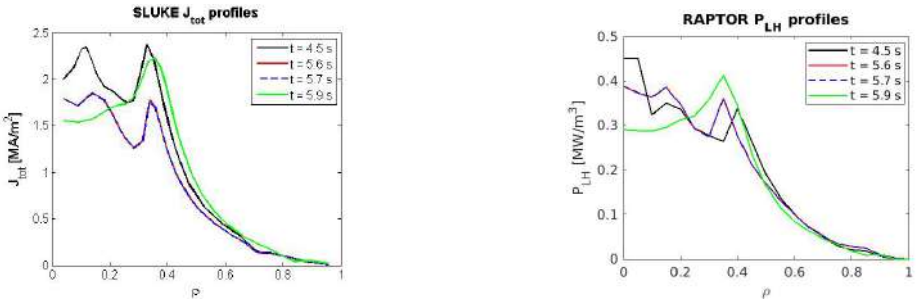

(a) J_{tot} profiles with abnormal transport computed by LUKE.

(b) The five profiles used in RAPTOR simulation. The central value is adjusted in time to match the temperature evolution.

Figure 5.19 – LUKE's current profiles were normalised with respect to injected power.

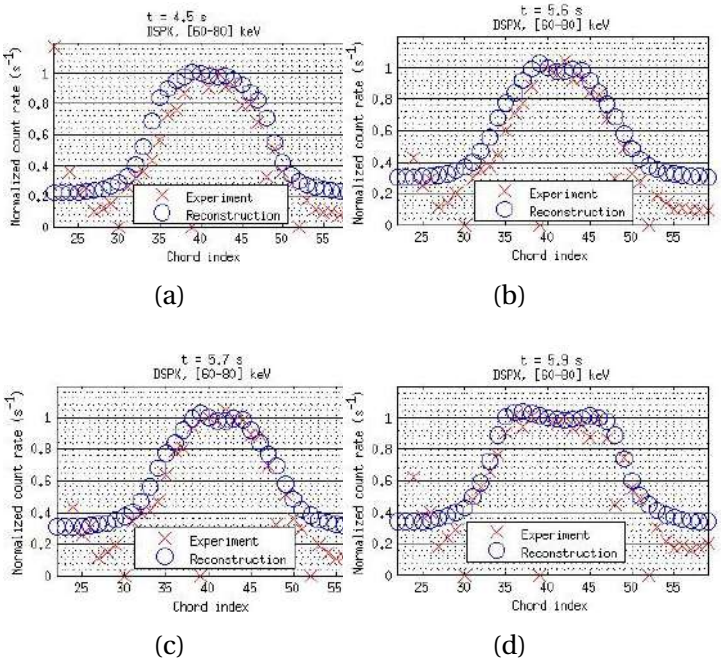

(a) (b)

(c) (d)

Figure 5.20 – The experimental value of the HXR signal for each chord (red crosses) is compared with the HXR signal reconstructed by LUKE (blue circles). In this case the values are normalized.

the normalized values of the HXR signals are shown, and we observe that the shape are well reconstructed.

RAPTOR-QLKNN simulations

As for the previous pulse, three different simulations RAPTOR-QLKNN have been run: flat and constant tungsten concentration with LHCD power absorption computed from LUKE (green dashed line in figure 5.21), only tungsten increase with a

constant profile of LHCD (t=4.5s) (purple line) and with both, the contribution of tungsten and LHCD absorption (orange line). Also in this case, only increasing of tungsten is not sufficient to reproduce the first part of the collapse, but it seems to have the same effect as the reduction of LHCD central absorption alone. Either way, both, tungsten accumulation and the LHCD reduced core absorption are needed to reproduce the collapse.

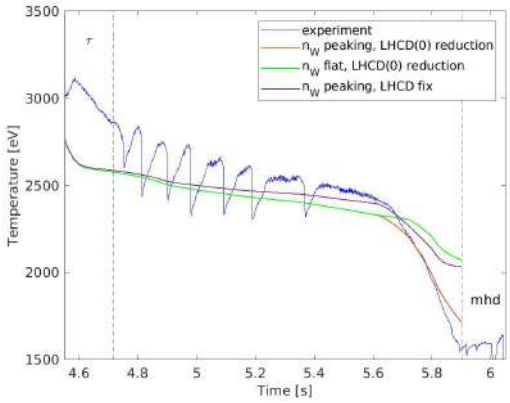

(a) Time behaviour of dynamic collapse for different simulations.

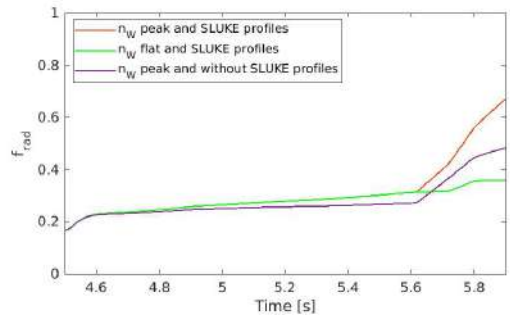

(b) The fraction of radiated power is computed of each simulation.

Figure 5.21 – Time behaviour of different simulations. The blue line corresponds to central electron temperature taken from the experiment. The green dashed line corresponds to the simulations in which the tungsten is flat and constant with LHCD power absorption computed from LUKE, the purple line is the simulation in which only the tungsten increases and the orange line is for both contributions, with tungsten peaking and LHCD absorption varying.

In figure 5.21b the time behaviour of the radiated fraction for the three simulations done is plotted. In this case it is not necessary that the fraction radiating into the core

is greater than the power injected into the same volume of plasma. This is probably because the contribution of tungsten accumulation in this discharge is similar to the contribution of LHCD deposition. In any case, both these contributions are necessary to reproduce the collapse rate.

The temperature profiles at different times can be visualised in figures 5.22. During the fast collapse, central T_e reduction matches well the experimental data and in particular when both the tungsten core peaking and the LHCD central absorption reduction are taken into account. Regarding the ECE signal points for $\rho > 0.5$, they are overestimated due to the effect of fast electrons suprathermal emission.

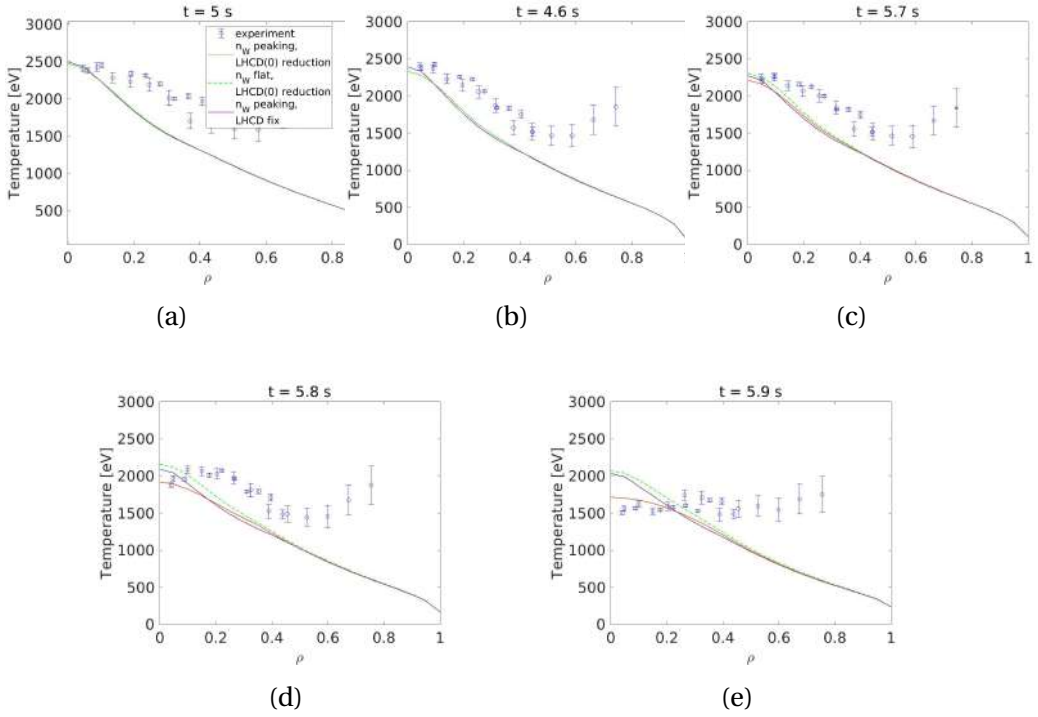

Figure 5.22 – In blue the temperature profiles measured by ECE with error bars, in orange the temperature computed for tungsten accumulation with LHCD central absorption decreasing, in dashed green the temperature for flat tungsten with LHCD central absorption decreasing and in purple the temperature for tungsten accumulation and constant LHCD power absorption profile. Figures 5.22a is a times before the collapse, while figures from 5.22b to 5.22d are times during collapse.

Also in this case, the modelled V_{loop} and the $l_i(3)$ are compared with respectively the measurement and the magnetic equilibrium reconstruction of the pulse. The comparison is shown in figure 5.23. The two quantities are rather well reproduced.

In general, we can say that the 54802 discharge follows the same dynamics as the

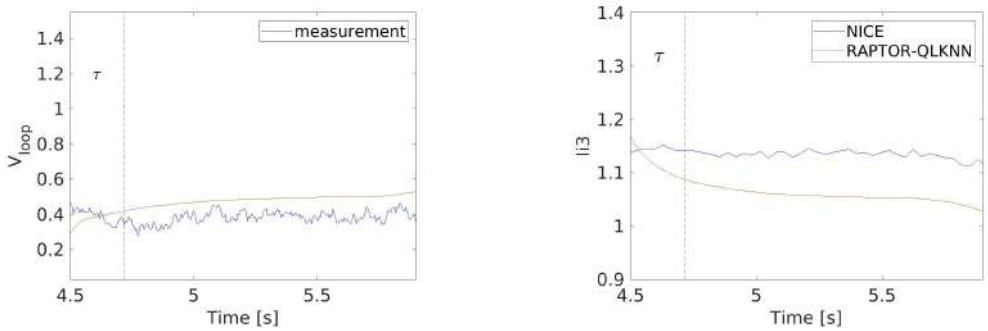

(a) V_{loop} time behaviour comparison. (b) $l_i(3)$ time evolution comparison

Figure 5.23 – Comparison between RAPTOR computation and NICE reconstruction.

collapse of 55025 discharge. This allows us to conclude that the actuators of the $T_e(0)$ collapse are: the reduction of LHCD power core absorption, the cooling factor due to the drop of temperature and, therefore, the increase of tungsten accumulation. These parameters may contribute in different percentages depending on the discharge analysed, but they must all be taken into account simultaneously in order to simulate the experimental collapse. This is shown in figures 5.24, where on the x-axis the ratio of the temperature difference between the beginning and the end of the fast collapse normalised to the temperature at the end of the collapse was calculated for the experimental data. On the y-axis we have the same quantity but for the simulated temperature. This quantity has been calculated for the case where only the tungsten peaking is considered (purple square), only the LHCD core absorption is reduced (green diamonds) and if both are considered (orange triangle). In the figure, both discharges have been represented. As can be seen, the contribution of the two ingredients is different in order to reproduce the temperature fall during the collapse, but both are necessary.
For both discharges, the temperature calculated by RAPTOR-QLKNN is generally underestimated. This is probably due to the fact that the value of the power injected at the centre was not changed, only linearly extrapolated. A modification is probably necessary in order to match the measured initial temperature, so as to have a better reproduction of the temperature behaviour for the rest of the discharge. Since this is an arbitrary choice, it was decided not to leave the initial temperature at the centre of the plasma unchanged. This does not exclude the possibility that other physical mechanisms could also be present during the collapse.

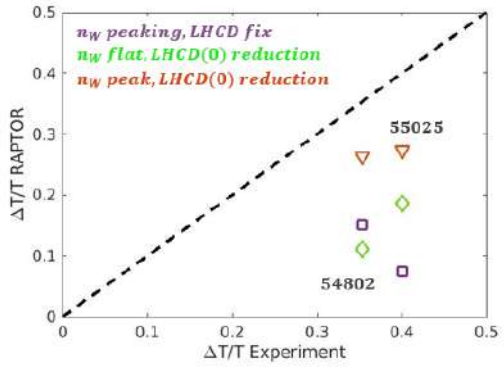

Figure 5.24 – Ratio of the temperature difference between the beginning and the end of the fast collapse (time gradient of the temperature) normalised to the temperature at the end of the collapse for the case where only the tungsten peaking is considered (purple square), only the LHCD decreases in the plasma core (green diamonds) and when both effects are considered (orange triangle).

5.4 Conclusion of the chapter

The key players at the origin of the transition from the hot to the cold branch are identified through the integrated modelling of two typical cases, pulses 55025 and 54802.
The modelling framework is composed of interpretative METIS simulations and predictive RAPTOR simulations using QuaLiKiz neural network for heat transport. LUKE code, in stand alone, is used to determine the LHCD power absorption profiles (in the multi pass absorption, the centrally absorbed value is not precisely captured, it is hence adjusted to match the central T_e evolution). The tungsten density and its profiles are computed using bolometry inversion. The radiated power is computed using ADAS 50 for the tungsten cooling factor.
For both studied discharges, the first slight decrease of temperature is due to the increase of electron density. The single growth of core tungsten concentration is not sufficient to reproduce the collapse. When also the reduction of LHCD central power absorption is considered, the collapse is reproduced. If only the reduction of LHCD central absorption and the increase of the cooling factor are taken into account, the collapse occurs but the speed of the collapse is weaker than experimentally observed. Therefore, three effects happening simultaneously are required to capture the velocity of $T_e(0)$ drop: cooling factor increase, LHCD central absorption reduction and tungsten accumulation.

Regarding the first ingredient, as the cooling factor is directly linked to the electron temperature, an initial T_e reduction makes the cooling factor to increase inducing a further decrease in T_e, in a vicious cycle. The core LHCD power absorption is reduced as expected in a colder plasma [39] because the peak of the deposition moves further

off-axis with the decrease of central T_e. This leads to a negative power balance in the core that initiates the temperature collapse. At the same time, the ∇T_e flattening induces a ∇T_i flattening by equipartition, and, if tungsten transport is mainly neoclassical, an initial T_e flattening is needed to trigger W accumulation. Therefore, tungsten profile peaks. Then, when the vicious cycle is initiated, both phenomena happen simultaneously. In the end, a broadening of the current profile occurs (drop of l_i) and MHD activity is triggered.

To avoid core radiative collapses central electron heating is crucial for two reasons: 1) to be as far as possible above the temperature range in which the tungsten cooling factor increases with lower T_e ($> 3keV$) and therefore become insensitive to mild density increase; 2) to beat the core tungsten radiation in the core and therefore to be resilient to higher levels of tungsten contamination.
In WEST coming campaigns, using dominant LHCD, the central electron temperature will be monitored by raising the ratio of injected power over density.
The core electron heating will be maximized, thanks to ICRH dedicated experiments adjusting the frequency and the H minority concentration. From 2023, central electron heating will be complemented by 3 gyrotrons providing 3MW of ECRH.

Conclusion

Studying the performance of magnetic fusion devices is of fundamental importance in order to extrapolate towards larger and more powerful devices such as ITER and DEMO. For this reason, the tokamaks currently available, thanks to their dedicated experiments, are important steps on the road to energy production from nuclear fusion.
There are many parameters that can influence the energy confinement time of a tokamak, the most important of which, plasma current, electron density, total power, toroidal magnetic field, elongation, major radius, aspect ratio and atomic mass, lead to the definition of the scaling law capable of calculating, and thus predicting, the magnetic confinement time. This, allows the definition of operational windows in which the device can operate safely and achieve desired performance levels.

In this thesis, using the existing tokamak database, the two existing main L mode scaling laws ITER89-P and ITER96-L are well reproduced both in dimensional and dimensionless parameters and their different aspect ratio scaling has been understood. In particular, the differences come from a gap between aspect ratio value between 4.4 and 5.5. These is due to the discharges in single null configuration of JT-60 tokamak. For these pulses the thermal energy confinement time is not provided and, moreover, they are characterized by a smaller plasma volume which itself correlates with a degradated energy content.

The WEST database was exploited to study how WEST most important characteristics can influence plasma performance. Among these, the aspect ratio and radiated power due to tungsten contamination were analysed in detail.
Regarding the former, WEST has an aspect ratio around 5-6, which is much larger than the other L-mode tokamaks. For this reason, WEST was added to the ITER96-L database and the coefficients of the linear regression were analysed, both in dimensional and non-dimensional parameters. In both cases, the regression coefficient for the aspect ratio is always around 0, which means that a large aspect ratio does not impact the performance of tokamaks.
On the other hand, when operating in tokamaks with tungsten-covered first walls and divertor, the radiated power was subtracted from the total power, which in WEST is a large percentage (30% to 50%). Again, the power law was analysed. The regressors show no significant differences. These results show that even in presence of large radiation, the energy confinement behaviour is not modified. Therefore, WEST confinement properties are not significantly impacted by high tungsten content and therefore large radiated powers.

In addition, the differences between WEST and the ITER96-L database were analysed. In particular, a reduced scaling law was considered. This only includes the plasma current, electron density and total power. In comparison with ITER96-L, a higher correlation with the plasma current was found. This is due to WEST's small operational range of 0.3MA to 0.7MA with most experiments (about 75% of all plateaus) at 0.5MA. This parameter can be improved by increasing discharges at lower, or higher, current, or by increasing the operational range. The regression coefficient for total power is very close to that of ITER96-L. In contrast, density shows a negative correlation, and this could be due to the dominant LHCD heating that might add some specificities such that a central heating shifts outward for denser plasmas. More studies have been done on this and more information can be found in ref. [M. Goniche, V. Ostuni et al. submitted to NF].

Also, the impact of the radio frequency heating has been analysed splitting the WEST database into discharges with $P_{LH} > 1MW$ and discharges with $P_{ICH} > 1MW$. The two scaling laws show an inverse dependence with respect to the density, this might reflect the fact that denser plasmas lead to an outward displacement of the LHCD absorption.
Moreover, the power degradation exponent is larger when the bulk radiation is removed. This means that the degradation of the confinement time due to turbulent transport only is larger than with both turbulent and radiative losses.

The ohmically heated pulses are analysed. Plotting the experimental energy confinement time as a function of the line-averaged electron density the change of confinement time from linear ohmic confinement regime (LOC) to saturated ohmic confinement regime (SOC) has been observed. An initial linear confinement time evolution is followed by a saturated phase.

In WEST operation a hot and a cold branch coexist. The first one is characterized by an electron temperature higher that 2keV, higher internal inductance and neutron flux; while the cold branch shows a temperature around 1.5keV, lower li and neutron flux and it is also characterized by a saturation with respect to the increase of the total power divided by the volume electron density.
It has been noticed that some discharges in the hot branch collapse on the cold one. These pulses have in common a rapid collapse of the central electron temperature. A simple model to detect the collapse is developed. We have found that 25% of the discharges in the hot branch collapse. Moreover, all the unstable plateaus are located in the region between 1.5 keV and 3keV. This is in agreement with the tungsten cooling factor unstable region, in which a decrease of the central electron temperature increases the radiation potentially leading to further temperature decrease.
The time evolution of the collapse is characterized by a first slow decrease of the central temperature and, at the same time, an electron density increase, then a fast collapse occurs. The signal of the HXR central channel for the energy band 60-80 keV

decreases, a signature of a reduced central LHCD absorption. The tungsten density is flat prior to the collapse and then it peaks during the fast collapse.
We conclude that potential causes for the $T_e(0)$ collapse are: the reduction of the central LHCD absorption and the increase of the core radiation due to the increase in cooling rate and tungsten density.

In order to explain and understand the dynamics and causality chain of the collapse, it has been reproduced using integrating modelling. The framework is composed by interpretative METIS simulations and predictive RAPTOR simulations using QuaLiKiz neural network for heat transport. The LUKE code, in stand alone, is used to determine the LHCD power absorption profiles. The tungsten density and its profile are computed using bolometry inversion. The radiated power is computed using ADAS 50 for the tungsten cooling factor.
Even though previous integrated modelling of W/background plasma interplay on JET and AUG used more complete framework in terms of physical non-linear coupling with predictive heat, particle, radiation etc., at the beginning of this work, only RAPTOR was able to handle IMAS data and therefore it could be easily applied to WEST. Nowadays we can use the IMASified version of JETTO (called High Fidelity Pulse Simulator) to read and model WEST.

What has been found thanks to the integrated modelling is that three effects happening simultaneously are required to capture the velocity of $T_e(0)$ collapse: the W cooling factor increase, LHCD central absorption reduction and tungsten accumulation.
Regarding the first ingredient, as the cooling factor is directly linked to the electron temperature, an initial T_e reduction, triggered by a slightly rising density, leads to increased cooling factor inducing a further decrease in T_e, in a vicious cycle. Core LHCD power absorption is reduced as expected in a colder plasma because the peak of the deposition moves further off-axis with the decrease of central T_e. This leads to a negative power balance in the core that initiates the temperature collapse. At the same time, the ∇T_e flattening induces a ∇T_i flattening by equipartition, and, if tungsten transport is mainly neoclassical, an initial T_e flattening is needed to trigger W accumulation. Therefore, tungsten profile peaks. Then, when the vicious cycle is initiated, both phenomena happen simultaneously. In the end, a broadening of the current profile occurs (drop of l_i) and MHD activity is triggered.

Despite the fact that a large step forward is made in this thesis regarding our understanding of the dynamics of the collapse, still numerous significant improvements can be made in the future. Firstly, the high-fidelity pulse simulator can be used for the WEST model in order to simultaneously analyse the temporal evolution of the tungsten density in a self-consistent manner with respect to the evolution of the density and temperature of the background plasmas. Secondly, to improve WEST performances, a central electron heating is crucial to be as far as possible above the temperature range in which the tungsten cooling factor increases hence such that T_e is well above 3 keV and therefore becomes insensitive to mild density increments;

to beat the core tungsten radiation in the core and therefore to be resilient to higher levels of tungsten contamination.
In WEST coming campaigns, using dominant LHCD, the central electron temperature will be monitored by raising the ratio of injected power over density.
The core electron heating will be maximized, thanks to ICRH dedicated experiments adjusting the frequency and the H minority concentration. From 2023, central electron heating will be complemented by 3 gyrotrons providing 3MW of ECRH.

Bibliography

[1] *U.S. Energy Information ADMINISTRATION. ≪ International Energy Outlook ≫*. 2021. URL: www.eia.gov/ieo. (cit. on p. 25).

[2] A. Zerrahn et al. “On the economics of electrical storage for variable renewable energy sources”. In: *European Economic Review* 108 (2018), pp. 259–279 (cit. on p. 26).

[3] A. Evans et al. “Assessment of utility energy storage options for increased renewable energy penetration”. In: *Renewable and Sustainable Energy Reviews* 16 (2012). 4141- 4147 (cit. on p. 26).

[4] Daniel Clery. “A shortage of tritium fuel may leave fusion energy with an empty tank”. In: *Science* 376 (6600 2022) (cit. on p. 27).

[5] A. Zerrahn et al. “European Research Roadmap to the Realization of Fusion Energy”. In: (2018) (cit. on pp. 27, 30).

[6] Peter Donnel. “Impurity transport in tokamak plasmas: gyrokinetic study of neoclassical and turbulent transport”. PhD thesis. Dec. 2018 (cit. on p. 27).

[7] Robert Arnoux. “Which was the rst ’tokamak’ - or was it ’tokomag’?” In: *ITER* (2018) (cit. on p. 28).

[8] Vladimir Smirnov. “Tokamak foundation in USSR/Russia 1950-1990”. In: *Nuclear Fusion* 50.1 (2009), p. 014003 (cit. on p. 28).

[9] Joan Lisa Bromberg. *OFusion: Science, Politics, and the Invention of a New Energy Source*. MIT Press, 1982. ISBN: 978-0-262-02180-7 (cit. on p. 29).

[10] Robert Arnoux. “INTOR: The international fusion reactor that never was”. In: *ITER* (2008) (cit. on p. 29).

[11] C.M. Braams et al. *Nuclear Fusion: Half a Century of Magnetic Con nement Research*. Institute of Physics Publishing, 2002. ISBN: 978-0-7503-0705-5 (cit. on p. 29).

[12] Fusion Electricity EFDA. “A roadmap to the realization of fusion energy”. In: (2012) (cit. on p. 30).

[13] V.D. Shafranov. “Plasma equilibrium in a magnetic field”. In: *Plasma Physics* 2 (1966), p. 103 (cit. on p. 32).

[14] Alfvén. “Existence of electromagnetic-hydrodynamic waves”. In: *Natur* 150 (1942). 3805, pp. 405–406 (cit. on p. 32).

[15] J. Blum et al. “Reconstruction of the equilibrium of the plasma in a Tokamak and identi cation of the current density pro le in real time”. In: *Computational Physics* 231 (2012), pp. 960–980 (cit. on p. 32).

[16] J.P. Freidberg. *Plasma physics and fusion energy*. Cambridge University Press, 2007. ISBN: 0521851076 (cit. on p. 34).

[17] J. Wesson. *Tokamaks*. Oxford: Claredon press, 1997 (cit. on pp. 35, 36).

[18] P. Moreau et al. “The new magnetic diagnostics in the WEST tokamak”. In: *Review of Scienti c Instrument* 89 (2018). 10J109 (cit. on p. 35).

[19] B. Faugeras et al. “Equilibrium reconstruction at JET using Stokes model for polarimetry”. In: *Nucl. Fusion* 58 (2018). 106032, p. 19 (cit. on p. 36).

[20] S.M. Kaye et al. “ITER L mode confinement satabase”. In: *Nucl. Fusion* 37.9 (1997) (cit. on pp. 36, 37, 42, 57, 58, 73).

[21] *H-mode*. URL: http://fusionwiki.ciemat.es/wiki/H-mode (cit. on p. 37).

[22] E. Buckingham. “On Physically Similar Systems; Illustrations of the Use of Dimensional Equations”. In: *Phys. Rev.* 4 (). 345 (cit. on p. 39).

[23] B B Kadomtsev. “Tokamaks and dimensional analysis”. In: *Sov. J. Plasma Phys.* 4 (1975), pp. 531–535 (cit. on pp. 39, 42).

[24] J. W. Connor. “Invariance principles and plasma con nement”. In: *Plasma Phys. Control. Fusion* 30.6 (1988), pp. 619–650 (cit. on p. 39).

[25] A. A. Vlasov. “On Vibration Properties of Electron Gas”. In: *J. Exp. Theor. Phys. (in Russian)* 8.3 (1938), p. 291 (cit. on p. 40).

[26] T.C. Luce et al. “Application of dimensionless parameters scaling techniques to the design and interpretation of magnetic fusion experiments”. In: *Plasma Phys. Control. Fusion* 50 (2008). 043001, p. 87 (cit. on pp. 41, 66, 74).

[27] Y. Sarazin et al. “Impact of scaling laws on tokamak reactor dimensioning”. In: *Nucl. Fusion* 60 (2020). 016010, p. 13 (cit. on pp. 41, 59, 67).

[28] ITER Physics Basis Editors. “ITER Physics Basis Expert Groups on Confinement and Transport and Confinement Modelling and Database”. In: *Nucl. Fusion* 39 (1999) (cit. on pp. 42, 59).

[29] G. Verdoolaege et al. “The updated ITPA global H-mode confinement database: description and analysis”. In: *Nuclear Fusion* 61 (2021). 076006, p. 29 (cit. on p. 43).

[30] D.C. McDonald et al. “Recent progress on the development and analysis of the ITPA global H-mode con nement database”. In: *Nucl. Fusion* 47 (2007). 147 (cit. on pp. 43, 44, 82).

[31] A.C.C. Sips et al. “Assessment of the baseline scenario at $q_{95} = 3$ for ITER”. In: *Nucl. Fusion* 58 (2018). 126010, p. 23 (cit. on p. 44).

[32] R. Johansson. *Numerical Python*. Apress, 2018 (cit. on p. 46).

[33] *Scikit-learn 0.23.1*. URL: https://scikit-learn.org/stable/modules/linear%20model.html (cit. on pp. 47, 49, 91).

[34] *Wikipedia. Ordinaty least squares*. URL: https://en.wikipedia.org/w/index.php?title=Ordinary%20least%20%20squares&oldid=895165643 (cit. on p. 47).

[35] *Wikipedia. Weighted least squares*. URL: https://en.wikipedia.org/wiki/Weighted%20least%20squares (cit. on p. 47).

[36] *Wikipedia. Covariance matrix*. URL: https://en.wikipedia.org/wiki/Covariance%20matrix (cit. on p. 47).

[37] D.D. Mijnsbrugge. "Study of energy con nement scaling in tokamaks by means of advanced statistical methods". PhD thesis. PhD thesis, Ghent university, 2018-2019 (cit. on p. 48).

[38] *Wikipedia. Generalized linear model*. URL: https://en.wikipedia.org/wiki/Generalized%20linear%20model (cit. on p. 48).

[39] *Generalized linear model constrained*. URL: texttthttps://www.statsmodels.org/stable/generated/statsmodels.genmod.%20generalized%20linear%20model.GLM.%20t%20constrained.html (cit. on pp. 48, 140).

[40] F.L. Hinton and R.D. Hazeltine. "Theory of plasma transport in toroidal con nement systems". In: *Rev. Mod. Phys.* 48 (1976), pp. 239–308 (cit. on pp. 50, 122).

[41] Per Helander and Dieter J. Sigmar. *Collisional transport in magnetized plasmas*. Cambridge University Press, 2005 (cit. on pp. 50, 122).

[42] J.M. Rax. "Physique des Tokamaks." PhD thesis. Ecole polytechnique : Physique. Ed. de l'Ecole polytechnique, 2011. ISBN: 9782730215800 (cit. on p. 50).

[43] J. Weiland et al. "Diffusive particle and heat pinch effects in toroidal plasmas". In: *Nucl. Fusion* 29.10 (1989), p. 1810 (cit. on p. 50).

[44] T.J.M. Boyd and J.J. Sanderson. *The physics of plasmas*. Cambridge University Press, 2003. ISBN: 0521459125 (cit. on p. 51).

[45] C. Angioni et al. "Tungsten transport in JET H-mode plasmas in hybrid scenario, experimental observations and modelling". In: *Nucl. Fusion* 54 (2014). 083028, p. 26 (cit. on p. 51).

[46] E.A. Belli et J. Candy. "Drift-Kinetic Simulations of Neoclassical Transport". In: APS-DPP Meeting Dallas. 2008 (cit. on p. 51).

[47] E.A. Belli et J. Candy. "Full linearized Fokker-Planck collisions in neoclassical transport simulations". In: *Plasma Phys. Control. Fusion* 54 (2012). 15015 (cit. on p. 51).

[48] W. Horton. "Drift waves and transport". In: *Rev. Mod. Phys.* 71.3 (1999), p. 735 (cit. on p. 52).

[49] Bruce D. Scott. “Drift wave versus interchange turbulence in tokamak geometry: Linear versus nonlinear mode structure”. In: *Physics of Plasmas* 12.6 (2005). 062314 (cit. on p. 52).

[50] Bruce D Scott. “Tokamak edge turbulence: background theory and computation”. In: *Plasma Physics and Controlled Fusion* 49.7 (2007) (cit. on p. 52).

[51] V. Grandgirard et al. “A 5D gyrokinetic full-f global semi-lagrangian code for flux-driven ion turbulence simulations”. In: *Computer Physics Communications* 207 (2016) (cit. on p. 52).

[52] E.Lanti et al. “Orb5: A global electromagnetic gyrokinetic code using the PIC approach in toroidal geometry”. In: *Computer Physics Communications* 251 (2020). 107072 (cit. on p. 52).

[53] E. Jenko et al. “Electron temperature gradient driven turbulence”. In: *Physics of Plasmas* 7.5 (2000), pp. 1904–1910 (cit. on p. 52).

[54] J. Candy et Re Waltz. “An eulerian gyrokinetic-maxwell solver”. In: *Journal of Computational Physics* 196.2 (2003), pp. 545–581 (cit. on p. 52).

[55] A.G.Peeters et al. “The nonlinear gyro-kinetic flux tube code GKW”. In: *Computer Physics Communications* 180 (2009), pp. 2650–2672 (cit. on p. 52).

[56] K. L. van de Plassche et al. “Fast modeling of turbulent transport in fusion plasmas using neural networks”. In: *Physics of Plasmas* 27 (2020). 022310 (cit. on pp. 52, 115, 117).

[57] C. Bourdelle et al. “A new gyrokinetic quasilinear transport model applied to particle transport in tokamak plasmas”. In: *Physics of Plasmas* 14.11 (2007). 112501 (cit. on p. 52).

[58] C. Bourdelle et al. “Core turbulent transport in tokamak plasmas : bridging theory and experiment with QuaLiKiz”. In: *Plasma Physics and Controlled Fusion* 58.1 (2015). 014036 (cit. on p. 52).

[59] J. Citrin et al. “Tractable flux-driven temperature, density, and rotation profile evolution with the quasilinear gyrokinetic transport model QuaLiKiz”. In: *Plasma Physics and Controlled Fusion* (2017) (cit. on p. 52).

[60] J. E. Kinsey et al. “The first transport code simulations using the trapped gyro-Landau-fluid model”. In: *Physics of Plasmas* 15 (2008). 055908 (cit. on p. 52).

[61] M. Erba et al. “Development of a non-local model for tokamak heat transport in L-mode, H-mode and transient regimes”. In: *Plasma Physics and Controlled Fusion* 39.2 (1997), p. 261 (cit. on p. 52).

[62] E. Fable et al. “Progress in characterization and modelling of the current ramp-up phase of ASDEX Upgrade discharges”. In: *Nuclear Fusion* 52.6 (2012). 063017 (cit. on p. 53).

[63] J.F. Artaud et al. “The CRONOS suite of codes for integrated tokamak modelling”. In: *Nuclear Fusion* 50.4 (2010). 043001 (cit. on p. 53).

[64] M. Romanelli et al. “JINTRAC : A System of Codes for Integrated Simulation of Tokamak scenarios”. In: *Plasma and Fusion Research* 9 (2014). 3403023 (cit. on p. 53).

[65] F. Felici. “Real-Time Control of Tokamak Plasmas: from Control of Physics to Physics-Based Control”. PhD thesis. Ecole polytechnique federale de Lausanne, 2011 (cit. on pp. 53, 115, 116).

[66] *WEST users portal*. URL: https://westusers.partenaires.cea.fr/group/west%20/machine-description.html (cit. on p. 53).

[67] J.Bucalossi et al. “The WEST project: Testing ITER divertor high heat flux component technology in a steady state tokamak environment”. In: *Fusion Engineering and Design* 89 (2014), pp. 907–912 (cit. on p. 53).

[68] M. Firdaouss et al. “First feedback during series fabrication of ITER like divertor tungsten components for the WEST tokamak”. In: *Phys. Scr.* 96 (2021). 3403023 (cit. on p. 55).

[69] M. Firdaouss et al. “Overview of the different processes of tungsten coating implemented into WEST tokamak”. In: *Fusion Eng.Des.* 124 (2017) (cit. on p. 55).

[70] T. Batal et al. “Design and manufacturing of WEST Baffe”. In: *Fusion Engineering and Design* 98-99 (2015), pp. 1221–1225 (cit. on p. 55).

[71] M. Firdaouss et al. “Design and manufacturing of bulk tungsten tiles for WEST outer limiter”. In: *Fus. Eng. and Design* 160 (2020). 112000 (cit. on p. 55).

[72] J. Hillairet et al. “WEST actively cooled load resilient ion cyclotron resonance heating system results”. In: *Nucl. Fusion* 61 (2021). 096030 (cit. on p. 56).

[73] L. Delpech et al. “Evolution of the Tore Supra Lower Hybrid Current Drive System for WEST”. In: *Fusion Engineering and Design* 96-97 (2015), pp. 452–457 (cit. on p. 56).

[74] T. Putterich et al. “Calculation and experimental test of the cooling factor of tungsten”. In: *Nuclear Fusion* 50.2 (2010). 025012 (cit. on pp. 56, 87).

[75] C.D. Challis et al. “Effect of fuel isotope mass on q-profile formation in JET hybrid plasmas”. In: *Nucl. Fusion* 60 (2020). 086008 (cit. on p. 56).

[76] E. Joffrin et al. “First scenario development with the JET new ITER-like wall”. In: *Nuclear Fusion* 54 (2014). 013011, p. 12 (cit. on p. 56).

[77] P. Buratti et al. “MHD activity in FTU plasmas with reversed magnetic shear”. In: *Plasma Phys. Control. Fusion* 39 (1997). B383 (cit. on p. 56).

[78] P. Manas et al. “Tungsten transport in tokamaks: towards real-time kinetic-theory-based plasma performance optimisation”. In: *IAEA* (2021)) (cit. on p. 56).

[79] F. Imbeaux et al. “Design and rst applications of the ITER integrated modelling & analysis suite”. In: *Nuclear Fusion* 55.12 (2015). 123006 (cit. on p. 61).

[80] B. Faugeras. “An overview of the numerical methods for tokamak plasma equilibrium computation implemented in the NICE code”. In: *Fusion Engineering and Design* 160 (2020). 112020 (cit. on p. 61).

[81] Y-K.M. Peng and D.J. Strickler. “Features of spherical torus plasmas”. In: *Nucl. Fusion* 26 (1986). 769 (cit. on p. 63).

[82] C. Bourdelle et al. “Stabilizing impact of high gradient of β on microturbulence”. In: *Physics of Plasmas* 10 (2003). 2881 (cit. on p. 63).

[83] M. Maslov et al. “Energy and particle con nement in JET H-mode plasma”. In: *Nuclear Fusion* 60 (2020). 036007 (cit. on p. 73).

[84] J.E. Rice et al. “Understanding LOC/SOC phenomenology in tokamaks”. In: *Nuclear Fusion* 60 (2020). 105001 (cit. on p. 77).

[85] P.N. Yushmanov et al. “Scaling for tokamak energy confinement”. In: *Nucl. Fusion* 30 (1990). 10 (cit. on p. 79).

[86] O. Sauter et al. “Considerations on energy confinement time scaling using present tokamak databases and prediction for ITER size experiments”. In: *Nuclear Fusion* 40.5 () (cit. on p. 81).

[87] P. Devynck et al. “Calculation of the radiated power in WEST”. In: . *Phys. Commun.* 5 (2021). 095008 (cit. on p. 86).

[88] T. Putterich et al. “Determination of the tolerable impurity concentrations in a fusion reactor using a consistent set of cooling factors”. In: *Nucl. Fusion* 59 (2019). 056013 (cit. on pp. 86, 87).

[89] J. L. Ségui et al. “An upgraded 32-channel heterodyne electron cyclotron emission radiometer on Tore Supra”. In: *Review of Scienti c Instruments* 76 (2005). 123501 (cit. on p. 88).

[90] K. Wongrach et al. “WEST tokamak hard x-ray tomography inversion”. In: *AIP Advances* 11 (2021). 085313 (cit. on p. 88).

[91] C. Gil et al. “Renewal of the interfero-polarimeter diagnostic for WEST”. In: *Fusion Engineering and Design,* 140 (2019). 81-91 (cit. on p. 89).

[92] R. Dumont et al. “Combined kinetic and transport modeling of radiofrequency current drive”. In: *Physics of Plasmas* 7 (2000). 4972 (cit. on pp. 94, 103).

[93] V. D. Shafranov. “Plasma Physics Determination of the parameters β_I and li in a Tokamak for arbitrary shape of plasma pinch cross-section”. In: *Plasma Physics* 13 (1971). 757 (cit. on p. 103).

[94] C. Angioni et al. “A comparison of the impact of central ECRH and central ICRH on the tungsten behaviour in ASDEX Upgrade H-mode plasmas”. In: *Nucl. Fusion* 57 (2017). 056015 (cit. on p. 112).

[95] D. Gallart et al. “Modelling of JET hybrid plasmas with emphasis on performance of combined ICRF and NBI heating”. In: *Nucl. Fusion* 58 (2018). 106037 (cit. on p. 112).

[96] Vl.V. Bobkov et al. “Compatibility of ICRF antennas with W-coated limiters for di erent plasma geometries in ASDEX Upgrade”. In: *Journal of Nuclear Materials* 363-365 (2007). 122-126 (cit. on p. 112).

[97] J.F. Artaud et al. “Metis: a fast integrated tokamak modelling tool for scenario design”. In: *Nucl. Fusion* 58 (2018). 105001 (cit. on pp. 115, 116).

[98] Y. Peysson et al. “Numerical simulations of the radio-frequency-driven toroidal current in tokamaks”. In: *Fusion Science and Technology* 65.1 (2014). 095008 (cit. on p. 115).

[99] C. Bourdelle et al. “A new gyrokinetic quasilinear transport model applied to particle transport in tokamak plasmas”. In: *Phys. Plasmas* 14 (2007). 11250 (cit. on p. 117).

[100] C. Bourdelle et al. “Core turbulent transport in tokamak plasmas: bridging theory and experiment with QuaLiKiz”. In: *Plasma Phys. Control. Fusion* 58 (2016). 014036 (cit. on p. 117).

[101] 2021 C. D. Stephens. “Advances in Quasilinear Gyrokinetic Modeling of Turbulent Transport”. PhD thesis. University of California, Los Angeles, 2021 (cit. on pp. 117, 118).

[102] Romanelli et al. “Numerical study of linear dissipative drift electrostatic modes in tokamaks”. In: *Phys. Plasmas* 14 (2007)). 082305 (cit. on p. 117).

[103] A. Ho. “Development of neural networks towards predict-first plasma modelling”. PhD thesis. PhD thesis. Eindhoven University of Technology, 2021 (cit. on p. 118).

[104] Y. Peysson et al. “versatile ray-tracing code for studying rf wave propagation in toroidal magnetized plasmas”. In: *Plasma Physics and Controlled Fusion* 54 (2012)). 045003 (cit. on p. 118).

[105] Y. Peysson et al. “Fast electron bremsstrahlung in axisymmetric magnetic con guration”. In: *Physics of Plasmas* 15 (2008). 092509 (cit. on p. 118).